Dissertation

submitted to the

Combined Faculties for the Natural Sciences and for Mathematics

of the Ruperto-Carola University of Heidelberg, Germany

for the degree of

Doctor of Natural Sciences

put forward by

Jan-Eric Meißner M.Sc.

born in Berlin

oral examination: 19.04.2017

Quantitative pulsed CEST MR imaging

Referees: Prof. Dr. Peter Bachert

Prof. Dr. Rainer Fink

Quantitative pulsed CEST MR imaging

Chemical Exchange Saturation Transfer (CEST) experiments enable the indirect detection of small metabolites, e.g. creatine, and proteins in living tissue by means of magnetic resonance imaging. Selective RF saturation of solute protons in chemical exchange with water leads to an accumulation of saturation in the water magnetization. The resulting reduction of the water signal depends on physiological properties, e.g. pH, temperature and solute concentration, but also on the saturation scheme. In a clinical setup, the latter is limited to a series of short RF-pulses to obey safety regulations. Pulsed saturation is difficult to describe theoretically, thus, the quantitative determination of physiological parameters via CEST experiments is a challenging task.

In this thesis, a new analytical model for CEST is proposed, which extends a former interleaved saturation-relaxation approach. This model enables the analytical calculation of Z-spectra yielding deeper insight into the physics of pulsed CEST experiments. Furthermore, it enables for the first time in the case of pulsed saturation the separate and independent determination of the exchange rate k and the relative proton concentration f. The validity of this approach was tested by simulations and verified in measurements of model solutions containing creatine on a 7-Tesla whole-body MR tomograph. Finally, the obtained knowledge was used to quantitatively investigate pH and absolute creatine concentration in the human calf muscle under resting conditions and during exercise.

Quantitative gepulste CEST-MR-Bildgebung

Chemical Exchange Saturation Transfer (CEST) Experimente ermöglichen die indirekte Detektion von kleinen Metaboliten, z.B. Kreatin, und Proteinen im lebenden Gewebe mittels Magnetresonanz-Bildgebung. Selektive RF-Sättigung von gebundenen Protonen, welche im chemischem Austausch mit Wasser stehen, führt zu einer Akkumulation von Sättigung in der Magnetisierung des Wassers. Die resultierende Reduktion des Wasser-Signals hängt von physiologischen Eigenschaften, wie pH, Temperatur und Metabolit-Konzentration, aber auch von dem verwendeten Sättigungsschema ab. Letzteres ist an klinisch einsetzbaren MR-Tomographen auf eine Serie kurzer RF-Pulse beschränkt, um sicherheitstechnische Vorschriften einzuhalten. Die gepulste Sättigung ist allerdings theoretisch nur schwer zu beschreiben, so dass die quantitative Bestimmung physiologischer Größen mittels CEST-Experimenten eine Herausforderung darstellt.

In dieser Arbeit wird ein neues analytisches Modell für CEST auf Grundlage eines bereits bekannten verschachtelten Sättigungs- und Relaxations-Ansatzes vorgestellt. Dieses Modell erlaubt es, das Z-Spektrum analytisch zu berechnen und ermöglicht dadurch tiefere Einblicke in die Physik von gepulsten CEST-Experimenten. Des Weiteren konnten erstmals für den Fall der gepulsten Sättigung die Austauschrate k und die relative Protonenkonzentration f getrennt und unabhängig voneinander bestimmt werden. Die Gültigkeit dieses Ansatzes wurde durch Simulationen überprüft und mittels Messungen an Kreatin-Modellösungen an einem 7-Tesla-Ganzkörper-MR-Tomographen verifiziert. Schließlich konnte das gewonnene Wissen verwendet werden, um den pH-Wert und die absolute Konzentrationen von Kreatin im Wadenmuskel des Menschen in Ruhe und unter Belastung zu bestimmen.

Contents

List of abbreviations

AREX	apparent exchange-dependent relaxation
BM	Bloch-McConnell
bw	bandwidth
CE	chemical exchange
CEST	Chemical Exchange Saturation Transfer
CK	creatine-kinase
Cr	creatine
cw	continuous-wave
DC	duty cycle
DKFZ	German Cancer Research Center
dnsAREX	downfield-rNOE-suppressed apparent exchange-dependent relaxation
FID	free induction decay
FoV	field-of-view
FWHM	full-width-at-half-maximum
GRE	gradient-echo
LS	large-shift limit
MR	magnetic resonance
MRI	magnetic resonance imaging
NMR	nuclear magnetic resonance
NOE	Nuclear-Overhauser effect
RF	radio frequency
rNOE	exchange-relayed NOE
ROI	region-of-interest
SAR	specific absorption rate
ss	steady state
ssMT	semi-solid magnetization transfer
TE	echo time
TI	inversion time
TR	repetition time
WASABI	water shift and B1
WEX	water exchange
Z	value of the Z-spectrum

1. Introduction

The development of *nuclear magnetic resonance* (NMR) has its foundation in the discovery of the proton spin in the *Stern-Gerlach* experiment in 1922 [1]. This method was improved by *Otto Stern* and *Otto Frisch* enabling the detection of the electron spin in 1933 [2]. After *Isidor Rabi* showed that it is possible to induce transitions between discrete energy levels by oscillating magnetic fields [3], *Felix Bloch* [4] and *Edward M. Purcell* [5] used this knowledge independently to demonstrate nuclear magnetic resonance in condensed matter. The discovery of the chemical environment dependent resonance frequency (*chemical shift* [6]) gave rise to the important field of NMR spectroscopy, which is nowadays an important tool in physics and biochemistry to analyze the structure and characteristics of molecules. The transition to one of the most important tools in diagnostic medicine did not start until *Lauterbur* and *Mansfield* used magnetic field gradients to encode the spatial distribution of nuclear spins within the MR signal [7,8]. Magnetic resonance imaging (MRI) uses the relatively large NMR signal of free water protons and thus yields an excellent soft tissue contrast without the use of ionizing radiation or radioactive nuclides. In addition to the conventional relaxation-weighted NMR imaging of hydrogen protons, many other methods have been developed. These include the acquisition of rare (e.g. ^{23}Na or ^{17}O) and hyper-polarized nuclei (e.g. ^{3}He or ^{123}Xe) and diffusion-, perfusion- or contrast media-weighted imaging. All these contrasts have a physiological background and are therefore particularly interesting for the differentiation of pathological and healthy tissue. An additional intriguing contrast in this context is based on magnetization transfer experiments [9], due to the dependence on tissue pH and metabolite concentration.

The *Chemical Exchange Saturation Transfer* (CEST) [10,11] represents a special case of magnetization transfer experiments and combines the spectral selectivity of NMR spectroscopy and high spatial resolution of MR imaging. The contrast is based on the chemical exchange of water protons and other labile bound proton in small molecules or proteins. The spin states of this solute protons are saturated during selective radio frequency (RF) irradiation and hence the magnetization is destroyed. The chemical exchange accumulates this saturation in the water magnetization and leads to a signal enhancement, which is in the order of the exchange rate. Subsequent measurement of the modified MR signal of water enables thereby the indirect detection of low concentrated solutes with an improved signal-to-noise ratio compared to conventional NMR spectroscopy. Repetition of this experiment for different frequency offsets and plotting of the normalized water signal allows to acquire a saturation spectrum, the so-called Z-spectrum.

Several different CEST effects can be observed in Z-spectra obtained by in vivo measurements. These include the chemical exchange of protons bound in endogenous macromolecules such as proteins [12] and in metabolites of small molecular mass such as creatine [13–15], glucose [16,17], glutamate [18,19], glycosaminoglycans (GAG) [20] or lactate [21] as well as administered paramagnetic CEST (PARACEST) [22] and diamagnetic CEST agents [23]. In addition to the dependence with concentration, the CEST effect of amide and amine protons also correlates with pH. This was first reported in vitro [24] and later on also in vivo [12,25–27]. The actual CEST contrast, however, depends next to physiological factors also on technical parameters. Overall, the complex interplay of (i) exchange rate and relative concentration of

the low concentrated proton species, (ii) water relaxation properties of the specific tissue and (iii) used hardware and evaluation techniques makes the comparison of results obtained by different research groups complicated [28]. Hence, a quantitative data evaluation approach to acquire the chemical exchange-dependent variables in vivo, which in turn would allow the determination of pH and absolute concentration maps, is of high interest.
The two parameter, the exchange rate k_{BA} and relative concentration f_B, appear as a product in the equation of the ideal CEST effect [29–31]. A separation is possible exploiting the dispersion of the CEST effect with the RF saturation amplitude B_1. Several approaches were reported e.g. QUESP [30], multiple B_1 fit [31–33]) as well as *Dixon et al.* [34] could even show mathematically that the dispersion correlates linearly with $1/B_1^2$. This simple quantification by linear regression is called Ω-plot method. However, the validity is only given for PARACEST agents as for small chemical shifts the direct water saturation with the concomitant spillover effect prohibits the application [31, 32]. Standard evaluation methods, e.g. asymmetry analysis [12], are affected by the water relaxation parameters. Recently, a method to handle the spillover effect was proposed. This so-called inverse metric [27] can mathematically be merged with the Ω-plot formalism and thereby enables the investigation of endogenous agents with small chemical shifts [35]. However, the underlying theory is only valid in the case of experiments and investigations using continuous-wave (cw) saturation. In a clinical setup only saturation by trains of short pulses are allowed to maintain within specific absorption rate (SAR) and solid-state amplifier limits [36, 37] prohibiting the application of the Ω-plot method.

The goal of this study was to extend the spillover-corrected Ω-plot method for the case of saturation using trains of Gaussian-shaped RF pulses. The calculations were performed analytically and are based on the Bloch-McConnell (BM) equations. This yields a method that is applicable to data acquired on whole-body scanners within the SAR limits and, moreover, is able to separately quantitatively determine relative concentrations and exchange rates.
In contrast to other approaches integrating the B_1 field strength of time-dependent pulses (cw power equivalent [37]), the presented approach is based on the $R_{1\rho}$ model for CEST [38] and the integration of the longitudinal relaxation rate in the rotating frame $R_{1\rho}(B_1(t))$ as a function of the pulse shape. This approach allows the calculation of form factors for the modified CEST signal as well as the modified B_1 dispersion of the CEST effects generated by a series of Gaussian-shaped saturation pulses. These form factors translate directly to the Ω-plot equations for prediction of exchange rate k_{BA} and relative proton concentration f_B.
The transition to in vivo applications could be made through a suitable fitting routine. A high resolution imaging of reasonable pH values in vivo could be achieved by using the creatine signal in the human calf muscle. However, a difference in the obtained creatine concentration indicated other contributions to the signal.

Alltogether, the proposed method enables for the first time a full quantitative, and thereby comparable, signal in the clinical setup.

2. Physical and Biochemical Background

In this chapter the basic principles of nuclear magnetic resonance (NMR) are presented. Further, magnetic resonance imaging (MRI) is introduced. As this only captures a briev overview of the relevant topics, the reader is referred to the textbooks by *Abragam* [39], *Haacke et al.* [40] or *de Graaf* [41] for a more detailed theoretical description. Afterwards a short introduction to the important biochemical and physiological properties of the cell energy metabolism is given.

2.1. Nuclear spins and the Zeeman-effect

Every atomic nuclei consists of protons and neutrons. Both are fermions and have a half-numbered spin. Nuclei with an odd number of protons and/or neutrons carry a nuclear spin $\overrightarrow{I}$ different from zero. Accordingly, the nucleus of hydrogen, ^{1}H, consisting of a single proton, exhibits a nuclear spin of one-half. As a quantum-mechanical property the commutator relations for angular momentum apply for the nuclear spin $\overrightarrow{I}$:

$$\left[\hat{I}_i, \hat{I}_j\right] = i\hbar\epsilon_{ijk}\hat{I}_k \tag{2.1}$$

$$\left[\hat{I}^2, \hat{\overrightarrow{I}}\right] = 0 \tag{2.2}$$

Based on this, the eigenstates $|I, m\rangle$ of the nuclear spin own the following eigenvalues:

$$\hat{I}^2 |I, m\rangle = \hbar^2 I (I+1) |I, m\rangle \tag{2.3}$$

$$\hat{I}_z |I, m\rangle = \hbar m |I, m\rangle \tag{2.4}$$

where I is the angular momentum quantum number and $m = (-I, -I+1, \dots, I-1, I)$ is the magnetic quantum number. It holds that $\Delta m = 1$. Associated to the nuclear spin is a magnetic moment

$$\hat{\overrightarrow{\mu}} = \gamma \hat{\overrightarrow{I}} \tag{2.5}$$

with the gyromagnetic ratio γ, which is specific to each nucleus. For hydrogen protons ^{1}H it was experimentally shown that $\gamma = \frac{g_p \mu_N}{\hbar} = 2.675 \cdot 10^8 \, \frac{\mathrm{Hz}}{\mathrm{T}}$ and accordingly $\frac{\gamma}{2\pi} = 42.577 \, \frac{\mathrm{MHz}}{\mathrm{T}}$. The interaction of the magnetic moment $\overrightarrow{\mu}$ and a static external magnetic field along the z-axis $\overrightarrow{B} = (0,\ 0,\ B_0)$ is characterized by the Hamiltonian $\hat{\mathcal{H}}$:

$$\hat{\mathcal{H}}_z = -\hat{\overrightarrow{\mu}} \cdot \overrightarrow{B} = -\hat{\mu}_z \cdot B_0 = -\gamma \hat{I}_z \cdot B_0 \tag{2.6}$$

The angular momentum and the Hamiltonian are linear, i.e. $[\hat{I}_i, \hat{\mathcal{H}}] = 0$ and $[\hat{I}^i, \hat{\mathcal{H}}] = 0$. Thus, both have the same eigenstates $|I, m\rangle$ and the time-independent Schrödinger equation for the static magnetic field reads:

$$\hat{\mathcal{H}}_z |I, m\rangle = E_m |I, m\rangle = -\gamma\hbar m B_0 |I, m\rangle \tag{2.7}$$

Consequently this leads to a discrete splitting into $2I+1$ equidistant energy levels, named Zeeman effect [42]. The energy difference of two possible eigenstates of a proton $|\alpha\rangle = |1/2, -1/2\rangle$ and $|\beta\rangle = |1/2, +1/2\rangle$ is given by (figure 2.1)

$$\Delta E = E_\alpha - E_\beta = \gamma\hbar B_0 = \hbar\omega_0 \tag{2.8}$$

with the so called *Larmor frequency* ω_0. The energy required for a transition between the two adjacent levels can be induced using time-varying magnetic fields.

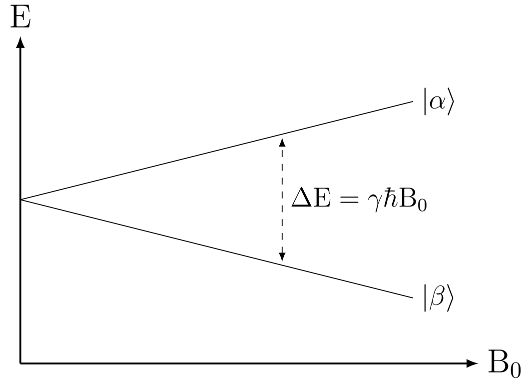

Figure 2.1.: The Zeeman splitting is shown for a nucleus with the spin quantum number $I = 1/2$ as a function of the magnetic field B_0. The energy difference between the two states α and β is given by $\Delta E = \gamma\hbar B_0$.

2.2. Macroscopic magnetization

The preceeding theoretical description is limited to characterize the behavior of a single nuclear spin. However, in almost every NMR experiment a macroscopic ensemble containing a large number of nuclei N (with $N > 10^{16}$) has to be considered. As shown in section 2.1 the energy levels are split due to the Zeemann effect into $2I+1$ states and their population probability p_m in a thermal equilibrium is governed by the *Boltzmann statistic*:

$$p_m = \frac{1}{Z} e^{-E_m/k_B T} \tag{2.9}$$

where $Z = \sum_{m=-I}^{I} e^{-\frac{E_m}{k_B T}}$ is the canonical number of states, k_B the Boltzmann constant and T the equilibrium temperature. For the sake of simplicity from now on only an ensemble of N hydrogen atoms, which exhibit a nuclear spin of 1/2 and therefore the two energy states $|\alpha\rangle$ and $|\beta\rangle$, is considered. The expected value of the z-component of the magnetic moment is then given by

$$\begin{aligned} \langle\hat{\mu}_z\rangle &= \gamma\,\langle I_z\rangle = \gamma\left(p_{-1/2}\langle\alpha|\hat{I}_z|\alpha\rangle + p_{+1/2}\langle\beta|\hat{I}_z|\beta\rangle\right) \\ &= \frac{1}{2}\gamma\hbar\left(p_{+1/2} - p_{-1/2}\right) = \frac{1}{2}\gamma\hbar P \end{aligned} \tag{2.10}$$

where the polarization P, which is given by the difference in probabilities between the two states, is also defined as the normalized difference in population:

$$P = p_{+1/2} - p_{-1/2} = \frac{\Delta N}{N}. \tag{2.11}$$

Using the energy eigenvalues E_m (equation 2.7) and the definition of the population probability (equation 2.9) yields

$$P = \frac{e^{\frac{\gamma\hbar B_0}{2k_BT}} - e^{-\frac{\gamma\hbar B_0}{2k_BT}}}{e^{\frac{\gamma\hbar B_0}{2kT}} + e^{-\frac{\gamma\hbar B_0}{2kT}}} = \tanh\left(\frac{\gamma\hbar B_0}{2k_BT}\right). \tag{2.12}$$

At room temperature and for the field strengths used in this work it can be assumed that $\gamma\hbar B_0 \ll k_BT$. This allows to use the Taylor expansion at $x = 0$ for the hyperbolic tangens, yielding in first order approximation for the polarization

$$P \approx \frac{\gamma\hbar B_0}{2k_BT}. \tag{2.13}$$

For hydrogen protons in an external field $B_0 = 7\,\mathrm{T}$ at room temperature ($T = 298.15\,\mathrm{K}$) the polarization is $P \approx 10^{-6}$. The macroscopic magnetization of a spin ensemble, which is the sum of all magnetic moments in volume V times the average magnetic moment, is proportional to the polarization as follows

$$\vec{M} = \frac{N}{V}\left\langle\hat{\vec{\mu}}\right\rangle = \frac{1}{2}\gamma\hbar\frac{N}{V}\vec{P} \approx \frac{1}{4}\frac{N}{V}\frac{\gamma^2\hbar^2}{k_BT}\vec{B} \tag{2.14}$$

The temperature dependence obeys the *Curie law* ($M \propto T^{-1}$). Only due to the large number of protons ($\approx 6.6 \cdot 10^{19}$ mm^{-3}) a measurable magnetization is produced for the thermal polarization. The magnetization is linear with the magnetic field strength B_0 and depends quadratically on the nucleus specific gyromagnetic ratio γ.

2.2.1. Time evolution of the magnetization

For a proton spin in a time-dependent magnetic field the time-dependent Schrödinger equation has to be employed

$$i\hbar\frac{\partial}{\partial t}\left|I, m\right\rangle = \hat{\mathcal{H}}(t)\left|I, m\right\rangle \tag{2.15}$$

where $\hat{\mathcal{H}}(t) = -\hat{\vec{\mu}}\cdot\vec{B}(t)$ is the time-dependent Hamiltonian. The *Ehrenfest theorem* [43] allows to determine the expectation value of the time-dependent magnetic moment

$$\frac{\mathrm{d}}{\mathrm{d}t}\left\langle\hat{\vec{\mu}}\right\rangle = \frac{i}{\hbar}\left\langle\left[\hat{\mathcal{H}}, \hat{\vec{\mu}}\right]\right\rangle + \left\langle\frac{\partial\hat{\vec{\mu}}}{\partial t}\right\rangle \tag{2.16}$$

Using the commutator relations given in equations (2.1) yields

$$\frac{\mathrm{d}}{\mathrm{d}t}\left\langle\hat{\vec{\mu}}\right\rangle = \left\langle\hat{\vec{\mu}}\right\rangle \times \gamma\vec{B}(t) \tag{2.17}$$

The correspondence principle by *Niels Bohr* states that systems described by quantum mechanics satisfy classical physics in the macroscopic limit [44]. Due to the large number of proton spins in the measurement volume it is sufficient to investigate the time-dependent expectation value of the classical macroscopic magnetization:

$$\frac{\mathrm{d}}{\mathrm{d}t}\vec{M}(t) = \vec{M}(t) \times \gamma \vec{B}(t) \tag{2.18}$$

To produce a measurable signal an additional time-dependent radio frequency (RF) field $\vec{B}_1$ oscillating in the x-y-plane with frequency ω_{RF} is superimposed to the static magnetic field $\vec{B}_0$:

$$\vec{B}_1(t) = B_1 \begin{pmatrix} \cos(\omega_{RF} t) \\ \sin(\omega_{RF} t) \\ 0 \end{pmatrix} \tag{2.19}$$

In this case, the macroscopic magnetization $\vec{M}$ performs a movement around the superposition of both magnetic fields $\vec{B}(t) = \vec{B}_0 + \vec{B}_1(t)$. The equation of motion can be made more vivid by a transformation into a coordinate system rotating with $\vec{B}_1(t)$. This coordinate system is called rotating frame with its coordinates (x', y', z'). As a consequence $\vec{B}_1$ is aligned in the x'-direction and both fields are static, yielding:

$$\frac{\mathrm{d}}{\mathrm{d}t}\vec{M}'(t) = \vec{M}'(t) \times \gamma \vec{B}_{eff} \tag{2.20}$$

with the effective magnetic field $\vec{B}_{eff}$:

$$\vec{B}_{eff} = \begin{pmatrix} B_1 \\ 0 \\ B_0 - \frac{\omega_{RF}}{\gamma} \end{pmatrix} \tag{2.21}$$

If the resonance condition $\omega_{RG} = \omega_0 = \gamma B_0$ is satisfied, the z-component of the effective magnetic field $\vec{B}_{eff}$ vanishes. Thus the magnetic field only acts on the magnetization in x'-direction and the magnetization vector precesses in the y'-z'-plane with the frequency

$$\omega_1 = \gamma B_1. \tag{2.22}$$

In the laboratory system, this irradiation ensures a spiral flip of the magnetization $\vec{M}$. The flip angle α of the magnetization to the z-axis depends on the duration of the irradiation t_p and the magnetic field B_1:

$$\alpha = \int_0^{t_p} \omega_1(t)\mathrm{d}t = \int_0^{t_p} \gamma B_1(t)\mathrm{d}t \tag{2.23}$$

Upon completion of the RF irradiation, the magnetization precesses in the x-y-plane around the static magnetic field $\vec{B}_0$ with the Larmor frequency ω_0. This induces an alternating voltage in a receive coil, which forms the measurable MR signal. During and after the irradiation the magnetization starts to return back to the thermal equilibrium. These underlying relaxation processes are described in the following section.

2.2.2. Relaxation processes - Bloch equations

So far interactions of the nuclear spins with one another and with the environment have not been considered. If these inter- and intra-molecular interactions are taken into account, a precession – and thus relaxation – back to thermal equilibrium starts concurrent with the RF-irradiation. Phenomenologically *Felix Bloch* [4] expanded the equations given in (2.20) by these relaxation processes to the so called *Bloch equations*:

$$\frac{\mathrm{d}M_{x'}}{\mathrm{d}t} = \gamma \left(\vec{M} \times \vec{B}\right)_{x'} - \frac{M_{x'}}{T_2} \tag{2.24}$$

$$\frac{\mathrm{d}M_{y'}}{\mathrm{d}t} = \gamma \left(\vec{M} \times \vec{B}\right)_{y'} - \frac{M_{y'}}{T_2} \tag{2.25}$$

$$\frac{\mathrm{d}M_{z'}}{\mathrm{d}t} = \gamma \left(\vec{M} \times \vec{B}\right)_{z'} - \frac{M_{z'} - M_0}{T_1} \tag{2.26}$$

with the spin-spin relaxation time T_2, the spin-lattice relaxation time T_1 and the equilibrium magnetization M_0. The relaxation times are tissue specific and table 2.1 gives an overview of the relevant tissues in this work. The transversal T_2 relaxation is based on a dephasing of the individual spin packages among each other. In this case, no energy is transferred to the environment, yet exchanged between the individual spins. The longitudinal T_1 relaxation results from a coupling between the spin system and the thermal reservoir, the so-called lattice, and is induced by movements of molecules, which result in temporarily varying magnetic fields.

tissue type	T$_1$ [ms]			T$_2$ [ms]		
	1.5 T	3 T	7 T	1.5 T	3 T	7 T
white brain matter	656 ± 16^1	1084 ± 45^2	1220 ± 36^1	72 ± 4^2	69 ± 3^2	–
grey brain matter	1188 ± 69^1	1820 ± 114^2	2132 ± 103^1	95 ± 8^2	99 ± 7^2	–
cerebrospinal fluid	4070 ± 65^1	–	4425 ± 137^1	–	–	–
blood	1540 ± 23^1	1932 ± 85^2	2587 ± 283^1	290 ± 30^2	275 ± 50	–
skeletal muscle	1008 ± 20^2	1412 ± 13^2	1898 ± 144^3	44 ± 6^2	50 ± 4^2	–

Table 2.1.: In vivo T_1 and T_2 relaxation times of human tissue at different static magnetic field strengths B_0. Values are from (1): *Rooney et al.* [45]; (2): *Stanisz et al.* [46] and (3): *Rerich et al.* [15].

2.2.3. NMR signal

The Bloch equations (2.24)-(2.26) can be reshaped to reflect the transversal and longitudinal component of the magnetization. Assuming that the pulse duration t_p is much shorter than the relaxation time and using $M_\perp(t) = M_x(t) + iM_y(t)$ yields

$$\frac{\mathrm{d}M_\perp(t)}{\mathrm{d}t} = M_\perp(0)e^{i\omega t}e^{-t/T_2} \tag{2.27}$$

$$\frac{\mathrm{d}M_{z'}(t)}{\mathrm{d}t} = M_0 - \left(M_0 - M_z(0)\right)e^{-t/T_1} \tag{2.28}$$

with $M_\perp(0)$ and $M_z(0)$ as the magnetizations directly before T_2 or T_1 relaxation. In real NMR experiments an additional dephasing on the basis of magnetic field inhomogeneities occurs next to the interactions between the spins. This results in an effective decay of the magnetization with T_2^* (with $T_2^* \leq T_2$).

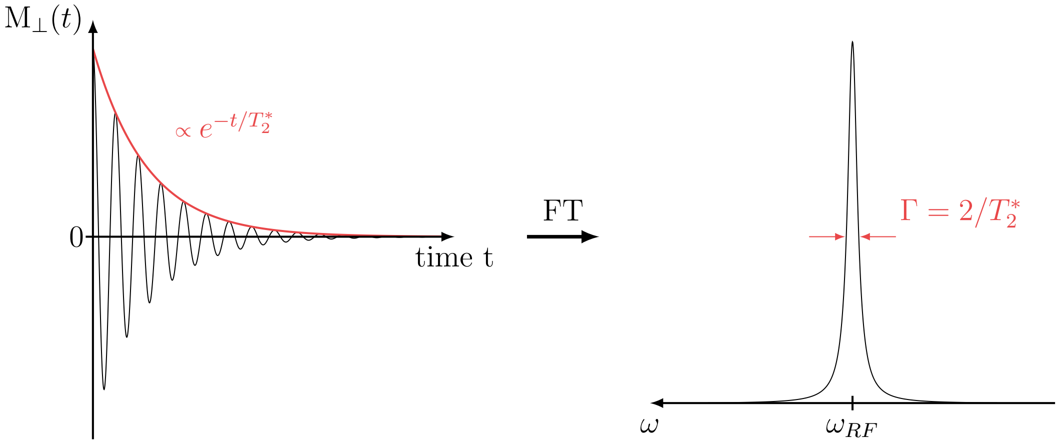

Figure 2.2.: The free induction decay (FID) during T_2^* relaxation in the time domain (left) yields a Lorentzian lineshape at the resonance frequency ω_{RF} after Fourier transformation (FT) in the frequency domain (right).

The rotating magnetization $M_\perp$ in the transversal x'-y'-plane creates a time-dependent magnetic flux. The resulting electromotive force can be measured in a receive coil as a voltage U_{ind}. Hence, the NMR signal in a volume V is given by

$$S(t) = U_{ind}(t) \propto \int \rho(\vec{r}) e^{i\omega_0 t} \mathrm{d}\vec{r} \tag{2.29}$$

with the spatial distribution $\rho(\vec{r})$ of the nuclear spins. The decrease in the transversal component towards thermal equilibrium can be measured as a exponential decay of the signal:

$$S(t) = A_0 e^{i\omega_0 t} e^{-t/T_2^*}. \tag{2.30}$$

This is referred to as free induction decay (FID) (figure 2.2 left). The Fourier transformation (FT) of the exponential decay leads to a Lorentzian lineshape in the frequency domain. The resonance frequency is ω_{RF} and the full-width-at-half-maximum Γ (FWHM) is given by $2/T_2^*$ (figure 2.2 right).

2.3. Chemical shift

The static magnetic field B_0 and the resonance frequency ω have so far been assumed to be constant for all nuclei. This assumption no longer applies to protons bound in molecules. Depending on the chemical environment, the electron cloud deforms and generates a local magnetic field $\vec{B}_{loc}$ for the proton spins:

$$\vec{B}_{loc} = \vec{B}_0 + \delta\vec{B} = \vec{B}_0(1-\sigma) \tag{2.31}$$

where σ is a dimensionless shielding constant. Consequently, the resonance frequency is changed to:

$$\omega_{loc} = \gamma B_0(1-\sigma). \tag{2.32}$$

Since this frequency shift depends strongly on the chemical environment, it is referred to as a *chemical shift*. The chemical shift is usually given as a field-independent frequency ratio in

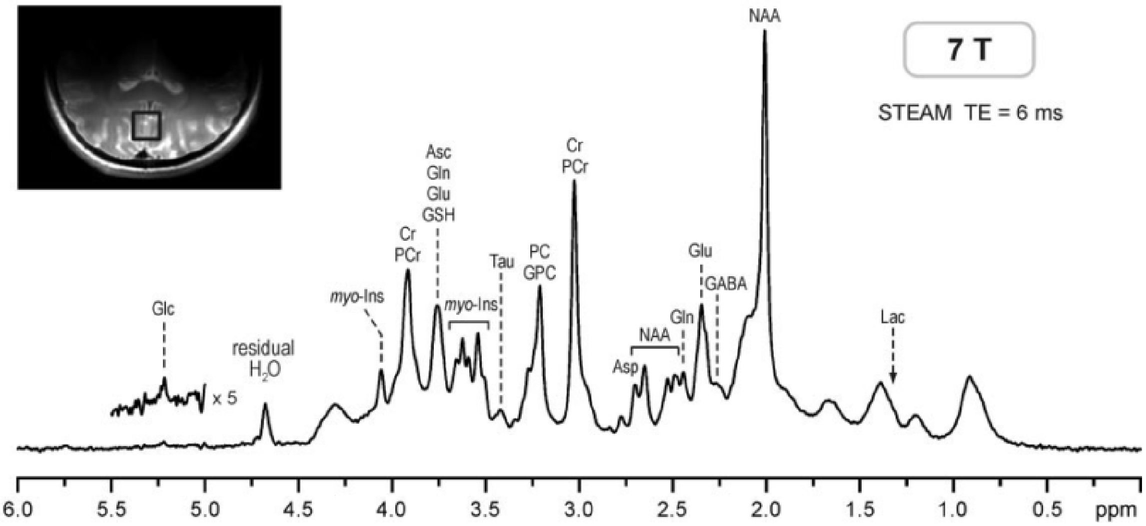

Figure 2.3.: ^{1}H NMR spectra acquired at 7T from the brain of a healthy subject. STEAM, $TE = 6\,\mathrm{ms}$, $TR = 5\,\mathrm{s}$, $VOI = 8\,\mathrm{cm}^3$, $NT = 160$. Processing: frequency and phase correction of single-scan FID arrays, FID summation, correction for the residual eddy currents, Gaussian multiplication ($\sigma = 0.15\,\mathrm{s}$), FT, zero-order phase correction. $SNR = 303$. Insets: transverse RARE images of the brain with the position of the VOI on the midline in the occipital lobe. Reproduced with kind permission from *Tkáč* et al., MRM 2009; 62(4):868-879. [47]

parts per million (ppm) to a reference frequency ω_{ref}.

$$\delta_i\,[\mathrm{ppm}] = \frac{\omega_i - \omega_{ref}}{\omega_{ref}} \cdot 10^6 \tag{2.33}$$

The reference frequency (i.e. $\delta = 0\,\mathrm{ppm}$) is the Larmor frequency of an arbitrary reference substance. Tetramethylsilane (TMS) is commonly used in MR spectroscopy as the reference substance [41]. For the magnetization transfer presented in chapter 3, the signal of protons in free water is assigned to the chemical shift of $\delta = 0\,\mathrm{ppm}$. The resonance frequency of protons in free water in vivo is shifted compared to TMS by $\Delta\delta \approx 4.7\,\mathrm{ppm}$. Conventionally the direction of the frequency axis of the chemical shift is reversed, meaning from downfield (higher frequencies) to upfield (lower frequencies).

The possibility to distinguish between different molecules or chemical groups via the chemical shift is the fundamental phenomenon, which allows to detect different substances by magnetic nuclear resonance [6]. A in vivo ^{1}H NMR spectrum of the human brain is shown in figure 2.3. The intensity ratios at specific resonances contain biochemical and metabolic information about the tissue. The most prominent resonances in vivo in the human brain belong to *n-acetyl-aspartat* (NAA), *phosphorcreatine* (PCr) and *creatin* (Cr). The importance in the energy metabolism of some of the metabolites is explained in section 2.5.1.

2.4. NMR imaging

So far only homogenous samples could be investigated. Using a gradient field $\vec{G}$ leads to a spatially dependent magnetic field $\vec{B}$:

$$\vec{B}(\vec{r}) = B_0 + \left(\vec{G} \cdot \vec{r}\right). \tag{2.34}$$

According to equation (2.8) the position of the spins is now encoded by their resonance frequency $\omega\left(\vec{B}(\vec{r})\right)$. The gradient field $\vec{G}$ is chosen to be parallel to the static magnetic field $\left(\vec{G} \parallel \vec{B}_0\right)$ to maintain the original quantization axis of the nuclear spins.

2.4.1. k-space

As a result from equations (2.29) and (2.34) the MR signal can be described by the following equation:

$$S(t) \propto \int \rho(\vec{r}) e^{i\omega_0 t} e^{i\gamma \vec{G}(t)\vec{r}t} \, \mathrm{d}\vec{r}. \tag{2.35}$$

Coordinate transformation into the rotating frame yields a signal equation which only depends on the spatial distribution of the nuclear spins $\rho(\vec{r})$ and the time dependent gradient field $\vec{G}(t)$

$$S(\vec{r}, t) \propto \int \rho(\vec{r}) e^{i\gamma \vec{G}(t)\vec{r}t} \, \mathrm{d}\vec{r} \tag{2.36}$$

Thus the spatial information is stored in the accumulated phase of the signal. This dependency is preferably represented in the so-called *k-space*. The vector $\vec{k}$ represents the spatial frequencies inherent in the original object. It is defined as

$$\vec{k} = \frac{\gamma}{2\pi} \int_0^t \vec{G}(\tau) \, \mathrm{d}\tau. \tag{2.37}$$

This allows to rewrite equation (2.36) to

$$S\left(\vec{k}(t)\right) \propto \int \rho(\vec{r}) e^{i\vec{k}(t)\vec{r}} \, \mathrm{d}\vec{r}. \tag{2.38}$$

The Fourier transformation of equation (2.38) yields the spatial distribution of the nuclear spins $\rho(\vec{r}(t))$ in dependence of the NMR signal $S\left(\vec{k}(t)\right)$:

$$\rho\left(\vec{r}(t)\right) \propto \int S\left(\vec{k}(t)\right) e^{i\vec{k}(t)\vec{r}} \, \mathrm{d}\vec{k} \tag{2.39}$$

The complete acquisition of the k-space during an MR experiment is described in the following.

2.4.2. Slice selection

First, the external magnetic field B_0 is superimposed with a gradient in the z-direction $G(z)$. A gradient field of the form $G(z) = G_z \cdot z$ yields the Larmor frequency

$$\omega_0(z) = \gamma\left(B_0 + G_z \cdot z\right) \tag{2.40}$$

A precisely defined slice can then be selected by a narrow-band excitation of a particular Larmor frequency. The position of the slice is defined by the center frequency $\omega_{RF}(z)$, while the width depends on a finite bandwidth $\Delta\omega_{RF}$ and the gradient strength G_z:

$$\Delta z = \frac{\Delta\omega_{RF}}{2\pi\gamma G_z}. \tag{2.41}$$

2.4.3. Frequency encoding

An additional gradient can be applied in x′-direction ($G(x) = G_x \cdot x$) during the readout. Thereby the signal is also encoded in this direction and the spins precess with different Larmor frequencies in the x′-direction.

$$\omega_0(x') = \gamma \left(B_0 + G_{x'} \cdot x'\right) \tag{2.42}$$

Thus, the measured signal no longer consists of only one frequency but of the sum of all frequencies, the so-called frequency spectrum. Fourier transformation along the x′-direction yields the signal distribution associated to the frequency spectrum.

2.4.4. Phase encoding

To encode the missing spatial dimension (here y′), the phase of the precessing magnetization is manipulated. A linear gradient in the y′-direction is applied between excitation and readout. Consequently the magnetization accumulates a phase $\varphi(y')$, which is maintained during the readout

$$\varphi(y') = \frac{\gamma}{2\pi} \int G_{y'}(t) \cdot y \; \mathrm{d}t. \tag{2.43}$$

To obtain an image resolution of $N_{y'}$ data points in the y′-direction, the acquisition has to be repeated $N_{y'}$ times with different gradient strength G_y. An image can then be calculated by applying the two-dimensional Fourier transformation.

2.4.5. Specific absorption rate (SAR)

The RF pulses applied in NMR imaging induce energy in the sample. However, within the applied frequency range of $10 - 300\,\mathrm{MHz}$ this induction is several orders of magnitudes smaller than the binding energy of an electron in a molecule or even the existing hydrogen bonds. Thus, biological tissue is virtually transparent for the RF field and electrical and covalent structures of molecules in the human body are not affected. Nevertheless, electrical currents are induced in the tissue and transformed to heat by *Ohmic heating* [41]. Free charge carriers and molecular dipoles, which are set in motion by the alternating electric field, induce currents that are converted into heat.

The so-called *specific absorption rate* (SAR) is the approach that is often used to quantify the heating of the tissue. In an exposed volume V the value SAR is defined as:

$$SAR = \int \frac{\sigma(\vec{r}) \cdot \left|\vec{E}(\vec{r})\right|^2}{\rho(\vec{r})} \mathrm{d}\vec{r} = c\frac{\mathrm{d}T}{\mathrm{d}t} \tag{2.44}$$

with the electrical conductivity σ, the averaged electrical field $\vec{E}$, the volumetric mass density of the volume ρ, and the specific heat capacity c. To prevent damage of the tissue by excessive heating the exposure to RF magnetic fields in NMR is limited by law [48]. The SAR increases quadratically with the static magnetic field [49]. Thereby the safety margins are reached quickly in ultra-high field magnetic resonance experiments thereby restricting specific investigations.

2.5. Physiology

In this part the relevant biochemical and physiological fundamentals and aspects for this thesis are presented. This includes a brief outline of the cell energy metabolism and the anatomy of the human calf. For more information about these topics the reader is referred to the work of [50], [51] or [52].

2.5.1. Biochemical fundamentals of the energy metabolism

Every biological activity needs energy. The transient energy carrier in human cells is *adenosine triphosphate* (ATP). By hydrolytic breaking of the covalent-bound phosphate residues energy is produced:

$$\mathrm{ATP} + \mathrm{H_2O} \rightleftarrows \mathrm{ADP} + \mathrm{P_i} + \mathrm{H^+} + 12.6\,\mathrm{kJ/mol} \tag{2.45}$$

Since ATP is continuously consumed to ensure a proper cell work, it must be continuously regenerated. This is mainly done by the mitochondrial respiratory chain. A detailed explanation of this anaerobic and aerobic gylcolysis, however, exceeds the scope of this thesis and the interested reader is referred to e.g. [50].

The creatine-kinase (CK) reaction

In order to compensate short-time requirements of higher energy, buffer systems are necessary in the cell. For this purpose the phosphate group of the PCr can be transferred to ADP with the help of the enzyme creatine-kinase (CK) to regenerate ATP:

$$\mathrm{PCr} + \mathrm{ADP} + \mathrm{H^+} \rightleftarrows \mathrm{Cr} + \mathrm{ATP} \tag{2.46}$$

However, this extremely fast energy generation is only able to cover the increased energy need for a short time ($\sim 10\,\mathrm{s}$) [50]. For long-lasting energy consumption the substantial ATP synthesis has to take place. The recovering of PCr to the equilibrium concentration takes place during regeneration phases by the reversed CK-reaction under ATP consumption.

Metabolites

The following is an overview of the most important metabolites of the energy metabolism in the human body:

- **adenosin-5'-triphosphat** (ATP)
  is small molecule in the cell, which functions as the „molecular currency unit" of the energy metabolism. Dissociation into adenosine 5'-diphosphate (ADP) and inorganic phosphate (P_i) releases energy. To stabilize the molecule in the cell it is mostly bound in a chelate complex with Magnesium ions ($\mathrm{Mg^{2+}}$). The cells aims to maintain a constant ATP concentration by continuously regeneration via the mitochondrial respiratory chain or the creatine-kinase reaction.

- **phosphocreatine (PCr)**
  is used as a temporary storage of phosphate groups in the human energy metabolism. It serves as a short-time buffer for the ATP pool and can be used in the creatine-kinase reaction to enable a fast generation of energy.
- **creatine (Cr)**
  is the dephosphorylated form of PCr and is produced during the ATP production via the creatine-kinase reaction. Due to its guanidinium group, creatine has a special significance for the chemical exchange introduced in the following chapters.
- **anorganic phosphat (P_i)**
  is produced by the separation of phosphate groups from ATP and serves as a buffer in the physiological pH range.

2.5.2. Anatomy of the human calf muscle

The muscle system is suitable for examining energy metabolism and hence all in vivo measurements in this work have been carried out in the human calf. Muscle contractions often require a high amount of energy in the form of ATP. The additional energy required in the case of short or mild exercises is obtained mainly by the CK-reaction leading to a relative change in phosphocreatine and creatine concentration.
A schematic view of the human calf is shown in figure 2.4. Next to the bone structures, i.e. *tibia* and *fibula*, the achilles tendon (lat. *tendo calcaneus*) and vessel system, different muscles can be identified. These muscle groups, i.e. *musculus gastrocnemius*, *musculus soleus* and *musculus tibialis*, exhibit different compositions. In general, muscle fibers can differ in both their contractile properties, i.e. slow (type I) and fast (type II), as well as in their metabolism (aerobic or anaerobic) [51].

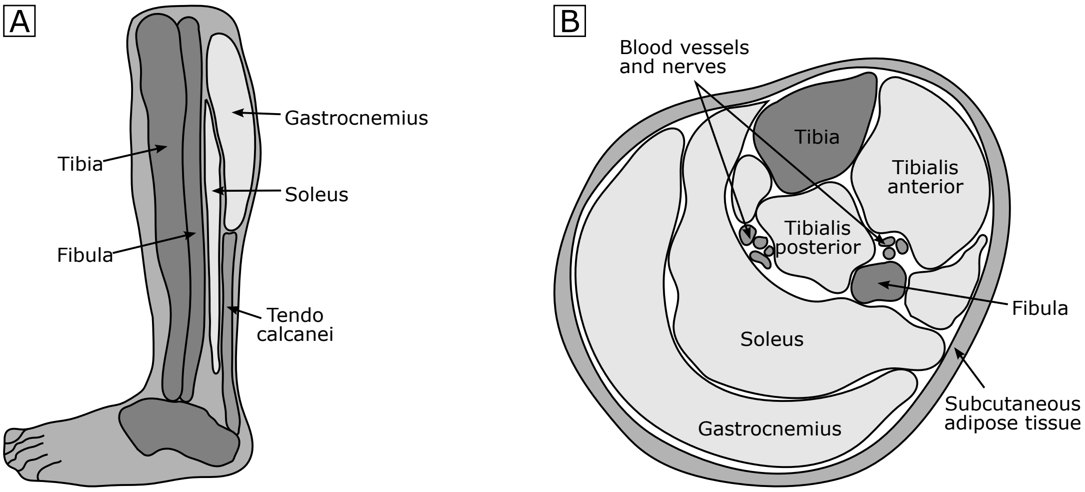

Figure 2.4.: Schematic structure of the human calf of a left leg. The bones, muscles and vessels as well as its rough arrangement are shown in a sagittal view of the calf (A) and a transverse cross section (B). Muscle groups are bright and bone structures dark. Reproduced and adapted with kind permission from [53].

3. The phenomenon CEST

Chemical Exchange Saturation Transfer (CEST) combines the signal acquisition of water protons with MR imaging and the chemical shift properties of MR spectroscopy. It enables the indirect detection of protons of metabolites of low concentration down to *millimolar* (mM) range. Magnetization transfer is used to accumulate a saturation in the large water proton signal ($c \approx 55.5\,\mathrm{M}$). This yields a signal gain, which can be expressed by the so-called *proton transfer enhancement* (PTE) and is governed by the longitudinal relaxation rate and the exchange rate along the magnetization transfer pathway: $PTE \approx k_{BA} \cdot T_{1A}$.

This chapter provides a short phenomenological explanation of CEST. The mathematical description will follow in chapter 4.

3.1. Pool model and exchange processes

So far, it has been assumed that all spins are in a magnetically similar environment. If several different spin systems are involved, interactions occur, which are not described by the relaxation model (section 2.2.2). Proton-spin systems with the same physical properties are grouped into so-called pools. The individual pools have the same relaxation parameters $R_{1i} := \frac{1}{T_{1i}}$ and $R_{2i} := \frac{1}{T_{2i}}$, the same resonance frequencies δ_i (chemical shift - section 2.3) and the same exchange rates k_{ij} with $i, j = A, B$. However, between two different pools, the values can differ. A simple two-pool model, describing the magnetization transfer between a pool A and a pool B, is schematically depicted in figure 3.1.

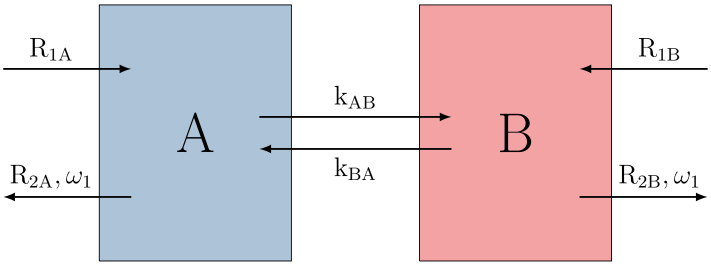

Figure 3.1.: The schematic structure of a 2-pool model is shown. The protons of each pools are characterized by the relaxation rates R_1 and R_2 and the frequency offset δ. There is an exchange between the pools, which is determined by the exchange rate k.

In the case of CEST spectroscopy or imaging, pool A is always assumed as the spins of protons bound to free water molecules. In watery solutions the interactions between the two pools can in principle be attributed to three different mechanisms:

Chemical Exchange

A physical exchange of protons can be induced by chemical reactions. Despite the change of chemical environment, the quantum mechanical properties of the nuclear spin is not affected leading to a magnetization transfer. This is called *Chemical Exchange* (CE) [54].

Dipolar interaction

Dipolar interactions between nuclear spins of coupled spin systems enable new cross relaxations. These new relaxation pathways allow the magnetization transfer between different pools. This is also known as the *Nuclear-Overhauser-Effect* (NOE) [55].

Molecular exchange

Molecules can be in a bound or a free state of motion depending on the macromolecular environment. Diffusion can lead to a change of this state, resulting in an alteration of the chemical shift and relaxation rates of the protons bound in the molecules. This in turn leads to a transfer of magnetization between two pools [9].

A more detailed description of the processes which are important for the CEST spectroscopy is given after an introduction of the CEST experiment.

3.2. Saturation Transfer

In the context of the magnetization transfer, the term saturation describes the destruction of the magnetization of a certain pool of nuclear spins. In the case of a complete saturation, the two energy states $|\alpha\rangle$ and $|\beta\rangle$ of a spin 1/2 ensemble are occupied equally. Hence the macroscopic magnetization of this system would be zero. The Saturation Transfer experiment utilizes this property. The protons of pool B, which transfer their magnetization to water protons (pool A), generate a partially saturated water magnetization. This difference results in a depolarization of pool A, since the spin population difference is smaller compared to the value given by the thermal-equilibrium of the Boltzmann distribution.
Saturation transfer can also be seen as an additional relaxation pathway induced by the saturation of a specific pool. This is indicated in the pool model in figure 3.1. In the rotating frame of reference (section 2.2.1) the longitudinal and transversal relaxation rates are then named $R_{1\rho}$ and $R_{2\rho}$, respectively. This spectral selective relaxation process can be described by the Bloch-McConnell equations. The mathematical description is given in chapter 4.

3.2.1. The Saturation Transfer experiment

The fundamental Saturation Transfer experiment consists of two blocks: (1) a frequency selective radio frequency (RF) saturation followed by (2) an imaging of the modified water signal (figure 3.2). Continuous-wave (cw) RF irradiation is used to saturate pool B. The saturation is defined by the duration t_{sat}, amplitude $B_1 = \omega_1 / (\gamma 2\pi)$ and the frequency offset $\Delta\omega$ to water. The selectivity in the frequency domain, called bandwidth bw, is thereby proportional to the inverse of the pulse duration: $bw \propto \frac{1}{t_{sat}}$. During and after the on-resonant saturation at the resonance frequency of pool B, magnetization is transferred to the water (pool A) by the mechanism introduced in section 3.1. Subsequently the readout of the modified z-component of the water signal is performed using standard imaging sequences.

3.2.2. Z-Spectrum

As already mentioned, the measured signal in CEST experiments is always the magnetization of the water protons. In order to quantify the exchange between the pools, the reduction of the z-magnetization of the water pool is the decisive value. Plotting the residual signal in dependency of the saturation offset $\Delta\omega$, i.e. irradiation frequency, and normalizing it with an

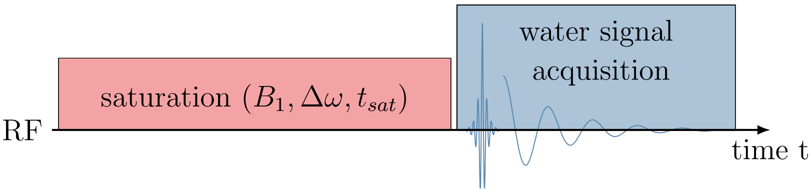

Figure 3.2.: The Saturation Transfer experiment consists of a frequency-selective saturation block (red) and the subsequent acquisition of the modified water signal (blue). A continuous-wave RF irradiation with duration t_{sat}, amplitude B_1 and at the frequency offset $\Delta\omega$ serves as saturation.

unsaturated signal M_0, the so-called *Z-spectrum* is obtained (figure 3.3) [56]. Note that for each point in the Z-spectrum an image has been taken and the saturation transfer experiment has to be carried out once.

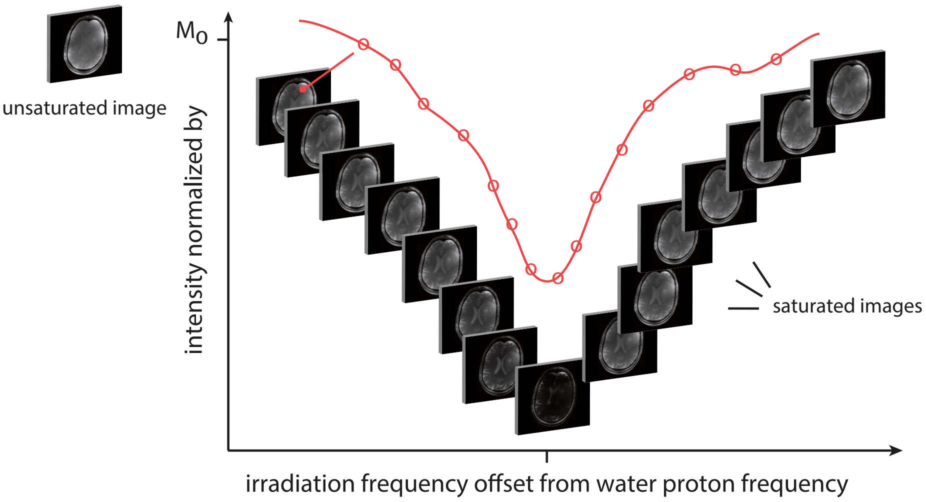

Figure 3.3.: The acquisition of the Z-spectrum is illustrated. For each frequency offset $\Delta\omega$ the experiment depicted in figure 3.2 is repeated. Normalization with an unsaturated image M_0 yields the Z-values in each voxel. Image reproduced and adapted with kind permission from *Zaiss and Bachert*, Phys. Med. Biol 2013; 58:221-269 [28].

3.3. CEST effects in vivo

The Z-spectrum in section 3.2 is a schematic illustration. Investigations of an in vivo system implies a lot of different effects. In the following the main contributions and properties of in vivo Z-spectra are described.

3.3.1. Modified frequency axis and direct water saturation

Figure 3.4 shows an in vivo Z-spectrum of a voxel selected in the white matter in the human brain. As conventionally done in ^{1}H spectroscopy, the frequency axis is plotted from upfield to downfield. The reference in CEST ($\Delta\omega_{ref} = 0\,\text{ppm}$) is chosen to be the resonance frequency

of protons of free water, resulting in a shift of $-4.7\,\text{ppm}$ of the frequency axis compared to ^{1}H spectroscopy [56].
The appearance of the Z-spectrum is dominated by the almost complete vanishing of the signal at $\Delta\omega = 0\,\text{ppm}$. This effect called *direct water saturation* originates in the direct irradiation at the water proton resonance [57]. The magnitude of this collapse depends mainly on the saturation amplitude and relaxation properties of the investigated spin system and can mathematically be described using the Bloch equations (section 2.2.2) [4].

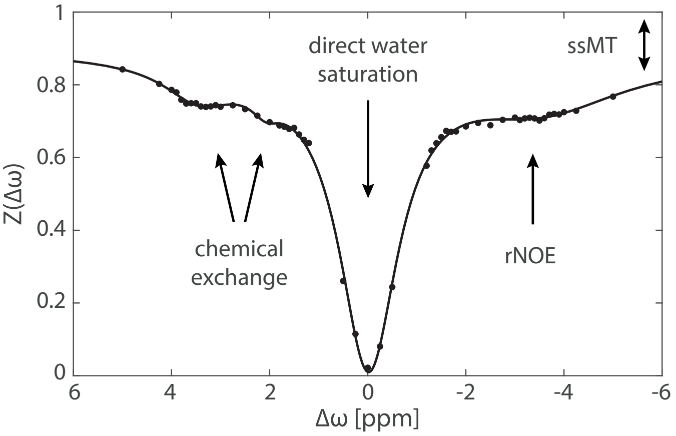

Figure 3.4.: An exemplary in vivo Z-spectrum of the human brain at $B_0 = 7\,T$ is shown. The effects due to chemical exchange and aliphatic protons (rNOE) are small in contrast to the direct water saturation and the semi-solid macromolecular magnetization transfer (ssMT).

3.3.2. Chemical exchange

Chemical exchange describes the physical transfer of protons from functional groups, e.g. amides, amines or hydroxyl groups, to water. The chemical shifts of these endogenous CEST effects are in the positive range, i.e. upfield from water in the Z-spectrum (figure 3.4). Due to the fact, that the chemical reactions governing the exchange are base- and/or acid-catalyzed, the exchange rate depends on pH and temperature and can vary from some s^{-1} to several 1000 s^{-1}. The resulting CEST effect depends mainly on the concentration and the exchange rate of the investigated functional group. This was shown by analytically solving the Bloch-McConnell equations (section 4.3). Various functional groups with different origins, and therefore specific offset frequency δ_i and exchange rate k_{BA}, were already reported (table 3.1). The main focus of this thesis is the investigation of the -NH$_2$ resonance at $\Delta\omega_B = 1.9 - 2\,\text{ppm}$ which is associated to creatine and protein contributions in tissue [13, 26, 58].

So far, only so-called *endogenous* CEST agents were discussed. These are all naturally occurring components of living tissue. However, there are also *exogenous* contrast agents that let arise a CEST effect. The research spans out from CT contrast agents, like *iopamidol* [63], to specifically manufactured chemical compounds that involve a signal enhancement. Some examples are paramagnetic tracers (PARACEST [22]) that possess large chemical shifts ($\Delta\omega_B \sim 100\,\text{ppm}$), compartmental hyper-polarized agents (HyperCEST [64]), or agents that are activated only under catalysis (CatalyCEST [65]).

solute/metabolite	functional group		δ_i [ppm]	k_{BA} [s^{-1}]
proteins [12, 59]	Amide	-NH	3.5	28.6 - 300
proteins [54]	Amine	$-NH_2$	2.0	700-10.000
glutamate [18]	Amine	$-NH_2$	3.0	5.500
creatine [13, 60]	Guanidinium	$-(NH_2)_2^+$	1.9	950 [pH 7.15, $T = 37°C$]
	Guanidinium	$-(NH_2)_2^+$	1.9	1190 [pH 7.0, $T = 37°C$]
phosphocreatine [61]	Guanidinium	$-NH_2$	1.8	140 [pH 7.0, $T = 37°C$]
	Amide	-NH	2.5	110 [pH 7.0, $T = 37°C$]
glucose [62] [pH 6.41, $T = 23°C$]	Hydroxyl	-OH	1.3	300
			2.2	30
			2.9	150
			~ 0.5	several thousands
lactate [21]	Hydroxyl	-OH	0.4	500
glycosaminoglycan [20]	Amide	-NH	3.5	'protein-like'
	Hydroxyl	-OH	1-2	1000

Table 3.1.: Selection of endogenous functional groups, their resonance frequencies δ_i and exchange rates k_{BA}. The values refer to in vivo conditions if not stated explicitly by pH and temperature T.

3.3.3. Semi-solid magnetization transfer (ssMT)

Macromolecular structures are present in vivo. These include rigid and mostly immobile components of the cell, i.e. the cell membrane, other surface proteins or the cytoskeleton. The interactions between free water molecules and the protons of this macromolecular matrix yield the so-called *semi-solid magnetization transfer* (ssMT) (figure 3.5a). During this process, water molecules can bind to the surface of the matrix (molecular exchange), which leads to a reduced mobility but, thereby, an increased correlation time. In contrast to the unbound state the inter-molecular exchange can no longer be neglected. The following transition to the free state allows the transfer of the magnetization to the water pool via diffusion. The resulting exchange rate of the ssMT is in the range of $k_{CA} \approx 40\,s^{-1}$ [46].

Due to the solid-like structure (these structures are not truly rigid, nevertheless, they have solid-like characteristics) these protons have very short relaxation times, i.e. T_2 in the range of a few μs, resulting in a line-width of several kHz. This broad resonance makes a direct detection difficult, but can be utilized to prepare a magnetization transfer contrast (MTC) even at large offset frequencies by an indirect measurement via the water signal [9, 66].

3.3.4. Exchange-relayed NOE (rNOE)

It was shown that relaxation processes can be induced by application of an oscillating RF field. In principle, however, any fluctuating magnetic field that oscillates near the Larmor frequency can alter the relative occupation of the nuclear spin states. In liquids the magnetic moment of a spin randomly affects the local field of another spin due to the Brownian molecular motion. Its fluctuating magnetic field can induce energy transitions and thus relaxation through space. The dipolar interactions of the nuclear spins are called *Nuclear-Overhauser-Effect* (NOE) and are described by the *Bloch-Solomon* equations [55]. These can be derived from the Bloch-McConnell equations by introducing the cross-relaxation rate σ, which depends on parameters such as correlation time τ_C or interaction distance r.

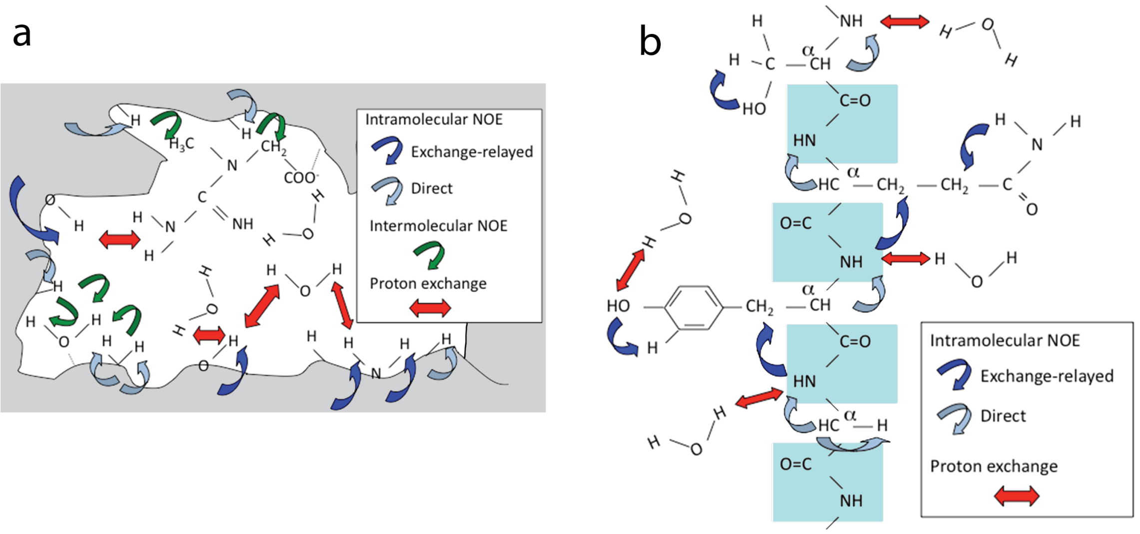

Figure 3.5.: Illustration of magnetization transfer pathways in proteins. a) Magnetization transfer can occur within the macromolecular matrix (gray background) via intra-molecular spin-diffusion processes (blue and gray arrows). Inter-molecular dipolar interactions (green arrows) as well as chemical exchange processes (red arrows) transfers the magnetization to water molecules, which are in a bound state to the macromolecular matrix. b) Magnetization is mediated by intra-molecular spin-diffusion processes (blue and gray arrows) from fixed protons ($-\mathrm{CH}_2-$) to chemical groups ($-\mathrm{NH}$, $-\mathrm{NH}_2$, $-\mathrm{OH}$) inside a macromolecule (e.g. proteins). The chemical exchange of protons (red arrows) with the surrounding water molecules allows the transport of the magnetization to water. This magnetization transfer path between water protons and non-exchanging covalently bound protons in macromolecules is called exchange-relayed NOE (rNOE). Reproduced with kind permission from *van Zijl and Yadav*, MRM 2011; 65(4):927-948 [67].

In the case of large organic macromolecules the protons are not only coupled to each other in intra-molecular and dipolar manner, but also with multiple other proton pools. This allows the equilibration of magnetization throughout the whole protein, called *spin diffusion*. Since free water molecules have only very short correlation times, the magnetization transfer by inter-molecular dipolar interactions with other molecules is very slow ($\sim 2-5\,\mathrm{s}^{-1}$ [68]). However, the combination of intra-molecular spin diffusion and subsequent inter-molecular exchange enables the transfer of magnetization from a non-exchanging proton to a proton which is in chemical exchange to water protons (figure 3.5b). This process is called *exchange-relayed NOE* (rNOE).

The rNOE of aliphatic protons is observed downfield from water in the range from $\Delta\omega_B = -2 - -5\,\mathrm{ppm}$. Recently, an additional peak at $\Delta\omega_B = -1.6\,\mathrm{ppm}$ attributed to the phosphor choline of the cell membrane was discovered in rat experiments [69] and also seen in high resolution CEST imaging of Glioblastoma patients [70]. Effects of aromatic protons upfield from water could also be observed in rat brain and pig brain tissue homogenate ($\Delta\omega_B = 1-4\,\mathrm{ppm}$) [71,72].

3.4. Limitations in CEST

The mechanisms generating the CEST contrasts (section 3.3) depend naturally on the properties of the investigated metabolite: the exchange rate and the relative concentration. However, also several other parameters contribute to the dimension of the CEST effects and their impact in the Z-spectrum. The nominal static magnetic field B_0 determines the spectral resolution, since the resonance frequencies are more or less separated from the water signal. Additionally, the longitudinal relaxation times are longer for higher magnetic fields yielding a longer storage of the saturation. Furthermore the saturation and relaxation parameter itself play an important role, which are described in the following sections.

3.4.1. B_1 and t_{sat} scaling – labeling efficiency

The saturation and thus the magnetization transfer to the water pool are directed by the parameters of the RF irradiation. These include mainly the saturation time t_{sat} and saturation amplitude B_1. The dependencies for a 2-pool-model are schematically illustrated in figure 3.6. The CEST effect increases with longer saturation time t_{sat} (figure 3.6A), the so-called *transient state*. If the saturation time is in the range of several T_1 (in the case of this simulations $T_1 = 2\,\text{s} \rightarrow t_{sat} \gtrsim 6\,\text{s}$) a so-called *steady-state* is reached. This is equivalently given for the direct water saturation and the magnetization transfer.
An increasing RF amplitude B_1 yields a more effective labeling of the CEST pool and therefore an increase in amplitude and width of the CEST effect (figure 3.6B). However, the direct water saturation is enhanced as well, which dilutes the CEST effect with increasing B_1. This so-called *spillover dilution* is clarified in more detail in the next section. From this it follows that for a specific CEST pool the saturation has to be adjusted to obtain an apparent effect in the Z-spectrum.

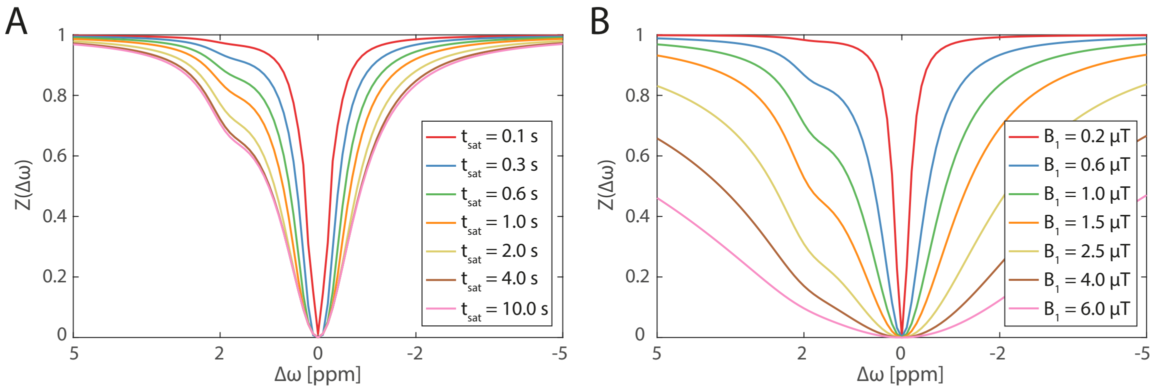

Figure 3.6.: Simulated Z-spectra of a 2-pool system ($\Delta\omega_A = 0\,\text{ppm}$, $\Delta\omega_B = 1.9\,\text{ppm}$) with constant relaxation times T_1 and T_2 at the static magnetic field $B_0 = 7\,\text{T}$ are shown.
A: Increasing saturation time t_{sat} with the same saturation amplitude $B_1 = 1.0\,\mu\text{T}$. B: Increasing saturation amplitude B_1 with the same saturation time $t_{sat} = 10\,\text{s}$.

When a whole image is acquired, an additional effect is important: field-inhomogeneities. Due to the comparable size of the RF wavelength and the diameter of the field-of-view (FoV), a severe reduction of the B_1 strength in the periphery compared with the isocenter can be observed [73]. The CEST effect will be over- or underestimated without the precise knowledge of the saturation amplitude and subsequent correction. A method to handle these inhomogeneities is presented in section 5.4.4.

3.4.2. T_1 and T_2 scaling – spillover dilution

Due to the indirect measurement, CEST effects are scaled with relaxation properties of the water pool (figure 3.7). On the one hand, this allows the accumulation of the saturation in the water pool and therefore an amplification of the CEST signal by the proton transfer enhancement (PTE), but on the other hand, the water relaxation affects and dilutes the signal. As already addressed in the previous section, the longitudinal relaxation time T_1 has an impact on the effective saturation of the CEST pool. It defines the time for the accumulation of saturation in the water pool. A longer T_1 yields a more apparent CEST effect in the steady-state for constant saturation length t_{sat} (figure 3.7A). Another disturbance, which influences the CEST signal, is the *spillover dillution.* The water pool is already directly saturated at the resonance frequency of pool B. Consequently, the magnetization of the water pool is lower, resulting in less water protons for the saturation transfer. Hence the direct water saturation yields a dilution of the CEST effect. The magnitude of the spillover dilution increases for increasing saturation amplitude B_1 (figure 3.7B) and decreasing transversal relaxation time T_2 (figure 3.7B).

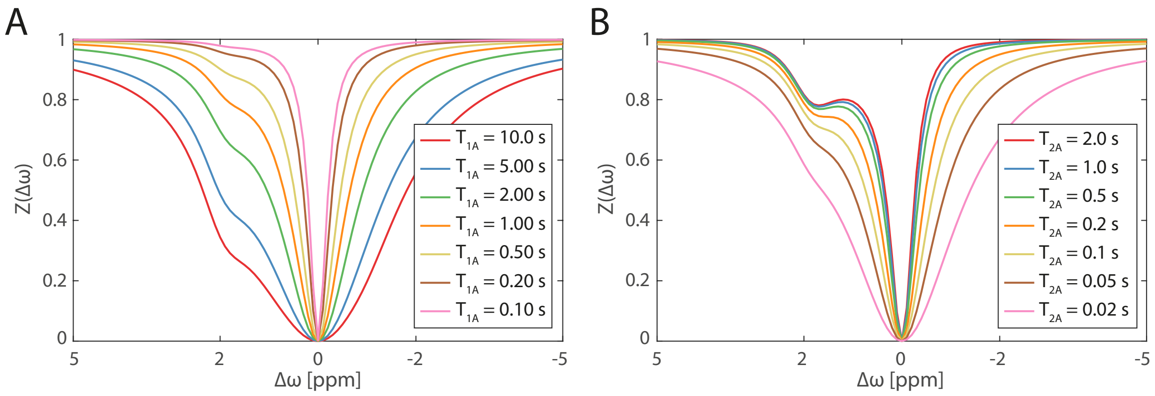

Figure 3.7.: Simulated Z-spectra of a 2-pool system ($\Delta\omega_A = 0\,\text{ppm}$, $\Delta\omega_B = 1.9\,\text{ppm}$) with constant saturation parameters t_{sat} and B_1 at the static magnetic field $B_0 = 7\,\text{T}$ in the steady-state are shown. A: Increasing longitudinal relaxation time T_1 with constant T_2. B: Decreasing transversal relaxation time T_2 with constant T_1.

3.4.3. Specific absorption rate on a whole body scanner

So far, only a cw saturation with a pulse duration of several seconds was assumed. On clinical whole-body scanners the duration of the RF saturation pulse is limited due to technical and safety reasons. These are mainly governed by limitations of the specific absorption rate (SAR), which limit the heat transport into the tissue (section 2.4.5). The pulse duration is restricted to $t_p \leq 100\,\text{ms}$ for the whole-body tomograph used in this work [74]. Consequently, saturation pulses are interleaved with interpulse delays to maintain the SAR within allowed values. This results in disadvantages such as a lower labeling efficiency or a more complex theoretical description compared to the cw saturation. Additionally, the optimization of CEST experiments is more complicated since several parameters, such as number of pulses n, pulse duration t_p, interpulse delay t_d and pulse shape have to be considered. However, pulsed saturation also allows to use sophisticated measurement methods, like varying rotation angles (CERT [75], VDMP [76]) or tunable transfer modules (TTM [68]).

3.5. Motivation and challenges

CEST depends on a large set of parameters complicating a comparison between different measurements. The only two parameters given by the CEST agent itself are the exchange rate and relative concentration. A quantitative measurement of these two variables would be an important step towards a comparability between different studies. In a clinical setup, the saturation scheme is limited to a series of short pulses to follow regulation of the specific absorbtion rate. Addtionally, pulsed saturation is difficult to describe theoretically, thus rendering quantitative CEST, a challenging task.

In this thesis an analytical model will be presented that permits deeper insight into pulsed CEST experiments. It furthermore allows to extend a known and in the case of cw saturation established method to the case of pulsed saturation, yielding separately, and independently, the exchange rate and the relative proton concentration.

4. Theory

For a more detailed description on Magnetization transfer and CEST the reader is referred to the review articles [67,77,78] or the book *Chemical Exchange Saturation Transfer Imaging* [79]. Everything discussed in this section is already known in the CEST community and not part of this thesis. The new theoretical approach investigated in this work will be presented in chapter 6.

4.1. Chemical Exchange

The chemical exchange between protons bound in proteins, solutes or metabolites and water is governed by acid-base-reactions. These chemical reactions are characterized by the exchange rate k_{BA} between the solute pool (B) and the pool of free water protons (A). For a first order chemical reaction (proportionality to concentration [80]) this rate can be approximated by [12, 54]:

$$k_{BA} = k_{base} \cdot \left[OH^-\right] + k_{acid} \cdot \left[H_3O^-\right] + k_{buffer} \tag{4.1}$$

where k_{base}, k_{acid} and k_{buffer} are the base-, acid- and buffer-catalyzed reaction rates, respectively. $[OH^-]$ and $[H_3O^+]$ are the hydroxyl- and oxonium-ion concentrations. For the sake of simplicity k_{buffer} comprises all other catalysis mechanisms. All three reaction rates k exhibit a exponential temperature dependence that is mathematically given by the *Arrhenius law* [81]. Equation (4.1) can be rewritten using the definition of the pH value and dissociation constant of water pK_w to [80]:

$$k_{BA}(pH, T) = k_{base}(T) \cdot 10^{pH - pK_w(T)} + k_{acid}(T) \cdot 10^{pH} + k_{buffer}(pH, T, c_{buffer}) \tag{4.2}$$

It is obvious that the exchange rate can increase and decrease with pH. The dependency and dominating process change for different functional groups with pH (figure 4.1).

For in vivo like systems it was shown that the exchange of amide and amine groups is mainly base-catalyzed [12]. In this thesis the exchange of amine protons to water is studied, which can be approximated as

$$k_{BA}^{Amine} = 10^{pH - \mathcal{K}} \tag{4.3}$$

At temperature $T = 37°\mathrm{C}$ *Desmond et al.* [84] and *McVicar et al.* [85] determined an experimental value of $\mathcal{K} = 4.2$ and $\mathcal{K} = 4.4$, respectively.

4.2. The Bloch-McConnell equations

The dynamic of the magnetization of a coupled spin-system under RF irradiation can be described by an extension of the classical Bloch equations (2.24)-(2.26) with exchange terms.

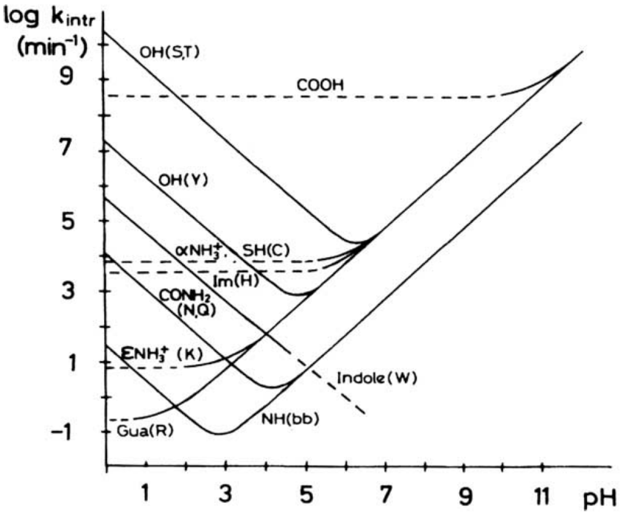

Figure 4.1.: The exchange rate k_{BA} (here called k_{intr}) of different functional groups within amino acids as a function of pH is shown for $T = 25°C$. The amino acids are identified by the one-letter code [82] and (bb) denotes the backbone of the amino acid chain. Image reproduced with kind permission from [83].

The resulting equations are called Bloch-McConnell equations [86]. In the case of a 2-pool system with pool A and B they are given by:

$$\frac{\mathrm{d}}{\mathrm{dt}}M_{xA} = -\Delta\omega_A M_{yA} \quad - R_{2A}M_{xA} \quad + k_{BA}M_{xB} - k_{AB}M_{xA} \tag{4.4}$$

$$\frac{\mathrm{d}}{\mathrm{dt}}M_{yA} = +\Delta\omega_A M_{xA} \quad - R_{2A}M_{yA} - \omega_1 M_{zA} \quad + k_{BA}M_{yB} - k_{AB}M_{yA} \tag{4.5}$$

$$\frac{\mathrm{d}}{\mathrm{dt}}M_{zA} = +\omega_1 M_{yA} \quad - R_{1A}\left(M_{zA} - M_{zA,0}\right) \quad + k_{BA}M_{zB} - k_{AB}M_{zA} \tag{4.6}$$

$$\frac{\mathrm{d}}{\mathrm{dt}}M_{xB} = -\Delta\omega_B M_{yB} \quad - R_{2B}M_{xB} \quad - k_{BA}M_{xB} + k_{AB}M_{xA} \tag{4.7}$$

$$\frac{\mathrm{d}}{\mathrm{dt}}M_{yB} = +\Delta\omega_B M_{xB} \quad - R_{2B}M_{yB} - \omega_1 M_{zB} \quad - k_{BA}M_{yB} + k_{AB}M_{yA} \tag{4.8}$$

$$\frac{\mathrm{d}}{\mathrm{dt}}M_{zB} = +\omega_1 M_{yB} \quad - R_{1B}\left(M_{zB} - M_{zB,0}\right) \quad - k_{BA}M_{zB} + k_{AB}M_{zA} \tag{4.9}$$

The equations (4.4)-(4.6) and (4.7)-(4.9) describe the dynamics of pool A and pool B, respectively. The parameter R_{1i} and R_{2i} are the relaxation rates of the particular pool as defined in section 3.1, $\omega_1 = \gamma B_1$ is the amplitude of the RF irradiation and $\Delta\omega_i$ is the shift of the RF irradiation frequency $\Delta\omega$ and the Larmor frequency δ_i of pool i: $\Delta\omega_i = \Delta\omega - \delta_i$. If the water pool is chosen as reference, $\Delta\omega$ is denominated as the frequency offset and given in *ppm* (section 2.3). Both pools are coupled in the exchange terms by the exchange rates k_{AB} and k_{BA} as follows:

$$k_{AB} \cdot M_{zA,0} = k_{BA} \cdot M_{zB,0}. \tag{4.10}$$

The magnetizations at thermal equilibrium $M_{zA,0}$ and $M_{zB,0}$ define the relative population difference. In the following this ratio is called *relative concentration*:

$$f_B = \frac{M_{zB,0}}{M_{zA,0}}. \tag{4.11}$$

In the literature the relative concentration is sometimes also given by the term *proton fraction*. Combining equations (4.11) and (2.14) yields a correlation between the relative concentration and the total number of spins N_i in both pools. Hence, the relative concentration is a function of the molecular concentration c and the number of protons per molecule n:

$$f_B = \frac{N_B}{N_A} = \frac{c_B \cdot n_B}{c_A \cdot n_A}. \tag{4.12}$$

The given characterization of a 2-pool system can easily be adapted for more pools. Each added pool (labeled C,D,E...) leads to three additional equations, i.e. one for each spatial orientation. In the case of magnetization transfer (from now on called pool C, without loss of generality) only a dependency of the z-magnetization is apparent, since the x- and y-orientation are negligible due to the high relaxation rate R_{2C}. An intra-molecular exchange between different pools besides water is neglected.

4.3. Analytical Solution of the Bloch-McConnell equations

The Bloch-McConnell equations are a coupled system of first-order linear differential equations. An analytical solution can be obtained using an eigenspace approach [38, 77, 87]:

$$\vec{\mathrm{M}}(t) = \sum_{n=1}^{6} e^{\lambda_n t} \vec{\nu}_n + \vec{\mathrm{M}}^{ss} \tag{4.13}$$

where $\vec{\mathrm{M}}(t)$ is the magnetization vector of the 2-pool system, λ_n are the eigenvalues and $\vec{\nu}_n$ are the eigenvectors. The parameter $\vec{\mathrm{M}}^{ss}$ specifies the steady-state solution of the magnetization (section 3.4). Under the assumption of a sufficiently long saturation $t_{sat} \gg T_{2A}$, the only relevant contribution to the magnetization vector of water $\vec{M}_A$ is the eigenvalue λ_1. The corresponding eigenvector $\vec{\nu}_1$ is collinear with the effective magnetic field $\vec{B}_{eff}$ (equation (2.21)). This simplifies the description of CEST experiments from several coupled differential equations to a one-dimensional system. It was shown that the eigenvalue λ_1 of the Bloch-McConnell equations can be approximated by the negative longitudinal relaxation rate in the rotating frame [38, 87]

$$\lambda_1 \approx -R_{1\rho}. \tag{4.14}$$

Hence, the water magnetization decays alongside the axis of the effective magnetic field $\vec{B}_{eff}$ with the rate $R_{1\rho}$. In the case of a 2-pool system consisting of a water pool (pool A) in chemical exchange with a solute pool (pool B), the longitudinal relaxation rate is given by

$$R_{1\rho}(\Delta\omega) = R_{eff}(\Delta\omega) + R_{ex}(\Delta\omega) \tag{4.15}$$

in which R_{eff} describes the relaxation rate of the water pool, while R_{ex}, the exchange-dependent relaxation rate, depicts the influence due to pool B. This reflects the mathematical description of the notion that chemical exchange or dipolar interactions introduce additional relaxation pathways, as already adressed in section 3.2. Without the perturbation of pool B, the longitudinal relaxation in the rotating frame would read [87]:

$$R_{1\rho}(water) = R_{eff}(\Delta\omega) = R_{1A}\cos^2\Theta + R_{2A}\sin^2\Theta \tag{4.16}$$

$$= R_{1A} + (R_{2A} - R_{1A})\,\frac{\omega_1^2}{\omega_1^2 + \Delta\omega^2} \tag{4.17}$$

with the relaxation rates R_{1A} and R_{2A}, and the angle $\Theta = \arctan\left(\frac{\omega_1}{\Delta\omega}\right)$ between the two magnetic fields $\vec{B}_{eff}$ and $\vec{B}_0$.
The analytical eigenspace approach allows to derive the water magnetization at any given time $M_{zA}\left(\Delta\omega, t_{sat}\right)$. Normalization with the equilibrium magnetization $M_{zA,0}$ yields the full solution of the z-magnetization after irradiation with duration t_{sat} at the frequency offset $\Delta\omega$

$$Z\left(\Delta\omega, t_{sat}\right) = \frac{M_{zA}\left(\Delta\omega, t_{sat}\right)}{M_{zA,0}} \tag{4.18}$$

$$= \left[Z_i\cos^2\Theta(\Delta\omega) - Z^{ss}(\Delta\omega)\right]e^{-R_{1\rho}t_{sat}} + Z^{ss}(\Delta\omega) \tag{4.19}$$

where Z_i is the initial magnetization value and the steady-state magnetization Z^{ss} is given by

$$Z^{ss}(\Delta\omega) = \frac{R_{1A}\cos^2\Theta(\Delta\omega)}{R_{1\rho}(\Delta\omega)}. \tag{4.20}$$

Hence, neglecting pool B allows to derive the steady-state Z-spectrum of the direct water saturation

$$Z_A^{ss}(\Delta\omega) = \frac{R_{1A}\cos^2\Theta(\Delta\omega)}{R_{eff}(\Delta\omega)} = 1 - \underbrace{\frac{\Gamma_A^2/4}{\Gamma_A^2/4 + \Delta\omega^2}}_{\mathcal{L}_A(\Delta\omega)}. \tag{4.21}$$

The Lorentzian-like function $\mathcal{L}_A(\Delta\omega)$ has a *full-width-at-half-maximum* (FWHM or Γ) given by

$$\Gamma_A = 2\omega_1\sqrt{\frac{R_{2A}}{R_{1A}}}. \tag{4.22}$$

In general the exchange-dependent relaxation rate in the rotating frame R_{ex} is not easy to calculate. However, assuming that the longitudinal relaxation rate of pool B is much smaller than the transversal relaxation rate ($R_{1B} \ll R_{2B}$) and the exchange rate ($R_{1B} \ll k_{BA}$), and the back exchange k_{AB} can be neglected, which is reasonable for $M_{zA,0} \gg M_{zB,0}$, allows to obtain the following formula [77]:

$$R_{ex} = f_B\left[k_{BA}\frac{\delta\omega_B^2}{\omega_1^2 + \Delta\omega^2}\cdot\frac{\omega_1^2}{\frac{\Gamma_B^2}{4} + \Delta\omega_B^2} + R_{2B}\frac{\omega_1^2}{\frac{\Gamma_B^2}{4} + \Delta\omega_B^2} + k_{BA}\sin^2\Theta\frac{R_{2B}(R_{2B} + k_{BA})}{\frac{\Gamma_B^2}{4} + \Delta\omega_B^2}\right] \tag{4.23}$$

with the FWHM

$$\Gamma_B = 2\sqrt{\frac{k_{BA} + R_{2B}}{k_{BA}}\omega_1^2 + \left(k_{BA} + R_{2B}\right)^2} \tag{4.24}$$

and the saturation and chemical shift dependent frequency offset $\Delta\omega_B = \Delta\omega - \delta\omega_B$. Assuming a large chemical shift for pool B ($\delta\omega \gg \omega_1$) the so-called *large-shift* limit (LS) is reached, and again a Lorentzian-like function at the frequency $\delta\omega_B$ can be obtained

$$R_{ex,LS}(\delta\omega_B) = R^{max}_{ex,LS} \frac{\Gamma^2/4}{\Gamma^2/4 + (\Delta\omega - \delta\omega_B)2} \tag{4.25}$$

For most experiments conducted in this thesis ($B_0 \geq 7\,\mathrm{T}$ and $B_1 \leq 2\,\mu\mathrm{T}$) the large-shift limit is no longer valid, if the chemical shift is below $|\delta\omega_B| \leq 1\,\mathrm{ppm}$. The exchange-dependent relaxation rate maximizes at the chemical shift of pool B ($\Delta\omega = \delta\omega_B$):

$$R^{max}_{ex,LS} = f_B k_{BA} \frac{\omega_1^2}{\omega_1^2 + k_{BA}(k_{BA} + R_{2B})} \tag{4.26}$$

Equation (4.25) is in accordance with the weak-saturation-pulse calculations of *Sun et al.* [25] (Appendix A). It becomes clear from this equation, that the steady-state CEST signal depends next to the relative concentration f_B and the exchange rate k_{BA}, also on a term describing the RF irradiation. As already noted in section 3.4 the influence of the saturation on the CEST effect is named labeling. Consequently, this term α is called *labeling efficiency* and is given by:

$$\alpha_{LS}(\omega_1) = \frac{\omega_1^2}{\omega_1^2 + k_{BA}(k_{BA} + R_{2B})} \tag{4.27}$$

Introduced by *Sun et al.* [88] this parameter can have values between 0 and 1. In figure 4.2 the labeling efficiency for different exchange rates k_{BA} is plotted as a function of the saturation amplitude B_1. Additionally to the result of the large-shift limit, also the general solution, which depends on the chemical shift $\delta\omega_B$ (Appendix B), is depicted. The labeling efficiency, and hence the CEST effect, increases with a higher saturation amplitude. In the case of the large-shift limit no maximum is reached, however, when the full solution (equation (B.16)) is used the labeling efficiency reaches an optimum for a specific B_1. Nevertheless, the large-shift limit describes the behavior of all investigated CEST systems in this thesis sufficiently well

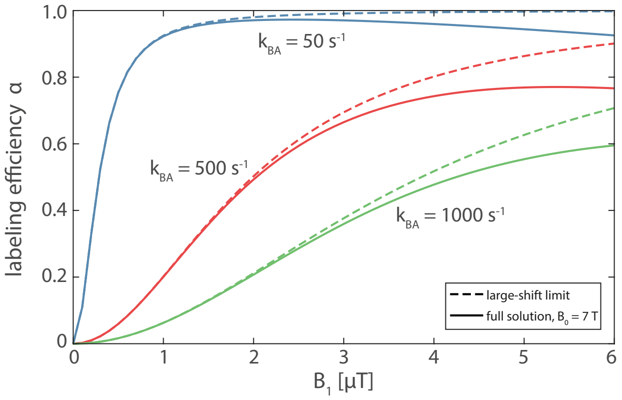

Figure 4.2.: The labeling efficiency α as a function of the saturation amplitude B_1. The large-shift limit (equation (4.27), dashed line) is shown as well as the full solution (equation (B.16), line) for different exchange rates k_{BA}. For the calculations the following amine-like parameters were used: $\delta_B = 1.9\,\mathrm{ppm}$, $f_B = 2‰$, $R_{2B} = 66.6\,\mathrm{s}^{-1}$.

4.4. Systems with multiple exchanging pools

As already discussed, the in vivo Z-spectrum is formed by several overlaying effects. This can be described by an extension of the analytical model. Under the assumption of small relative concentrations (f_i in the range of several percent) and no exchange between the solute pools (i.e. $k_{ij} = 0$ with $i, j \neq A$) the exchange-dependent relaxation rates $R_{ex,i}$ simply add up:

$$R_{1\rho} = R_{eff} + \sum_i R_{ex,i}. \tag{4.28}$$

The sum represents all different magnetization transfer pathways, including the semi-solid magnetization transfer, the exchange-relayed rNOE and the conventional chemical exchange (section 3.3). This extension allows to obtain the steady-state solution for the Z-spectrum from equation (4.20):

$$Z^{ss}(\Delta\omega) = \frac{R_{1A}\cos^2\Theta}{R_{eff} + \sum_i R_{ex,i}} \tag{4.29}$$

A Taylor expansion can be applied to equation (4.29) yielding the following equation in the large-shift limit [77]

$$Z^{ss}_{LS}(\Delta\omega) \approx \frac{R_{1A}\cos^2\Theta}{R_{eff}} - \frac{\sum_i R_{ex,i}}{R_{1A}} \tag{4.30}$$

From equation (4.21) it becomes clear, that theoretically the Z-spectrum is given by 1 minus the direct water saturation and minus the sum of the different solute pools. As given in equation (4.25) these CEST effects can also be approximated by a Lorentzian line-shape. Consequently, a Z-spectrum with several overlaying effects can be approximated by an summation of Lorentzian functions [31, 89, 90]:

$$Z^{ss}_{LS}(\Delta\omega) \approx 1 - \mathcal{L}_A - \sum_i \mathcal{L}_i \tag{4.31}$$

It has to be noted that the semi-solid magnetization transfer is, depending on the application and system characteristics, in the literature often described by other functions. These include Gaussian-shaped [91] or Super-Lorentzian shaped functions [92, 93]. However, for the investigation performed in this thesis a simple Lorentzian line-shape is sufficient.

4.5. Z-spectrum analysis

For a quantitative investigation of Z-spectra the separation of the designated CEST effect $R_{ex,i}$ from the direct water saturation R_{eff} and other confounding effects ($R_{ex,j}$, with $j \neq i$) is necessary. The steady-state z-value, the so-called *label scan* Z_{lab}, is defined as given in equation (4.29):

$$Z^{ss}_{lab}(\Delta\omega) = \frac{R_{1A}\cos^2\Theta}{R_{eff} + R_{ex,i} + \sum_{j,j\neq i} R_{ex,j}}. \tag{4.32}$$

Additionally a *reference scan* Z_{ref} is introduced, which does not contain the designated CEST effect, but all other contributions:

$$Z^{ss}_{ref}(\Delta\omega) = \frac{R_{1A}\cos^2\Theta}{R_{eff} + \sum_{j,j\neq i} R_{ex,j}}. \tag{4.33}$$

Since the exchange-dependent relaxation rate R_{ex} appears in the denominator of both equations, a subtraction of the inverse z-values is the logical conclusion and yields the magnetization transfer rate MTR_{Rex} [38]:

$$\begin{aligned} MTR_{Rex} &= \frac{1}{Z_{lab}} - \frac{1}{Z_{ref}} \qquad (4.34)\\ &= \frac{R_{ex}}{R_{1A}\cdot\cos^2\Theta} \qquad (4.35) \end{aligned}$$

This value is clearly free of influences of the direct water saturation or other confounding effects. A simple multiplication with the R_{1A} allows to correct for water relaxation properties and yields the so-called *apparent exchange-dependent relaxation* rate AREX [27]:

$$\begin{aligned} AREX := MTR_{Rex}\cdot R_{1A} &= \cdot\left(\frac{1}{Z_{lab}} - \frac{1}{Z_{ref}}\right)\cdot R_{1A} \qquad (4.36)\\ &= \frac{R_{ex}}{\cos^2\Theta} \qquad (4.37) \end{aligned}$$

Aside from the factor $\cos^2\Theta = \frac{\Delta\omega^2}{\Delta\omega^2+\omega_1^2}$, AREX represents a full quantitative approach to determine the CEST effect. In other publications AREX is sometimes called $\mathrm{CESTR_{ind}}$ (*CEST ratio inverse difference*) [35, 94]. Different methods to obtain the reference value Z_{ref} are discussed in section 5.4.3.

4.6. Quantitative CEST

In the last section a theoretical way to determine the quantitative CEST signal R_{ex} was introduced. However, as given in equation (4.26), the signal itself depends on properties of the pool, namely the exchange rate k_{BA} and relative concentration f_B, as well as the labeling efficiency α (section 3.4 and equation (4.27)). Several methods have been developed to determine the exchange rate and the relative concentration. The FWHM Γ (equation (4.24)) can be used to calculate the exchange rate directly [95]. Also, the dispersion of the CEST effect with the saturation amplitude ω_1 enables other approaches, like QUESP [30] or the numerical fitting of Z-spectra [28].
Dixon et al. [34] could even show that the there is a linear dependency of the CEST effect with the inverse of the squared saturation amplitude $1/B_1^2$. Hence a linear regression in the so-called *Ω-plot* allowed a simple quantification. However, these derivations were only valid for PARACEST agents, since it required large chemical shifts to circumvent the direct water saturation. It was shown that the inverse metric (equation (4.34)), which corrects for the spillover effect, is compatible with the Ω-plot method. This allowed to investigate endogenous CEST agents with small chemical shifts. For such a solute pool the on-resonant CEST effect is given by:

$$AREX = R^{on-resonant}_{ex,LS} = f_B k_{BA}\frac{\omega_1^2}{\omega_1^2 + k_{BA}\left(k_{BA} + R_{2B}\right)} \tag{4.38}$$

Inversion leads to the definition of the relaxation-compensated Ω-plot:

$$\frac{1}{AREX} = \underbrace{\frac{k_{BA}+R_{2B}}{f_B}}_{m} \cdot \frac{1}{\omega_1^2} + \underbrace{\frac{1}{f_B k_{BA}}}_{n} . \tag{4.39}$$

with the slope m and y-intersection n. Determination of m and n by fitting this linear relation allows to quantify the exchange rate k_{BA} and relative concentration f_B by the following equations [35]:

$$k_{BA} = \left(-\frac{R_{2B}}{2} + \sqrt{\frac{R_{2B}^2}{4} + \frac{m}{n}}\right) \tag{4.40}$$

$$f_B = \frac{1}{n \cdot \left(-\frac{R_{2B}}{2}\sqrt{\frac{R_{2B}^2}{4} + \frac{m}{n}}\right)} \tag{4.41}$$

4.7. Pulsed saturation

So far, the theory is only valid for cw technical and safety limitations on whole-body scanners require the introduction of a pulsed saturation. Therefore the saturation consists of pulses with duration t_p, which are interleaved with pulse delays of duration t_d. These two parameters are merged into the so-called *duty cycle* (DC):

$$DC = \frac{t_p}{t_p + t_d}. \tag{4.42}$$

Assuming a decay of the z-magnetization of water with $R_{1\rho}$ during saturation and with R_{1A} during the inter-pulse delay alters equation (4.20) in the steady-state to (Appendix C):

$$Z_{pulsed}^{ss}(\Delta\omega) = \frac{R_{1A}\,(1 - DC + DC \cdot \cos\Theta)}{R_{1A}(1 - DC) + R_{1\rho} DC} \tag{4.43}$$

If the inter-pulse delay t_d vanishes, i.e. $DC = 1$, equation (4.20) is obtained. The apparent exchange-dependent relaxation AREX is consequently scaled by the DC

$$\begin{aligned} AREX_{pulsed}^{on-resonant} &= DC \cdot \frac{R_{ex}}{\cos^2\Theta} \\ &= DC \cdot f_B k_{BA} \cdot \frac{\omega_1^2}{\omega_1^2 + k_{BA}\,(k_{BA} + R_{2B})} \end{aligned} \tag{4.44}$$

and remains thereby a quantitative parameter. This change can then be transferred into the Ω-plot method:

$$k_{BA} = \left(-\frac{R_{2B}}{2} + \sqrt{\frac{R_{2B}^2}{4} + \frac{m}{n}}\right) \tag{4.45}$$

$$f_B = \frac{1}{DC \cdot n \cdot \left(-\frac{R_{2B}}{2}\sqrt{\frac{R_{2B}^2}{4} + \frac{m}{n}}\right)} \tag{4.46}$$

5. Materials and Methods

This chapter introduces the equipment, software and basic methods used in this thesis. The programming of the software, which includes the import of DICOM (*Digital Imaging and Communications in Medicine*) images, evaluation algorithms or numerical simulations, was conducted in MATLAB (The MathWorks, Natick MA, USA) on a 3.2 GHz dual core CPU. Actual fitting was performed using a C-code based Levenberg-Marquardt optimizer (*levmar* [96]). C++ programming within the Siemens software development environment IDEA (Siemens Healthcare, Erlangen, Germany) allowed implementing different pulse shapes for saturation.

5.1. Numerical simulation of the Bloch-McConnell equations

The algorithm used to solve the Bloch-McConnell equations is based on fact, that the equation system can be written as a matrix equation, which is given by:

$$\frac{\mathrm{d}\overrightarrow{M}}{\mathrm{dt}} = \mathbf{A}(\mathbf{t})\overrightarrow{M}(t) + \overrightarrow{B} \tag{5.1}$$

Assuming a time-constant RF pulse with the saturation amplitude ω_1, the matrix equation (5.1) can be solved with the exponential approach as follows:

$$\overrightarrow{\mathrm{M}} = \left[\overrightarrow{\mathrm{M}}_0 + \mathbf{A}^+\overrightarrow{B}\right] e^{\mathbf{A}t} - \mathbf{A}^+\overrightarrow{B} \tag{5.2}$$

where $\mathbf{A}^+$ is the pseudo-inverse of the matrix $\mathbf{A}$. The expression $e^{\mathbf{A}}$ can be calculated in MATLAB via the eigenvalue decomposition and the term $\mathbf{A}^+\overrightarrow{B}$ with the left division by $\mathbf{A}/\overrightarrow{B}$. Due to the restriction to time-independent ω_1, this method is only suitable for the case of cw saturation. However, using a temporal discretization of $\omega_1(t)$, it is possible to perform the method for any arbitrary pulse form, e.g. Sinc or Gaussian-shaped pulses. For this purpose, the RF pulse is split into 200 parts, where ω_1 and the matrix $\mathbf{A}$ are assumed as constant in time in each segment [97].
In the case of pulsed saturation the amplitude ω_1 of the mandatory pause between the pulses is set to zero. The resulting matrix $\mathbf{A_{pause}}$ is thus independent of time and equation (5.2) can be solved. Hence, the matrix method is a suitable method to solve the Bloch-McConnell equations numerically in the case of continuous or pulsed saturation with any time-dependent saturation pulse. Exemplary simulation parameter for creatine are shown in table 5.1.

5.2. NMR measurement systems

The measurements and investigations in this work have been carried out on two different MR systems: First the whole-body scanner MAGNETOM 7T from Siemens, and second the NMR spectrometer Avance II from Bruker. While a system of three orthogonal gradient coils provides spatial resolution, additional shim coils serve to homogenize the magnetic field.

Pool		δ_i [ppm]	R_{1i} [s^{-1}]	R_{2i} [s^{-1}]	f_i	k_{iA} [s^{-1}]
Pool A	PBS-solution	0	0.24	0.83	1	$\sum_i f_i k_{iA}$
	muscle	0	0.54	20.0	1	$\sum_i f_i k_{iA}$
Pool B	creatine (pH 7.0)	1.9	R_{1A}	66.66	2.0‰	950

Table 5.1.: Typical parameter for Bloch-McConnell simulations of the water pool A and metabolite pool B. Estimation for transversal relaxation rate R_{2B} of pool B is from [25]; all other values taken from [13, 46] and if necessary adapted to $B_0 = 7\,T$.

5.2.1. 7 T whole body MRI scanner

The MAGNETOM 7 T whole-body scanner from Siemens (Siemens Healthineers, Erlangen, Germany) has a basic magnetic field strength of $B_0 \approx 7\,\mathrm{T}$. The actual ^{1}H resonance frequency of the systems is $\nu_0 = 297.18\,\mathrm{MHz}$. A 28-channel knee coil (Quality Electrodynamics, Mayfield, OH, USA) was used for RF irradiation and signal acquisition in vitro as well as in vivo. The temperature of the phantoms was stabilized using an MR-compatible thermos flask (Coleman Jug 1.8 L) containing 1.8 L of water. At least one automatic 3D shim was performed before the CEST experiments.

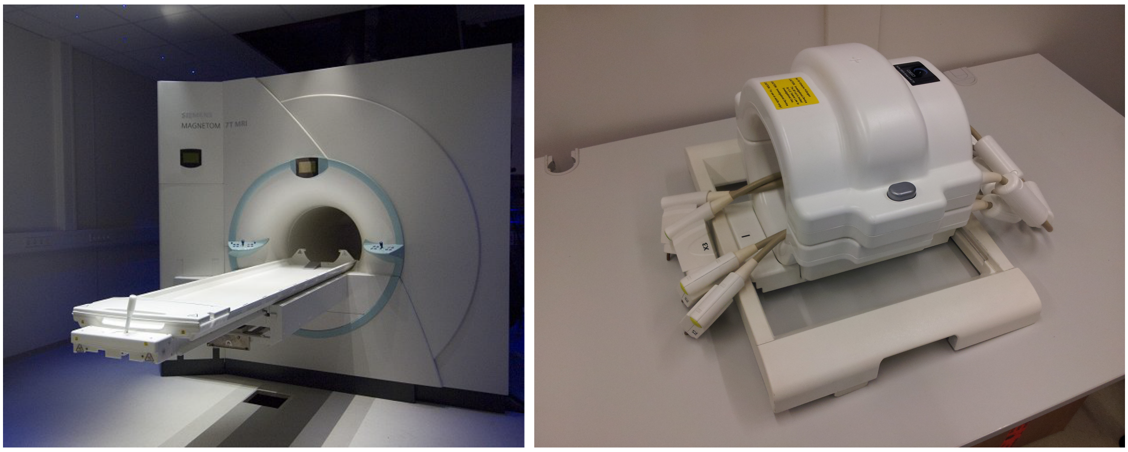

Figure 5.1.: Left: Whole body MR tomograph with $B_0 = 7\,\mathrm{T}$ (MAGNETOM 7T, Siemens Healthineers, Erlangen, Germany) of the German Cancer Research Center (DKFZ) in Heidelberg. Image taken from [98]. Right: 28-channel knee coil (Quality Electrodynamics, Mayfield, OH, USA) for the 7T tomograph.

5.2.2. 14.1 T NMR spectrometer

The Avance II NMR spectrometer from Bruker (Bruker, Karlsruhe-Rheinstetten, Germany) has a basic magnetic field strength of $B_0 \approx 14.1\,\mathrm{T}$. The actual ^{1}H resonance frequency of the systems is $\nu_0 = 600.13\,\mathrm{MHz}$. A combined transmit / receive coil was used for RF irradiation and signal acquisition in the conducted in vitro experiments. The temperature of the investigated sample was controlled using the internal heating and cooling device of the spectrometer.

Figure 5.2.: Bruker AVANCE II NMR spectrometer of the German Cancer Research Center (DKFZ) in Heidelberg. Image reproduced with kind permission from [99]

5.3. Acquisition of MR data

In this part, the individual steps for the acquisition the MR data are described. In this context, the used NMR pulse sequences are introduced and the respective measurement parameters are defined.

5.3.1. CEST sequence

As already mentioned in section 3.2 the CEST-MRI sequence consists of a frequency selective saturation block and an imaging block. These two parts are repeated for each frequency offset. The basic saturation types and the simple gradient-echo imaging sequence are described in the following.

5.3.1.1. Saturation

The cw saturation uses a single rectangular pulse with a length of up to several seconds. Hence cw saturation has a well predefined B_1, a small bandwidth and an efficient saturation, which are all beneficial for a CEST experiment. However, due to technical and safety restrictions only a pulsed saturation can be performed on whole-body MR tomographs. The simplest way to implement such a pulsed saturation is to split the cw-pulse into n rectangular pulses with specified length t_p and delay between two pulses t_d, yet the same amplitude B_1 and frequency offset $\Delta\omega$. To dephase remaining residual magnetization in the x-y-plane several spoiler gradients are activated in the delays t_d and right before the image readout. In case if our standard CEST experiment instead of using a rectangular pulse a Gaussian-shaped pulse given by:

$$B_1(t) = B_1 t_p \frac{1}{\sigma\sqrt{2\pi}} \cdot e^{-\frac{\left(t-\frac{t_p}{2}\right)^2}{2\sigma^2}} - B_1 t_p \cdot b \tag{5.3}$$

was employed. The width-to-pulse duration ratio is $\sigma/t_p = \frac{1}{4.458}$. The pulse is lowered by the baseline $B_1 t_p \cdot b$, with $b = e^{-\frac{t_p^2}{8\sigma^2}}$, to avoid large amplitude steps. In the interval $t = [0\ t_p]$ the pulse is normalized to fulfill:

$$\int B_1(t)\mathrm{d}t = B_1 t_p = \frac{\alpha}{t_p} \tag{5.4}$$

This means, that the stated B_1 amplitude of the shaped pulse is given by the constant B_1 of a rectangular pulse with same length t_p and flip angle α. The different saturation types are illustrated in figure 5.3.

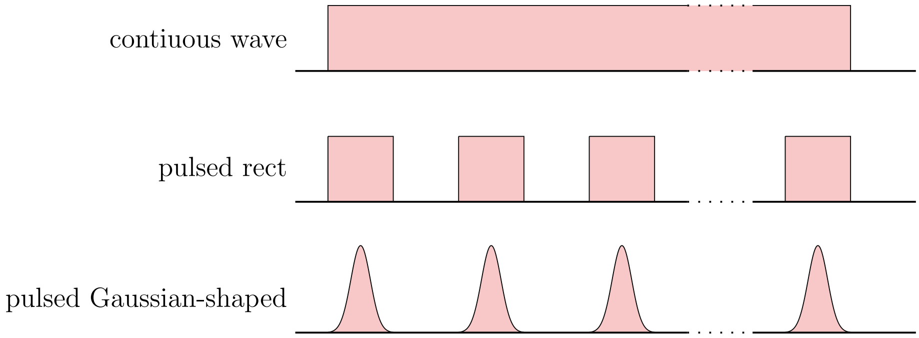

Figure 5.3.: Various saturation schemes. The continuous-wave (cw) saturation is given by a rectangular pulse of duration t_{sat}, amplitude B_1 and the frequency offset $\Delta\omega$. In a clinical setup a pulsed saturation has to be used due to safety limitations. These schemes are additionally defined by the pulse shape, the flip angle and the relation between pulse duration and inter-pulse delay.

In general the Gaussian-shaped pulse can be replaced by any pulse shape of interest, e.g. Sinus-like or Sinc-like functions. The B_1 amplitude is then again given by an equivalent rectangular pulse with same length t_p and flip angle α. Independent of the selected saturation scheme every pulse train is completely defined by the following five parameters:

$$(\ \Delta\omega,\ B_1,\ n,\ t_p,\ DC\ ) \tag{5.5}$$

These parameters allow to derive every other remaining variable:

$$\alpha = \gamma B_1 t_p \tag{5.6}$$

$$t_d = t_p \cdot \left(\frac{1}{DC} - 1\right) \tag{5.7}$$

$$t_{sat} = n \cdot t_p + (n-1) \cdot t_d = (n-1) \cdot \frac{t_p}{DC} + t_p \tag{5.8}$$

5.3.1.2. Readout

The measurement of the modified water signal has to be fast and is carried out immediately after saturation. This was achieved by the use of a gradient-echo (GRE) sequence on the whole-body system. On the NMR spectrometer a short 90°-rect RF pulse (FID) was acquired to record the water signal after preparation. An integration of the water resonance in the range between ±0.7 ppm resulted in the signal $M_{sat}(\Delta\omega)$.

The gradient-echo imaging sequence

A centric reordered spoiled gradient-echo (GRE) sequence was used for subsequent imaging of the modified water signal $M_{sat}(\Delta\omega)$ on the whole-body scanner. The sequence is based on a Siemens (Siemens Healthineers, Erlangen, Germany) product sequence [74]. Figure 5.4 illustrates a simplified sequence scheme. Standard parameters were: $FoV = 150 \times 150$, resolution $1.17 \times 1.17 \times 5\,\text{mm}^3$, $TR = 7.5\,\text{ms}$, $TE = 3.64\,\text{ms}$, flip angle $= 10°$, $bw = 260\,\text{Hz/px}$.

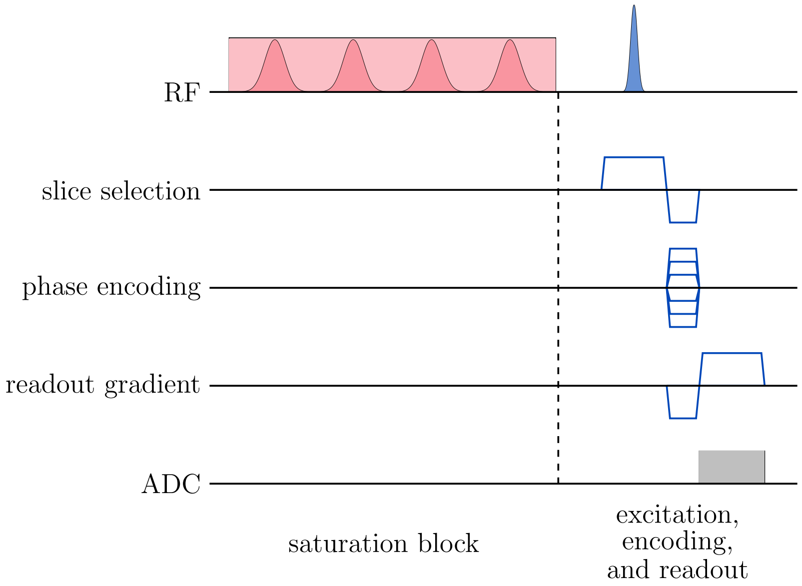

Figure 5.4.: Scheme of the used GRE sequence. The saturated magnetization is excited, spatially encoded and k-space lines are recorded. Crusher gradients after the readout dephase residual magnetization. This is repeated until the full k-space is acquired.

5.3.2. Mapping of the T_1 relaxation time

T_1A mapping was achieved by fitting T_1-weighted images. In the beginning of the thesis a saturation-recovery GRE sequence with 22 recovery times TI between 250 ms and 7.5 s was used. However, a more reliable adiabatic inversion recovery was established within the time frame of this thesis. The on-resonant adiabatic inversion pulse ($\mu = 6$, $bw = 1200\,\text{Hz}$ and $t_p = 8\,\text{ms}$) was performed for 17 recovery times TI between 100 ms and 15 s. The adiabatic approach enabled an evaluation independent of B_1 inhomogeneities [100]. The magnitude images of the MR signal were fitted pixel-wise by the following equation:

$$M(t) = \left|(M(t=0) - M_0) \cdot e^{-t/T_{1A}} + M_0\right| \tag{5.9}$$

For the unlikely case of an imperfect inversion pulse, i.e. $M(t=0) \neq -M_0$, the value $M(t=0)$ was set as a free fit parameter.

Measurement at the spectrometer

The measurement of T_{1A} at the spectrometer was done using a saturation-recovery pulse sequence. A single rectangular on-resonant pulse with duration 15 s saturated the water signal. The integrated water resonances in the range of ±0.7 ppm were fitted for 25 contrasts at different recovery times TI between 10 ms and 20 s to determine the T_{1A} of water. Contrary to the T_{1A} mapping, a simple restricted exponential fit used:

$$M(t) = M_0 \left(1 - e^{-t/T_{1A}}\right) \tag{5.10}$$

5.3.3. Field mapping

To achieve a pixel-by-pixel mapping of the static magnetic field B_0 and RF field B_1 three different methods were used:

internal B_0 map

A spline interpolation of the Z-spectrum was used to determine the intrinsic minimum. This point will be assigned to the frequency offset $\Delta\omega = 0$ ppm and the B_0-deviation can be derived by $\Delta B_0 = \gamma \Delta\omega_0$.

WASSR

The WASSR (***WA****ter* ***S****aturation* ***S****hift* ***R****eferencing*) method [101] uses a weak RF pulse to ensure only the saturation of the water peak. The resulting Z-spectrum does not depend on field inhomogeneities and thus is symmetrical to the point of minimum intensity. This point is also the actual resonance frequency. Determination of the deviation of this frequency to the nominal frequency allows to calculate the B_0 deviation by $\Delta B_0 = \gamma \Delta\omega_0$.

WASABI

The WASABI (***WA****ter* ***S****hift* ***A****nd* ***B1****-mapping*) method [102] enables both B_0- and B_1-mapping simultaneously. A short off-resonant rectangular saturation pulse leads to a Sinc-like spectrum. This spectrum is fitted using the signal equation without relaxation [40]:

$$Z(\Delta\omega) = \left| c - d \cdot sin\left(tan^{-1}\left(\frac{\gamma \cdot B_1}{\Delta\omega - \delta\omega_A} \right)^2 \right) \cdot sin^2\left(\sqrt{(\gamma \cdot B_1)^2 + (\Delta\omega - \delta\omega_A)^2} \cdot \frac{t_p}{2} \right) \right| \tag{5.11}$$

The parameter c and d compensate magnitude changes, and have no influence on the period or frequency shift. Determination of the symmetry axis shift $\delta\omega_A$ allows the calculation of of the B_0-shift using $\delta B_0 = \gamma \cdot \delta\omega_A = 42.577\,\mathrm{MHz\,T^{-1}} \cdot \delta\omega_A$.

5.4. Postprocessing of the CEST data

This part describes the general procedure used in this thesis to handle the acquired CEST data. It covers the different correction and evaluation methods as well as the resulting contrasts.

5.4.1. Normalization

First, the data is normalized with the aid of an M_0 image on a pixel-by-pixel basis using $Z(\Delta\omega) = \frac{M(\Delta\omega)}{M_0}$ (section 3.2). In the case of a repeated measurement of M_0 images during the CEST acquisition - e.g. before and after the regular offsets - these images were interpolated linearly over the frequency offset index and allowed a normalization by: $Z(\Delta\omega) = \frac{M(\Delta\omega)}{M_0(\Delta\omega)}$.

5.4.2. B_0-correction algorithm

As already described in chapter 3.4 the static magnetic field B_0 has an influence on the resulting Z-spectra. Since there are still inhomogeneities in B_0, even after shimming the desired field of view (FoV), a further correction is necessary. By creating so-called ΔB_0 maps (section 5.3.3), the still existing influence on the inhomogeneities can be eliminated or at least minimized. The general pixel-by-pixel B_0-correction procedure is:

- interpolation of the acquired Z-spectrum to 0.01 ppm accuracy
- rounding of the B_0-shift to 0.01 ppm accuracy
- shift of the Z-spectrum by ΔB_0
- linear extrapolation of the now missing values at the edge of the Z-spectrum
- back transformation to the original accuracy

The extrapolation at the edge of the Z-spectrum can be critical for measurements which only acquires offsets near the water resonance, since it generates data points which most certainly do not reflect the reality. This is negligible if the sampling scheme has points far away from any resonance of interest ($|\Delta\omega| \geq 25\,\text{ppm}$), because all effects important for the description of the chemical exchange resonate close to water. At this time point the WASABI sequence is the method of choice, however it was only developed within the time frame of this thesis. The B_0-correction in the first phantom experiments were conducted using WASSR. For all in vivo measurements the correction was done with the help of the WASABI sequence.

5.4.3. Z_{lab} and Z_{ref} - the label and reference value

The isolation of CEST effects is done with the help of the so-called reference value Z_{ref} (section 4.5), which is free of influences of confounding effects like direct water saturation or semi-solid MT. The simulated or measured data points in the Z-spectrum correspond to the value Z_{lab}. Since the reference value at the resonance frequency of interest can not be measured directly, two methods are introduced to obtain Z_{ref}.

Asymmetry approach

The common and easiest way to determine Z_{ref} is the asymmetry approach [12]. Under the assumption of no confounding effect downfield from water the Z-value on the opposite side of the Z-spectrum can be used as the reference value:

$$Z_{ref} = Z_{lab}(-\Delta\omega) \tag{5.12}$$

Multiple Lorentzian fitting

Every contribution in the Z-spectrum can be described by a single Lorentzian-like function (section 4.4). The in vivo Z-spectra of the human calf are fitted by a superposition of up to six Lorentzian functions $\mathcal{L}$. The different pools represent the direct water saturation (water), semi-solid MT (ssMT), aliphatic rNOE and effects due to the chemical exchange of amides, amines and guanidinium groups of creatine. Due to possible imperfect recovery to the equilibrium the maximum value of the Z-spectrum is additionally fitted by Z_{max}:

$$Z_{lab} = Z_{max} - (\mathcal{L}_{water} + \mathcal{L}_{ssMT} + \mathcal{L}_{amide} + \mathcal{L}_{aliphatic} + \mathcal{L}_{amine} + \mathcal{L}_{guanidine}) \tag{5.13}$$

Pool	Amplitude A	FWHM Γ [ppm]	frequency offset δ [ppm]
water	0.9	1.4	0
ssMT	0.1	25	-1
Amide	0.05	0.5	3.5
rNOE	0.02	3	-3.5
guanidine	0.05	1.5	1.9
Amine	0.05	1.5	2.7

Table 5.2.: Start parameters of the 6-pool Lorentzian fit model used to analyze Z-spectra obtained from measurements of the human calf.

The reference value can then be calculated by adding up the Lorentzians of the direct water saturation and ssMT:

$$Z_{ref} = Z_{max} - (\mathcal{L}_{water} + \mathcal{L}_{ssMT}) \tag{5.14}$$

The start parameters for the 6-pool Lorentzian fit for modeling of the human calf are listed in table 5.2.

5.4.4. B_1-correction

As already noted in section 3.4 the CEST effect depends strongly on the B_1 amplitude and maximizes for a specific B_1. Therefore B_1-inhomogeneities across the volume lead to an alteration of the CEST contrast, even though voxel of the same tissue type should maintain an equal contrast. The B_1-inhomogeneities are mainly due to the resulting shorter RF-wavelengths at ultra-high fields ($B_0 \geq 3\,\mathrm{T}$).
To compensate for these inhomogeneities the correction method by *Windschuh et al.* [103] was employed. The acquisition of Z-spectra of at least two different B_1 amplitudes ($B_{1,1}$, $B_{1,2}$) and an additional B_1-map enables an interpolation approach (figure 5.5) to reconstruct a Z-spectrum or contrast at a specific $B_{1,interest}$ with $B_{1,1} \leq B_{1,interest} \leq B_{1,2}$.

5.4.5. Contrast metric

With the help of B_0- and B_1-corrected data sets the inverse metric can be used to obtain also spillover- and relaxation-compensated CEST effects. For this calculation the acquired T_{1A}-map was used. The contrast was calculated as follows:

$$AREX = \left(\frac{1}{Z_{lab}} - \frac{1}{Z_{ref}}\right) \cdot \frac{1}{T_{1A}} \tag{5.15}$$

5.5. Phantoms

In all in vitro experiments, model solutions of creatine monohydrate (Sigma-Aldrich, Steinheim, Germany) with different concentrations, pH values and relaxation parameters were investigated. The resonance of the guanidinium group $(-\mathrm{NH}_2)^2$ of creatine is located at $\Delta\omega \sim 1.9\,\mathrm{ppm}$ in the Z-spectrum [60]. The solutions were buffered using phosphate-buffered saline with 1/15 M sodium potassium phosphate and held at the temperature $T = (37 \pm 2)°\mathrm{C}$.

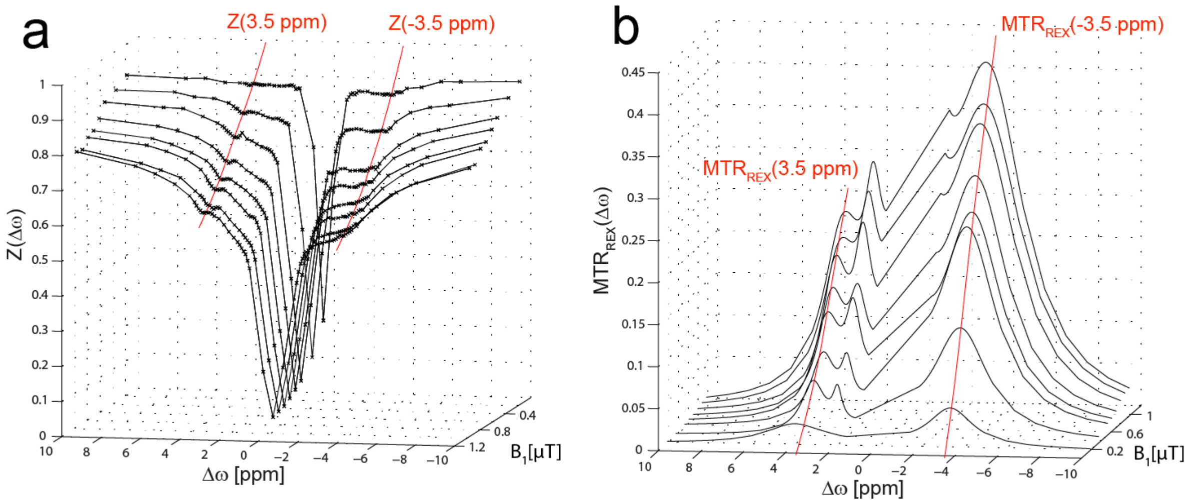

Figure 5.5.: The B_1-correction method of *Windschuh et al.* [103] is depicted. Z-spectra (a) and $\mathrm{MTR_{Rex}}$-spectra (b) in a ROI of GM of the brain of a healthy volunteer for different B_1 are shown. The red curves represent the fitted smoothing splines used for B_1-correction at the according frequency offsets. Reprinted with kind permission from [70].

5.5.1. Creatine model solutions for the spectrometer

Phantom #S1

For the first experiment regarding Ω-plot analysis a 3 ml model solution with creatine concentration $c_{Cr} = 50\,\mathrm{mM}$ and $pH7.12$ was created. This phantom is called #S1.

Phantom #S2

The study of different pulse shapes was performed using a 3 ml model solution with creatine concentration $c_{Cr} = 50\,\mathrm{mM}$ and $pH7.15$. This phantom is called #S2.

5.5.2. Creatine phantom for 7T

For MR measurements at $B_0 = 7\,\mathrm{T}$, three sets of phantoms were employed, each containing seven 30 mL tubes (table 5.3). Phantom #1 consisted of varying creatine concentrations c_{Cr}, while for phantom #2 the pH was varied and, finally, for phantom #3 the longitudinal relaxation times of water T_{1A} and transversal relaxation times of water T_{2A} were varied, induced by gadolinium ($Gd - DTPA$; Magnevist, Bayer Schering Pharma, Berlin, Germany) doping and changing the *agar* concentration, respectively.

The longitudinal relaxation times T_{1A} for phantoms #1 and #2 as well as for tubes 1-4 in phantom #3 were measured to be (4.31 ± 0.13) s. The T_{1A} values of the remaining tubes in phantom #3 were (0.95 ± 0.05) s, (0.69 ± 0.04) s, and (0.45 ± 0.09) s in the tubes 5, 6 and 7, respectively. The transversal relaxation times T_{2A} were not measured, however, for the chosen agar concentrations they should be in the range of 1.6 s (0% agar) and 0.13 s (1% agar) according to Zaiss et al. [27].

Phantom			1	2	3	4	5	6	7
#1	(pH 7.15)	c_{Cr} [mM]	10	20	35	50	75	100	125
#2	($c_{Cr} = 50\,\text{mM}$)	pH	6.32	6.54	6.74	6.94	7.15	7.40	7.60
#3	(pH 7.15, $c_{Cr} = 50\,\text{mM}$)	$Gd\text{-}DTPA$ [μM]	0	0	0	0	125	250	500
		Agar [%]	0.5	0.5	1	2	0.5	0.5	0.5

Table 5.3.: Composition of the three phantoms for the experiments conducted at $B_0 = 7\,\text{T}$. Phantom #1 contains varying creatine concentrations c_{Cr}, phantom #2 contains solutions of varying pH, while phantom #3 contains varying gadolinium and/or *agar* concentrations.

5.6. In vivo application in healthy volunteers

The right calf of four male and healthy volunteers (23-29 years old) were examined. The average measurement time for each volunteer was about 65 min and consisted of positioning and shimming of the FoV, 5 CEST measurements using Gaussian-shaped saturation pulses with different saturation amplitudes B_1, the acquisition of ΔB_0 and relative B_1 by the means of WASABI and measurement of T_1.

MR-compatible foot pedal

To investigate studies regarding muscle exercise within the whole-body scanner a mechanical, non-magnetic foot pedal was used (figure 5.6). This pedal was drafted and manufactured in cooperation with the mechanical workshop of the DKFZ. Plantar and dorsi flexion will be carried out using this pedal. The foot is fixated with a velcro fastener in the toe area. A rubber band yielded the restoring force. The horizontal and vertical location of the pedal can be changed to optimize the positioning of the lower leg within the RF coil.

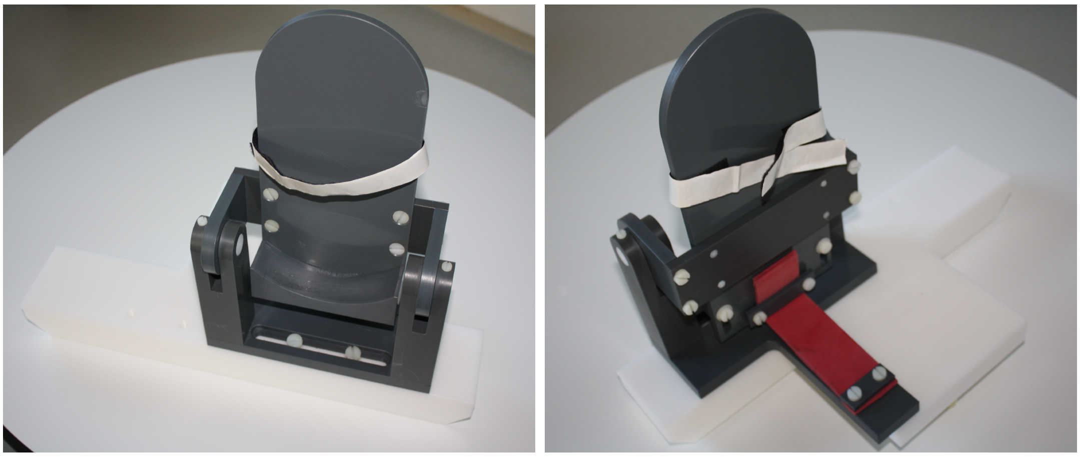

Figure 5.6.: The MR-compatible foot pedal in front (left) and back view (right). A velcro fastener (white band) is used to fixate the foot and a rubber band yields the restoring force. Constructed by the mechanical workshop of the German Cancer Research Center (DKFZ).

6. Results

To investigate the quantitative behavior of CEST agents in a first step a new analytical model is introduced. It is shown, that the inclusion of two form factors is sufficient to describe the exchange-dependent relaxation rate R_{ex} in the case of saturation with Gaussian-shaped pulses (section 6.1). This analytical model can be used to extend the existing Ω-plot method for the case of pulsed saturation (section 6.2). This allowed to characterize the exchange of the guanidinium group of creatine in a quantitative manner for the a saturation using Gaussian-shaped pulses. Validity and functionality of the presented theory was verified mathematically and experimentally for several saturation schemes, e.g. sinusoidal or sinc-like pulses. The correct description of the complex situation in vivo for the chemical exchange was then explored by multiple Lorentzian fitting (section 6.3). Finally, all the insight gained in this study enabled a quantitative experiment in vivo allowing the determination of the pH value in the human calf (section 6.4).

6.1. Analytical description of the pulsed CEST experiment

Parts of this section are published in the Journal *NMR in Biomedicine* [104].

In contrast to continuous-wave (cw) saturation, the longitudinal relaxation rate in the rotating frame $R_{1\rho}$ of shaped pulses is time-dependent in $\omega_1(t)$:

$$R_{1\rho}(\omega_1(t)) = R_{eff}(\omega_1(t)) + R_{ex}(\omega_1(t)). \tag{6.1}$$

The average $\overline{R_{1\rho}}$ in the case of saturation by means of shaped pulses is calculated by integration of $R_{1\rho}$, given by inserting equations (4.17) and (4.25) into equation (4.15), as a function of the pulse duration t_p:

$$\begin{aligned}
\overline{R_{1\rho}} &= \frac{1}{t_p}\int_0^{t_p} R_{1\rho}\mathrm{d}t && (6.2)\\
&= \frac{1}{t_p}\int_0^{t_p} (R_{eff}(t) + R_{ex}(t))\mathrm{d}t && (6.3)\\
&= R_{1A} + \frac{1}{t_p}\int_0^{t_p} (R_{2A} - R_{1A})\,\frac{\omega_1^2(t)}{\omega_1^2(t) + \Delta\omega^2}\mathrm{d}t \\
&\quad + \frac{1}{t_p}\int_0^{t_p} f_B k_{BA}\frac{\omega_1^2(t)}{\omega_1^2(t) + k_{BA}\left(k_{BA} + R_{2B}\right) + \frac{k_{BA}}{k_{BA}+R_{2B}}\Delta\omega_B^2}\mathrm{d}t && (6.4)
\end{aligned}$$

This equation can be solved numerically, however, in the following section an analytical solution is derived for the case of Gaussian-shaped saturation pulses.

6.1.1. $\overline{R_{1\rho}}$ for a Gaussian-shaped pulse

For Gaussian-shaped pulses it can be shown that the characteristic relaxation rate in the rotating frame $R_{1\rho}$ can be described on average by a time-independent ω_1 and the form factors c_1 and c_2 [104] (Appendix D) with

$$\begin{aligned} R_{1\rho}^{Gaussian} &\approx R_{1A} + (R_{2A} - R_{1A}) \cdot c_1 \cdot \frac{\omega_1^2}{\omega_1^2 + \Delta\omega^2 \cdot c_2^2} \\ &+ f_B k_{BA} \cdot c_1 \cdot \frac{\omega_1^2}{\omega_1^2 + \left(k_{BA}\left(k_{BA} + R_{2B}\right) + \frac{k_{BA}}{k_{BA}+R_{2B}} \Delta\omega_B^2\right) \cdot c_2^2} \end{aligned} \tag{6.5}$$

where c_1 and c_2 depend only on the width σ and length t_p of one Gaussian-shaped pulse. They are defined as

$$c_1 = \frac{\sigma\sqrt{2\pi}}{t_p} \tag{6.6}$$

$$c_2 = c_1 \cdot \sqrt{\sqrt{2}} = \frac{\sigma\sqrt{2\pi}}{t_p} \cdot \sqrt{\sqrt{2}} \tag{6.7}$$

Thus, AREX in the case of a saturation using Gaussian-shaped pulses is modified compared with an experiment using cw irradiation (equation (4.38)) to:

$$AREX_{Gaussian} = DC \cdot f_B k_{BA} \cdot c_1 \frac{\omega_1^2}{\omega_1^2 + \left(k_{BA}\left(k_{BA} + R_{2B}\right) + \frac{k_{BA}}{k_{BA}+R_{2B}} \Delta\omega_B^2\right) \cdot c_2^2} \tag{6.8}$$

The accuracy of the analytical solution is verified by numerical simulations (section 5.1). Figure 6.1 shows Z-spectra generated using a 2-pool Bloch-McConnell simulation (dots) and the analytical solution (lines), respectively. The analytical Z-value is determined by inserting equation (6.5) into equation (4.43). The four main dependencies of the CEST effect (equation (4.25) and (6.8)), the saturation amplitude B_1, the exchange rate k_{BA}, the relative concentration f_B and the transversal relaxation rate R_{2B}, were analyzed over a broad range of values. The used Gaussian-shaped pulse has a width-to-length ratio of $\sigma/t_p = 1/4.458$ resulting in the form factors $c_1 = 0.5672$ and $c_2 = 0.6687$.
Off-resonant ($\Delta\omega \sim -5$ ppm) both simulations agree with each other. Close to the water resonance and on-resonant on the pool B ($\Delta\omega_B$) the analytical solution underestimates the Z-value. This deviations increase for higher saturation amplitudes B_1 (figure 6.1A). For very high saturation strengths even the far off-resonant analytical value deviates. Changing the exchange rate k_{BA} does not affect the deviation between analytical and numerical solution significantly (figure 6.1B). A higher relative concentration f_B of pool B results in an increase of deviation (figure 6.1C). Like the exchange rate, a higher transversal relaxation rate R_{2B} of pool B yields no significant change in the deviation (figure 6.1D).

To describe the CEST effect the on-resonant value is of particular importance. To verify the analytical model the apparent exchange-dependent relaxation rate AREX was calculated at the resonance frequency of pool B (i.e. $\Delta\omega_B = 1.9\,\text{ppm}$) for both simulations. An even broader range of parameters compared to figure 6.1 is depicted in figure 6.2. In addition to the numerical simulation (black dots) and analytical solution from equation (6.8) the analytical solution without the form factors (equation (4.44) or (6.8) with $c_1 = c_2 = 1, DC = 50\%$, respectively) is shown (red line). The numerical simulation depicts the universally valid dependencies of the CEST for the used range of parameters:

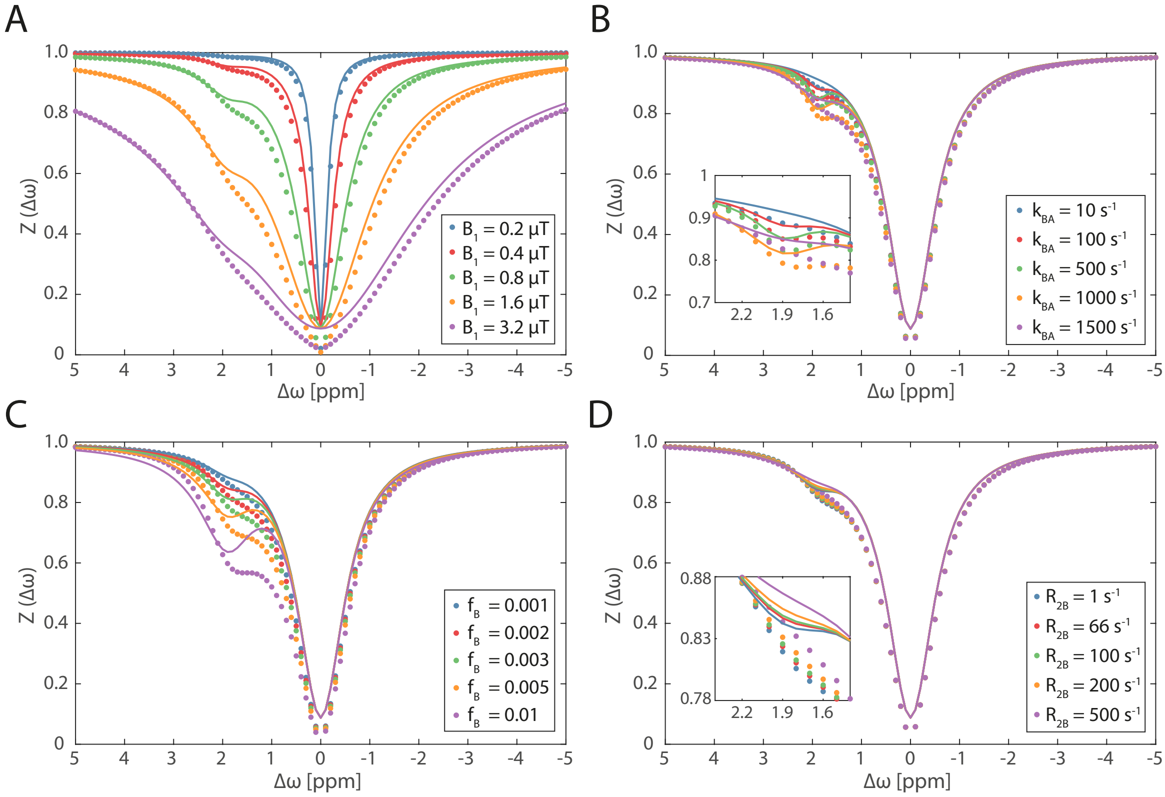

Figure 6.1.: Analytical (lines) and numerical (dots) simulation of Z-spectra using saturation by trains of Gaussian-shaped RF pulses ($B_1 = 0.8\,\mu$T, $n = 100$, $t_p = 0.1\,$s, $DC = 50\%$, $\sigma/t_p = 1/4.458$) with various B_1 (A), k_{BA} (B), f_B (C) and R_{2B} (D). The creatine guanidinium proton pool, which resonates at 1.9 ppm, was simulated using $k_{BA} = 945\,\mathrm{s}^{-1}$, $f_B = 2.00‰$ and $R_{2B} = 66\,\mathrm{s}^{-1}$. Water relaxation times were set to $T_1 = 1.9\,$s and $T_2 = 0.05\,$s.

- (A) AREX increases with increasing saturation amplitude B_1, while the transition into a steady-state for very high B_1 is visible
- (B) the presence of an optimal value for the exchange rate k_{BA} recognizable by the Lorentzian-like peak in AREX
- (C) a linear dependency of the relative concentration f_B and AREX
- (D) a rapid decrease of AREX for transversal relaxation rates $R_{2B} \geq 200\,\mathrm{s}^{-1}$

These trends are in general reproduced by the analytical simulations, however some important differences towards the numerical simulation and between both analytical solutions are present. Even though both analytical simulations underestimate AREX for low saturation amplitudes B_1, the solution without form factors intersects the numerical simulation at a specific B_1 and overestimates AREX from there on (A). The solution with form factors on the other hand describes the actual trend of AREX very well, except from a deviation increasing linearly as a function of B_1.

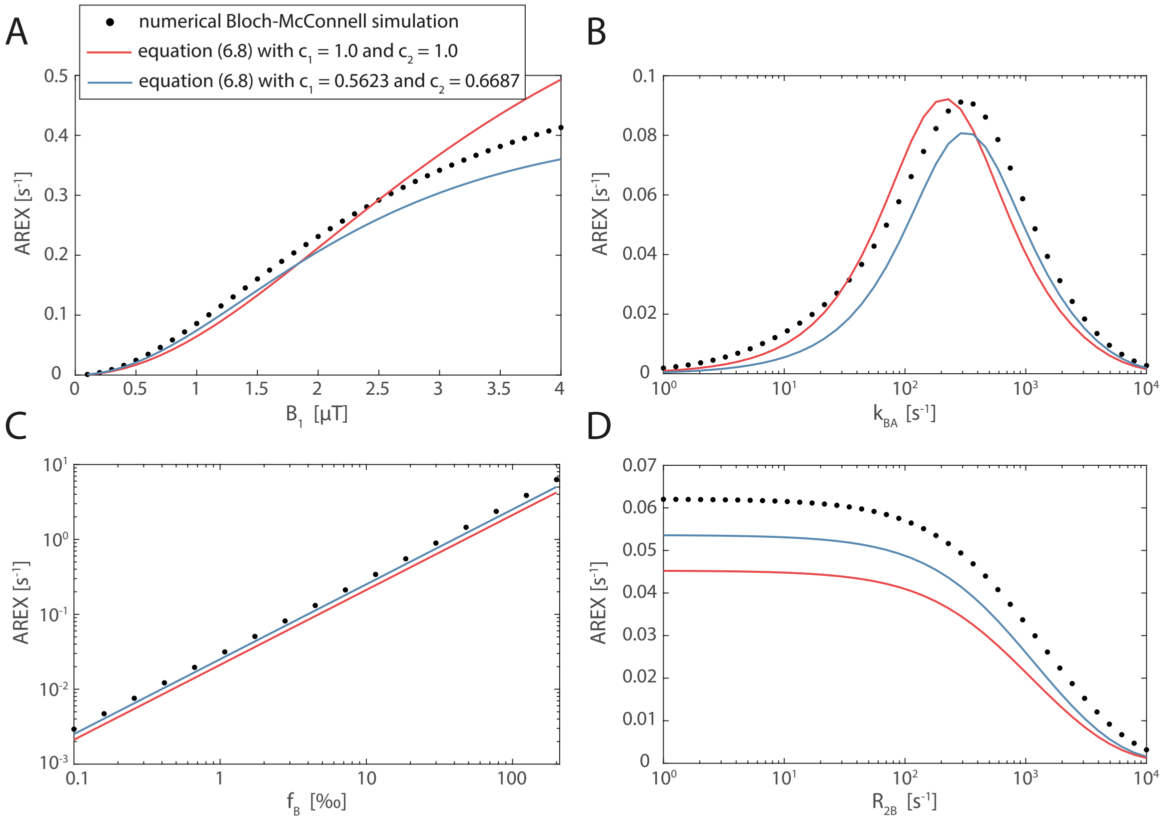

Figure 6.2.: Analytical and numerical simulation (black dots) of AREX for different B_1, k_{BA}, f_B and R_{2B}. The analytical solution with form factors $c_1 = 0.5623$ and $c_2 = 0.6687$ and duty cycle DC is shown as well (blue line) as the solution assuming a rectangular saturation pulse, i.e. $c_1 = c_2 = 1$ (red line). The simulation parameter for pool A and B are equal to the ones used in figure 6.1.

Both analytical solutions depict a maximum in AREX depending on the exchange rate k_{BA}, however, the actual position of k_{BA} or maximal value $AREX_{max}$ are changed (B). While the solution without form factors reproduces the AREX value pretty well, the maximum of the Lorentzian-shaped curve is shifted to lower exchange rates. This shift is corrected using the form factors, but the AREX values are thereby slightly underestimated.
The linear dependency of AREX from the relative concentration f_B is given for both analytical solutions, while the solution including the form factors exhibits a decreased deviation (C). The same result, i.e. a better estimation with the form factors, can be observed for the transversal relaxation rate R_{2B} (D). All in all the behavior of AREX is better described by the analytical solution with form factors than without.

It is worth noting that the analytical simulation using equation (6.8) was approximately 250.000-times faster than the numerical simulation.

6.2. Quantitative pulsed CEST

Parts of this section are published in the Journal *NMR in Biomedicine* [104].

This part in divided into three parts. First, the analytical solution of the previous section is used to extend *Dixon's Ω-plot method* [34] in the case of saturation by the means of shaped pulses. The approach is theoretically validated using BM-simulation and tested by conducting experiments on the whole-body scanner. In the second part a new experimental way to determine the form factors is presented. This is used in third part to investigate saturation performed by other pulse shapes.

6.2.1. Extended Ω-plot method

As described in section 4.6 and 4.7 the Ω-plot method enables the simultaneously determination of exchange rate k_{BA} and relative concentration f_B. However, performing the saturation with shaped pulses would lead to different Z-spectra compared to cw saturation (figure 6.3A). Even though the nominal B_1 amplitude (equation (5.3)) remains the same, the cw saturation generates larger CEST effects and a broader direct water saturation. The resulting Ω-plots reveals for both the desired linearity, but different slopes m and y-intersections n (figure 6.3B). Hence equations (4.45) and (4.46) would yield a wrong estimation of k_{BA} and f_B.
The analytical solution for saturation with Gaussian-shaped pulses, which was derived in the previous section, can be used to extend the Ω-plot method. Inversion of equation (6.8) yields the following formulas for the exchange rate k_{BA} and relative concentration f_B in the case of on-resonant saturation by Gaussian-shaped pulses:

$$k_{BA} = \left(-\frac{R_{2B}}{2} + \sqrt{\frac{R_{2B}^2}{4} + \frac{m}{n \cdot c_2^2}}\right) \tag{6.9}$$

$$f_B = \frac{1}{DC \cdot n \cdot c_1 \cdot \left(-\frac{R_{2B}}{2} + \sqrt{\frac{R_{2B}^2}{4} + \frac{m}{n \cdot c_2^2}}\right)} \tag{6.10}$$

where c_1 and c_2 are again the form factors introduced in section 6.1.1. These equations allow now the comparison of the Ω-plot method for a pulsed and a cw saturation. For this experiment phantom #S1 with pH 7.12, creatine concentration $c_{Cr} = 50\,\mathrm{mM}$ and $T_{1A} = (3.62 \pm 0.24)\,\mathrm{s}$ was examined at $B_0 = 14.1\,\mathrm{T}$ (section 5.5.1). Ω-plot evaluation (figure 6.3B) of the cw CEST experiment (straight line) using equations (4.45) and (4.46) and the pulsed CEST experiment (figure 6.3B, dotted line) using equations (6.9) and (6.10) yield the tupel

$$\begin{aligned}\left(k_{BA}\left[\mathrm{s}^{-1}\right]|f_B\,[‰]\right)_{cw} &= (911 \pm 123 | 1.72 \pm 0.34)\\ \left(k_{BA}\left[\mathrm{s}^{-1}\right]|f_B\,[‰]\right)_{Gaussian} &\approx (838 \pm 324 | 1.88 \pm 0.16)\end{aligned}$$

respectively. The values of the extended Ω-plot method agree, within the errors limits, with the values obtained by the cw saturation. Without the correction for Gaussian-shaped pulses, i.e. equations (6.10) and (6.9) with $c_1 = c_2 = 1$ and $DC = 50\%$, a more biased estimation is generated $\left(k_{BA}\left[\mathrm{s}^{-1}\right]|f_B\,[‰]\right) \approx (550 \pm 218 | 1.62 \pm 0.13)$. The application of the cw solution directly to the measurement using shaped pulses results in $\left(k_{BA}\left[\mathrm{s}^{-1}\right]|f_B\,[‰]\right) \approx (550 \pm 218 | 0.81 \pm 0.13)$.

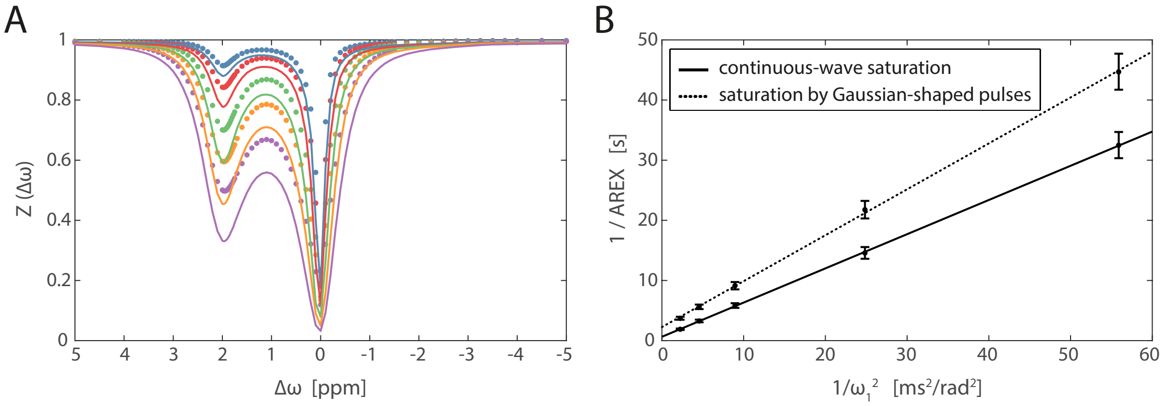

Figure 6.3.: Comparison of the Ω-plot method for cw and pulsed saturation. Experimental Z-spectra for cw saturation (lines) and saturation using Gaussian-shaped pulses (dots) with various B_1 values obtained from model solution measurements of phantom #S1 ($c_{Cr} = 50\,\text{mM}$, pH 7.12, $T = 37°\text{C}$) at $B_0 = 14.1\,\text{T}$ (A). The saturation time was $t_{sat} = 14.1\,\text{s}$ for cw, whereas for the pulsed saturation 71 Gaussian-shaped pulses with $t_p = 0.1\,\text{s}$ and $DC = 50\%$ were used. For the same saturation amplitudes, the cw measurement shows a larger CEST effect compared with the pulsed pre-saturation. The corresponding Ω-plots display the expected linearity (B). The calculated form factors for the Gaussian-shaped pulses are $c_1 = \sigma / t_p \cdot \sqrt{2\pi} = 0.5623$ and $c_2 = c_1 \sqrt[4]{2} = 0.6687$. The original image is from [104].

6.2.1.1. Accuracy of the extended Ω-plot method

To further assess the extended Ω-plot method the accuracy was tested using numerical Bloch-McConnell simulations (section 5.1). The exchange parameters of pool B, the exchange rate k_{BA} and relative concentration f_B, as well as the water relaxation parameter, the longitudinal and transversal relaxation times T_{1A} and T_{2A}, were varied over a broad range. If the parameters were not changed they were held to the values given in table 5.1. The values determined with equations (6.9) and (6.10) were normalized by the simulated parameter (figure 6.4). The colorbar, which applies for all four subplots, was adjusted to point out deviations of more than 15%. It is observable that the proposed Ω-plot method works well for $150\,\text{s}^{-1} \leq k_{BA} \leq 2000\,\text{s}^{-1}$ and $0.07\% \leq f_B \leq 1\%$ (figure 6.4 A and C). The extreme discrepancies for $< 50\,\text{s}^{-1}$ are expected due to the inadequate modeling of the inter-pause delay in the case of very slow exchange rates [27]. In the case of variations in relaxation times only the combination of high T_{1A} and low T_{2A} results in deviation larger than 15%. In addition, there are overall minor influences of the water relaxation parameter, especially the longitudinal relaxation time T_{1A}. These inaccuracies might originate from violations of the steady-state condition.

All in all, the extended Ω-plot method yields estimations close to the simulated parameter in the whole intermediate exchange regime. Therefore the analytical model proposed in section 6.1.1 is suitable to determine the exchange k_{BA} and relative concentration f_B in the case of saturation by Gaussian-shaped pulses.

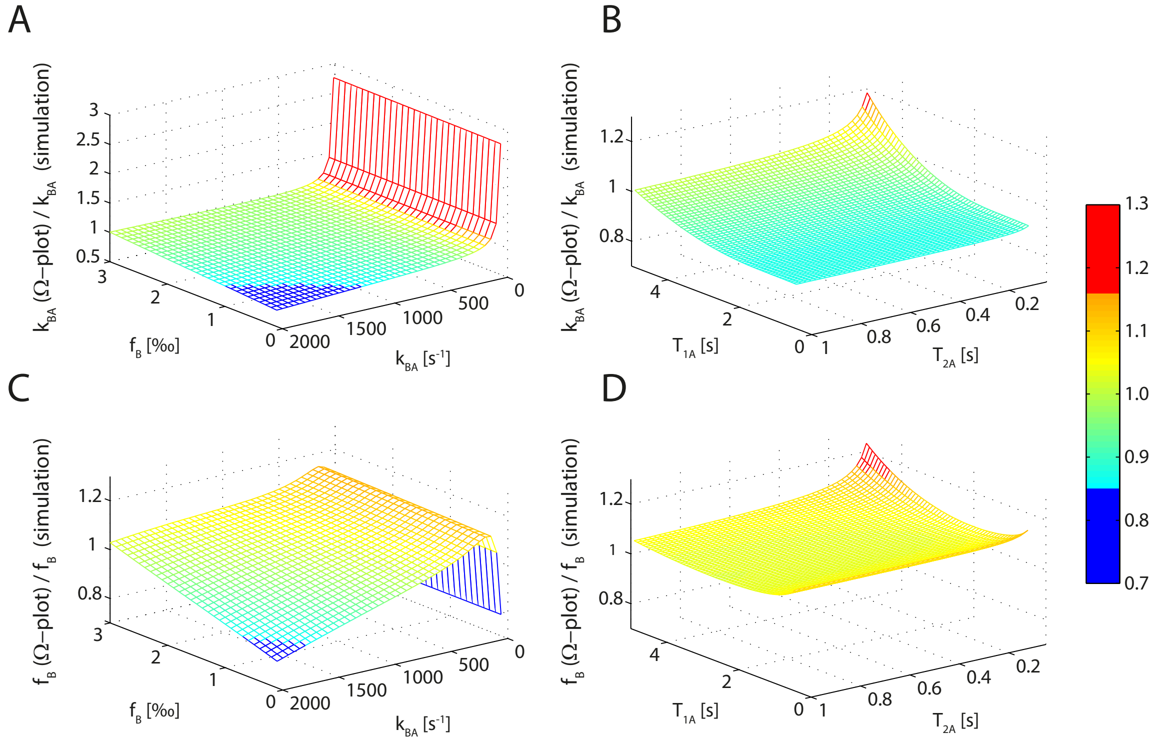

Figure 6.4.: The accuracy of the CEST analysis using the extended Ω-plot method for simulations is depicted. The normalized exchange rate is displayed as a function of exchange rate k_{BA} and relative concentration f_B (A) and as a function of relaxation times T_{1A} and T_{2A} of the water pool (B). The normalized relative concentration is also shown as a function of k_{BA} and f_B (C) and as a function of relaxation times T_{1A} and T_{2A} of the water pool (D). The color bar applies to all graphs. Saturation was always carried out using 60 Gaussian-shaped pulses ($t_p = 0.1\,\text{s}$, $DC = 50\%$, $\sigma/t_p = 1/4.458$). The original image is from [104].

6.2.1.2. Investigation of different creatine model solutions

An expanded experimental investigation of the proposed Ω-plot method was done by measuring the three phantoms introduced in section 5.5.2. They contained varying creatine concentrations c_{Cr} (phantom #1), varying pH values (phantom #2), and varying water relaxation times T_{1A} and T_{2A} (phantom #3), while the other two parameters were held constant. A region-of-interest (ROI) analysis was performed in each tube to obtain averaged AREX values at the resonance frequency $\Delta\omega_B = 1.9\,\text{ppm}$. The correlations between 1/AREX and $1/\omega_1^2$ are shown in figure 6.5. The numbering of each tube in the three phantoms refers to table 5.3. All Ω-plots depict the desired linearity. This fact reaffirms that the principle formula for R_{ex} – especially the B_1 dispersion – must have the same form for pulsed as for cw saturation. Noticeable is, that the Ω-plots of phantom #1 and #2, i.e. varying creatine concentration c_{Cr} and pH values, show different slopes m and displacements in y-direction n, while the tubes of phantom #3 with constant c_{Cr} and pH yield, within the error limits, equivalent Ω-plots.

Thus, equations (6.9) and (6.10) can be used for evaluation of pixel-wise calculated Ω-plots. The application to the phantom imaging data enabled the reconstruction of quantitative maps

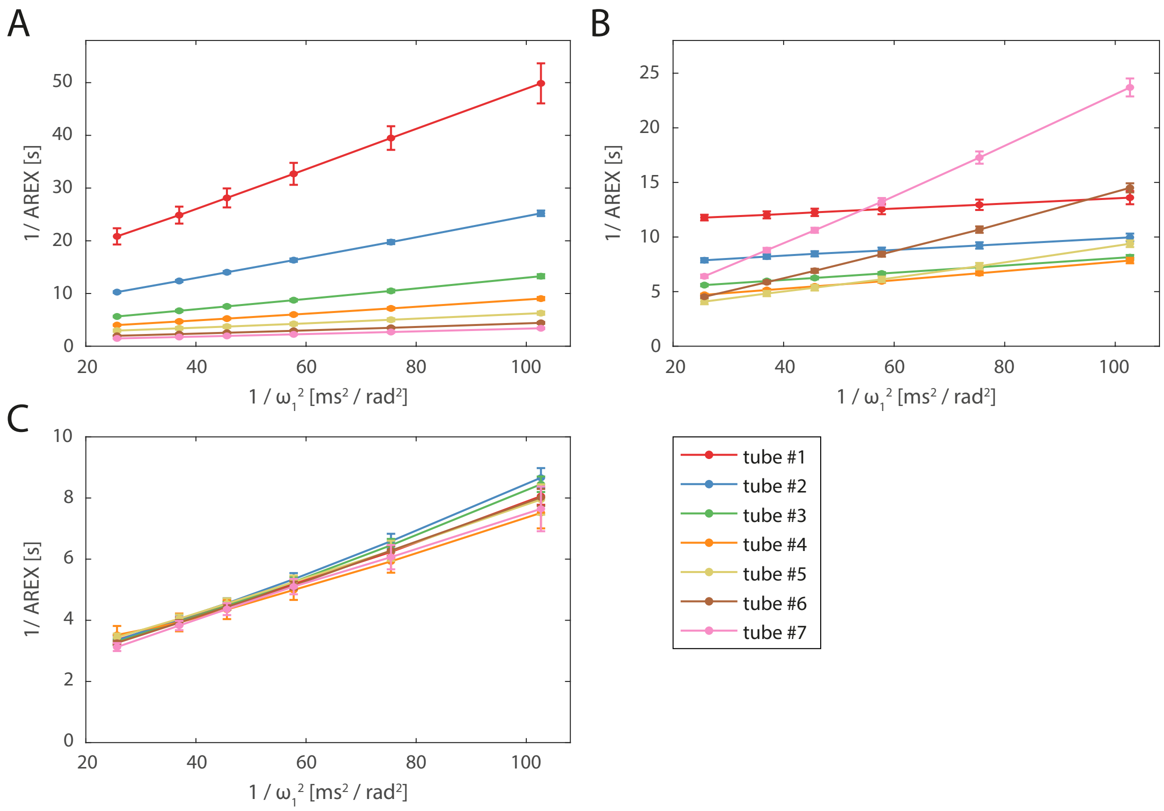

Figure 6.5.: Ω-plots determined from ROI analysis of the three phantoms (table 5.3). All pixels within each tube were selected and averaged. The linearity is given for the entire range of the creatine concentrations (A), pH values (B), and water relaxation parameters (C). Whereas the Ω-plots in phantom #1 (A) and phantom #2 (B) show a different behavior for each tube, the different relaxation parameters in phantom #3 (C) yield the same Ω-plots within the error limits. The original image is from [104].

within minutes (figure 6.6). For illustration purposes all pixels with no significant CEST effect, i.e. $Z(\Delta\omega = -1.9\,\text{ppm}) - Z(\Delta\omega = +1.9\,\text{ppm}) < 0.04$, were set to zero. This is justifiable since an effect can be expected in all meaningful pixels. While the k_{BA}-map for varying creatine concentrations (phantom #1) is homogenous across the tubes, the f_B-map shows the correct trend with c_{Cr} (figure 6.6A, B). For the phantom with varying pH values these correlations are reversed, meaning a correlation with k_{BA} and homogenous f_B-maps. The ring-like structure and artifacts, especially in tube #1 and #7, result from an incomplete B_1-correction. The tubes in phantom #3, with constant c_{Cr} and pH but changing water relaxation times T_{1A} and T_{2A}, show only very small variations between each other in both the k_{BA}- and f_B-maps.

The correct qualitative behavior of the analytical solution and consequently the extended Ω-plot method have been verified. The next step was the investigation of full quantitative values of exchange rate k_{BA} and relative concentration f_B. The region-of-interest analysis in each tube is shown in figure 6.7. All pixels within each tube were selected and averaged. The results from the extended Ω-plot method (i.e. equations (6.10) and (6.9)) are shown (blue) as well as the results obtained for equations (4.41) and (4.40) (red). The exchange rate k_{BA}

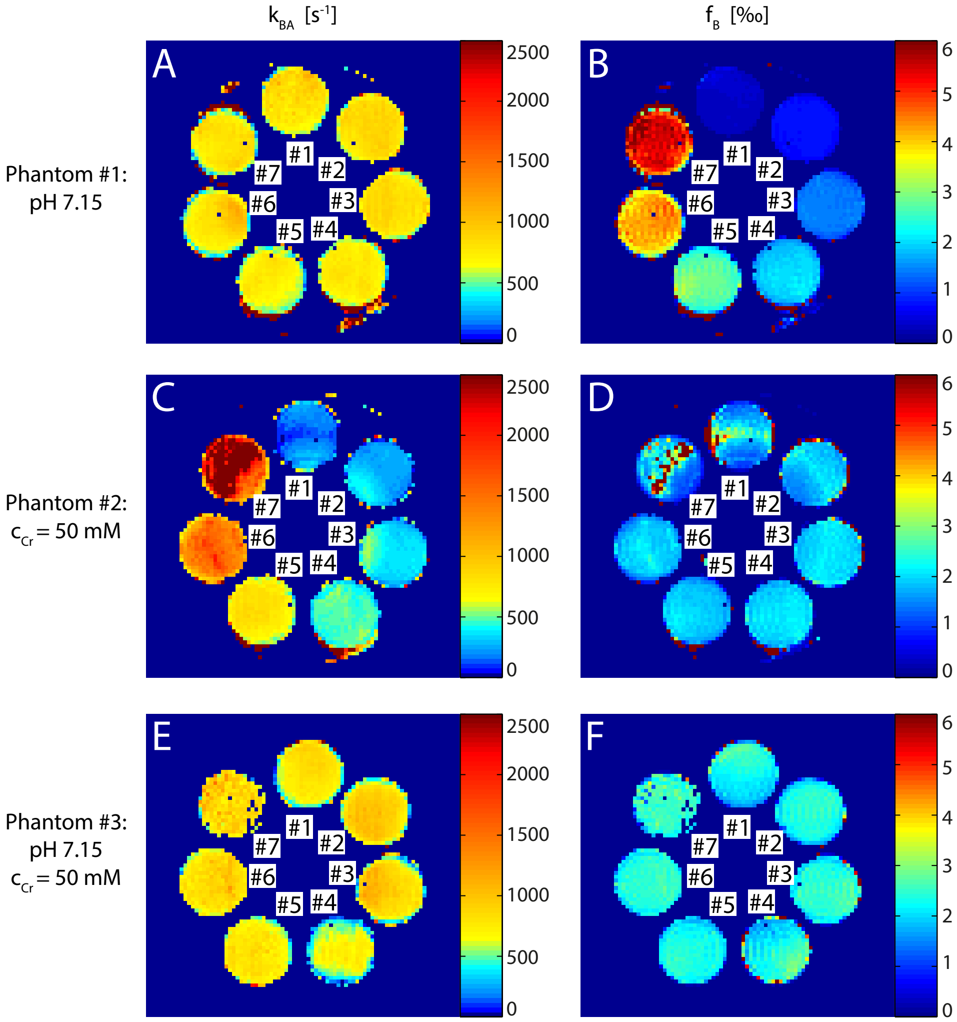

Figure 6.6.: Maps obtained by pixel-wise fitting of the Ω-plots yield the exchange rate k_{BA} (A, C, and E) and concentration f_B (B, D, and F) for the three phantoms (table 5.3). The exchange rates for phantom #1 show mostly no change (A), whereas the concentration depicts a strong dependence on c_{Cr} (B). In phantom #2, the relations are the opposite (C, D). The results in phantom #3 show mostly no variations for the selected relaxation parameter (E, F). For better visualization, all pixels with an asymmetry $Z(\Delta\omega = -1.9\,\text{ppm}) - Z(\Delta\omega = +1.9\,\text{ppm}) < 0.04$ were set to 0. The original image is from [104].

is stable over the whole phantoms #1 and #3, where a constant pH value is given (figure 6.7A, E). Averaging over all tubes yields with the form factors $k_{BA} = (800 \pm 65)\,\text{s}^{-1}$, while the application of the cw solution results in $k_{BA} = (525 \pm 43)\,\text{s}^{-1}$. *Haris et al.* published a value of $k_{BA} = (950 \pm 100)\,\text{s}^{-1}$ (diamond, dashed line) for a creatine solution with pH 7.0 at 37°C [13]. This value is shown for comparison as well as the result of the spectrometer measurement (figure 6.3) using cw saturation, $k_{BA} = (911 \pm 123)\,\text{s}^{-1}$ (square, dotted line). In the case of a changing pH value in phantom #2 (figure 6.7C) a clear exponential behavior can be observed, as expected for a base-catalyzed proton exchange (section 4.1). Fitting this relation results in $\mathcal{K} = 4.22 \pm 0.02$ for the extended Ω-plot method. The relative concentration f_B correlates linear with the creatine concentration c_{Cr} (figure 6.7B). Assuming four exchanging protons for the guanidinium group of creatine [27, 60] theoretical values can be derived using equation 4.12. It is apparent that the extended Ω-plot method vastly improves the estimation. Only a slight overestimation is visible for very high c_{Cr}. When the creatine concentration is not changed, the determined f_B stays constant within the error limits (figure 6.7D, F). The overestimation in phantom #3 are due to an inaccuracy in the calculated T_1-map.

6.2.2. Experimental determination of the form factors c_1 and c_2

Mathematical verification for linearity of the Ω-plots for any given pulse shape

The linear relation of $1/R_{ex}$ and $1/\omega_1^2$, which is exploited in the Ω-plots , is not obvious for any arbitrary pulse shape in equation (6.4). However, using equivalent transformations the following equation can be derived for the average exchange-dependent relaxation rate $\overline{R_{ex}}$:

$$\overline{R_{ex}} = \frac{f_B k_{BA}}{t_p} \sum_{l=1}^{\infty} \left(- \int_0^{t_p} \left(- \frac{\omega_1^2(t)}{k_{BA}(k_{BA} + R_{2B})} \right)^l \right) \mathrm{d}t \tag{6.11}$$

Every pulse shape can be divided into a time-independent saturation amplitude $\omega_1^2 = \gamma^2 B_1^2$ and a part describing the shape of the pulse $\varsigma^2(t)$. Consequently, the term ω_1^2 can be extracted from the integral:

$$\overline{R_{ex}} = \frac{f_B k_{BA}}{t_p} \sum_{l=1}^{\infty} \left(- \int_0^{t_p} \left(- \frac{\overline{\omega_1^2} \cdot \varsigma^2(t)}{k_{BA}(k_{BA} + R_{2B})} \right)^l \right) \mathrm{d}t \tag{6.12}$$

$$= \frac{f_B k_{BA}}{t_p} \sum_{l=1}^{\infty} \overline{\omega_1^{2l}} \left(- \int_0^{t_p} \left(-\varsigma^2(t) x^2 \right)^l \right) \mathrm{d}t \tag{6.13}$$

Thus the exchange-dependent relaxation rate R_{ex} slopes with ω_1^2, while the shape of the saturation pulse $\varsigma^2(t)$ contributes by a factor. Therefore, the resulting Ω-plot must be a straight line for any arbitrary pulse shape.

Improved estimation of k_{BA} and f_B

Besides the analytical solution an experimental approach allows to determine the form factors. Examination of the Ω-plots and consequently identifying the slope m and y-intersection n for the two different saturation schemes, e.g. cw and Gaussian-shaped saturation pulses, enables the use of equations (4.45), (4.46), (6.9) and (6.10). Independently of the saturation scheme, the resulting exchange rates k_{BA} and relative concentrations f_B should yield the same values, since they are only defined by the characteristics of the CEST pool. Thus, equating generates two equations with two unknown variables c_1 and c_2. Hence the form factors of the Gaussian-shaped pulse can be derived by:

$$c_1 = \frac{n_{CW}}{n_{Gaussian-shaped} \cdot DC} \tag{6.14}$$

$$c_2 = \sqrt{\frac{n_{CW} \cdot m_{Gaussian-shaped}}{m_{CW} \cdot n_{Gaussian-shaped}}} \tag{6.15}$$

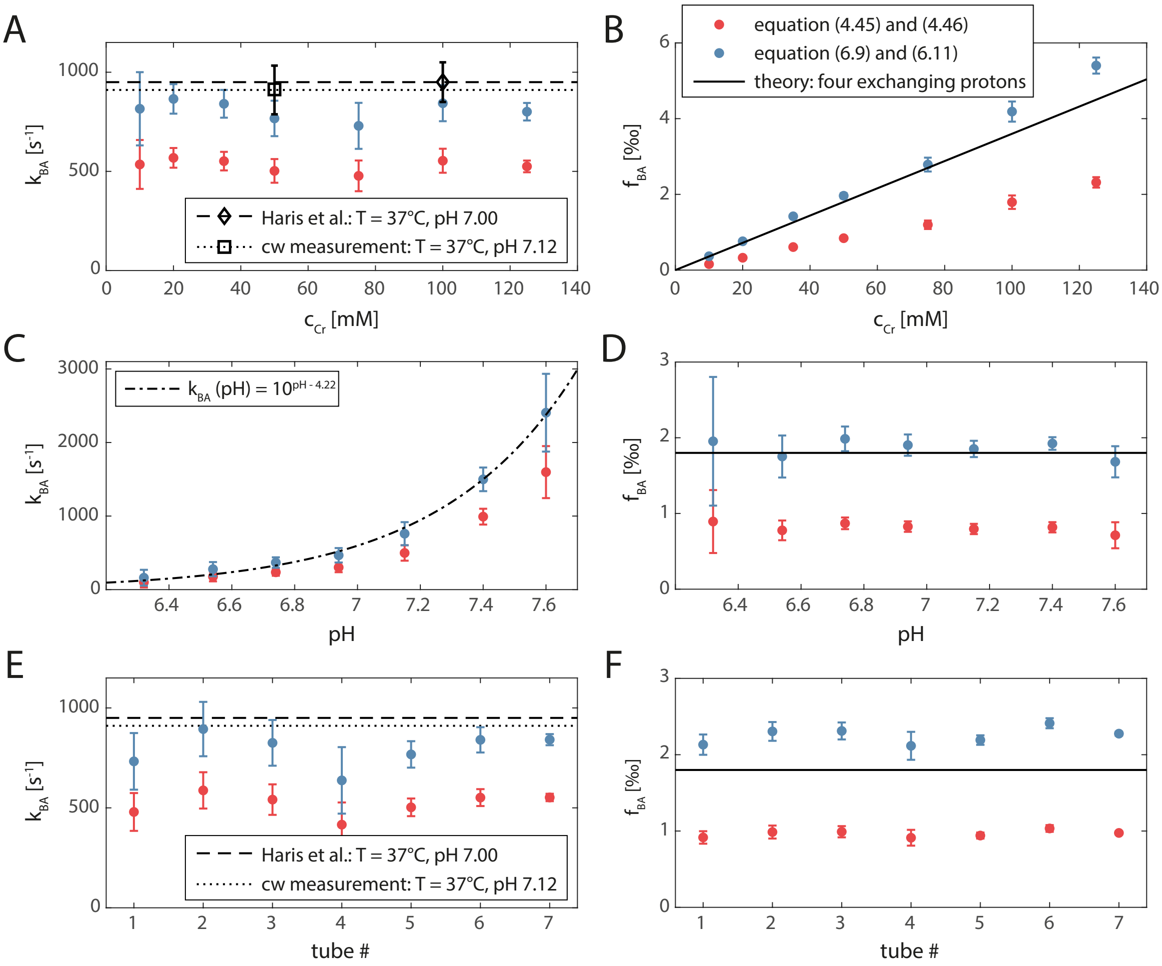

Figure 6.7.: ROI analysis of the three phantoms (table 5.3) for exchange rates k_{BA} (A, C, and E) and relative concentrations f_B (B, D, and F). The saturation was always carried out with 50 Gaussian-shaped pulses ($t_p = 0.1\,$s, $DC = 50\%$, $\sigma/t_p = 1/4.458$). The results based on the extended Ω-plot method (blue) are shown as well as the results for cw saturation (red). For comparison, the values $k_{BA} = (950 \pm 100)\,\mathrm{s}^{-1}$ (pH 7.00) of *Haris et al.* [13] (diamond, dashed line) and $k_{BA} = (911 \pm 123)\,\mathrm{s}^{-1}$ (pH 7.12) from the cw measurement (figure 6.3, square, dotted line) are displayed in (A) and (E). The dependence of k_{BA} on pH correlates well with an exponential function (dot-dashed line). The assumption of four exchanging protons for the creatine guanidinium group [27, 60] leads to a theoretical value for f_B (solid line) that is in good agreement with our extended Ω-plot method (B, D and F). The original image is from [104].

The values of the linear fit determined in the spectrometer measurement from section 6.2.1 (figure 6.3) result in $c_1 = 0.5672$ and $c_2 = 0.6171$. Comparing these values to the analytical derived form factors, i.e. $c_1^{ana} = 0.5623$ and $c_2^{ana} = 0.6678$, reveals a better labeling efficiency α of the Gaussian-shaped pulse.

Applying the newly derived form factors to equation (6.8) and repeating the simulations

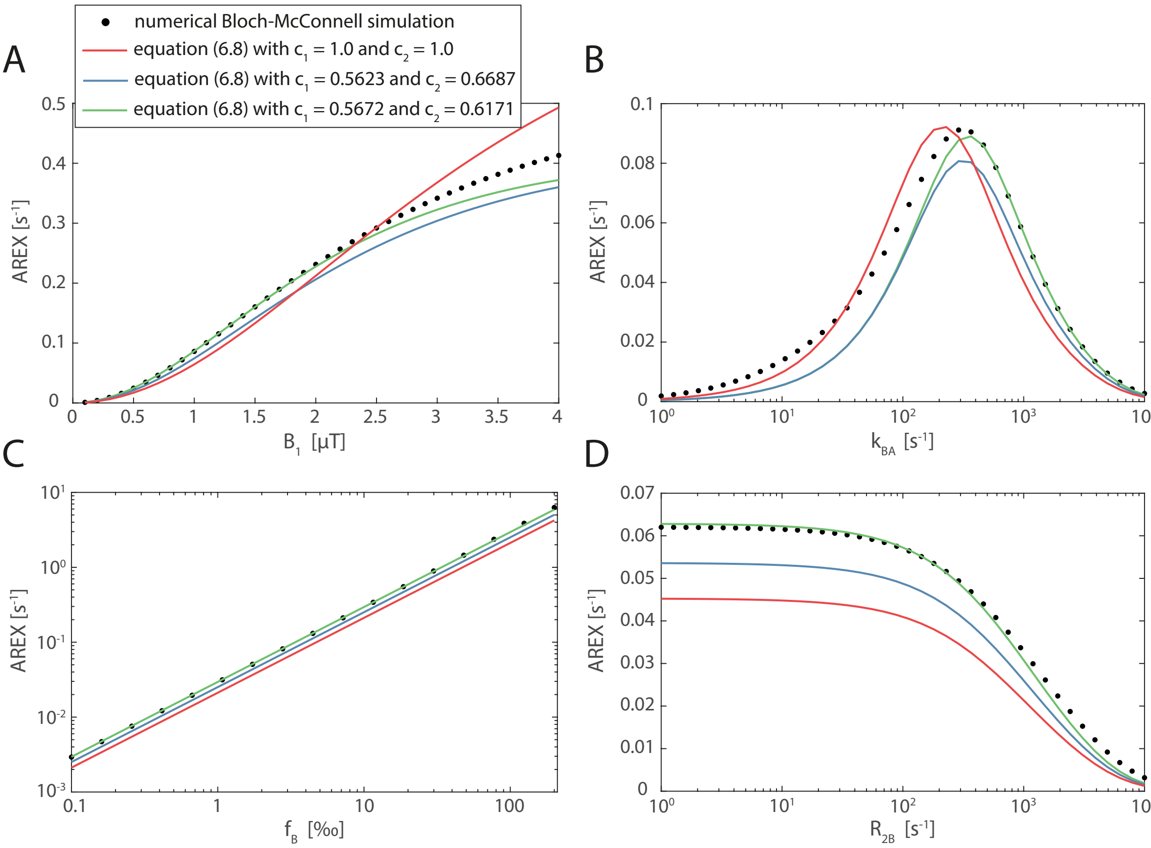

Figure 6.8.: Analytical and numerical simulation (black dots) of AREX for different B_1, k_{BA}, f_B and R_{2B}. The analytical solution with form factors $c_1 = 0.5623$, $c_2 = 0.6678$ (blue line) and $c_1 = 0.5672$, $c_2 = 0.6171$ (green line) are shown as well as the solution assuming a rectangular saturation pulse, i.e. $c_1 = c_2 = 1$ (red line). The simulation parameter for pool A and B are equal to the ones used in figure 6.1.

over a broad range of B_1, k_{BA}, f_B and R_{2B} as performed in section 6.1.1 shows a improved description of the apparent exchange dependent relaxation rate AREX (green line in figure 6.8). The solution describing the cw saturation (red line) and the original analytical solution (blue line) are shown for comparison. The simulation using the experimental determined form factors describe the Bloch-McConnell solution for the investigated parameters almost perfectly. Significant deviation can only be observed for high saturation amplitudes $B_1 \geq 2\,\mu\mathrm{T}$ and slow exchange rates $k_{BA} \leq 400\,\mathrm{s}^{-1}$.

These form factors also further improve the estimation of exchange rate k_{BA} and relative concentration f_B in the measurement of the creatine phantoms #1-#3 (figure 6.9). The published and in this thesis determined values for k_{BA} and f_B are shown again for comparison. Averaging the exchange rate over all tubes of phantom #1 and #2 yields now $k_{BA} = (870 \pm 73)\,\mathrm{s}^{-1}$. An exponential fit of the data in figure 6.7C results in $\mathcal{K} = 4.19 \pm 0.02$.

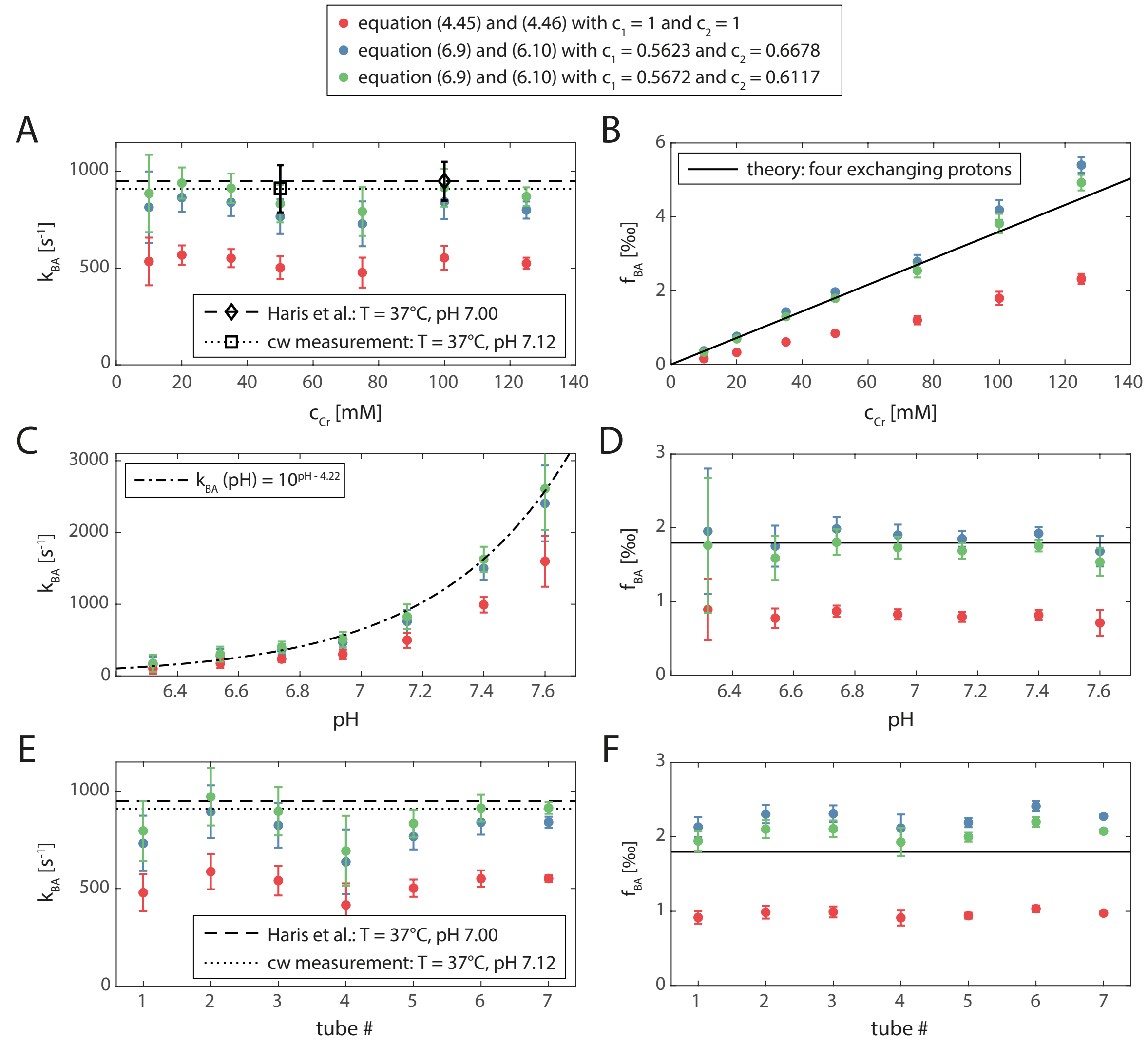

Figure 6.9.: ROI analysis of the three phantoms (table 5.3) for exchange rates k_{BA} (A, C, and E) and concentrations f_B (B, D, and F) are shown. The saturation was always carried out with 50 Gaussian-shaped pulses ($t_p = 0.1\,\mathrm{s}$, $DC = 50\%$, $\sigma/t_p = 1/4.458$). The results based on the extended Ω-plot method with the analytically derived $c_1 = 0.5623$ and $c_2 = 0.6687$ (blue) are shown as well as the results using the experimental determined form factors $c_1 = 0.5672$ and $c_2 = 0.6171$ (green). Red dots are results based on the Ω-plot method for cw pre-saturation ($c_1 = c_2 = 1$). For comparison, the values $k_{BA} = (950 \pm 100)\,\mathrm{s}^{-1}$ (pH 7.00) of *Haris et al.* [13] (diamond, dashed line) and $k_{BA} = (911 \pm 123)\,\mathrm{s}^{-1}$ (pH 7.12) of the cw measurement (figure 6.3, square, dotted line) are displayed in A and E. All in all The dependence of k_{BA} as a function of pH correlates well a exponential function (point-dashed line). The assumption of four exchanging protons for the creatine guanidinium group [27,60] leads to a theoretical value for f_B (solid line) which is in good agreement with our extended Ω-plot method as shown in B, D, and F.

The experimental determination of the form factors can be generalized to the case of two arbitrary pulses. Provided the form factors of pulse I are known, the calculation of the form factors for pulse II reads:

$$c_1^{II} = \frac{n_I \cdot DC_I}{n_{II} \cdot DC_{II}} \cdot c_1^I \tag{6.16}$$

$$c_2^{II} = \sqrt{\frac{n_I \cdot m_{II}}{m_I \cdot n_{II}}} \cdot c_2^I \tag{6.17}$$

This two equations enable now to investigate the quantitative behavior for any arbitrary pulse shape.

6.2.3. Investigation of other pulse shapes

To assess the equations (6.16) and (6.17) derived in the previous section, a creatine model solution with $c_{Cr} = 50\,\text{mM}$ and pH 7.15 (5.5.1) was investigated using several different pulse shapes at the 14.1T spectrometer. The resulting Z-spectra for different B_1 are illustrated in figure 6.10 for cw saturation (A) as well as pulsed saturation using Gaussian-shaped pulses (B), 1-lobe sinc functions (C), sinusoidal pulses (D) and sinc-like pulses provided by Philips (Philips, Amsterdam, Netherlands) (E). The measurement of $B_1 = 0.4\,\mu\text{T}$ for the sinc-like pulse was corrupted and is therefore not shown. All Z-spectra depict the expected CEST peak of the guanidinium group of creatine at around 1.9 ppm. The higher efficiency of a cw saturation compared to a pulsed saturation is already visible in the Z-spectra.

The actual shapes of the analyzed pulses are given in figure 6.11A. It should be noted, that the saturation involving shaped pulses is interleaved with a pause of duration $t_d = t_p$ between two successive pulses. AREX values at 1.9 ppm, i.e. $Z_{lab} = 1.9\,\text{ppm}$ and $Z_{ref} = -1.9\,\text{ppm}$, were calculated to compare the performance of the different saturation schemes (figure 6.11B). The cw saturation achieves for all saturation amplitude B_1 the largest effect. For $B_1 \leq 2\,\mu\text{T}$ the shaped pulses generate the most contrast in the following order: (1) 1-lobe sinc functions, (2) sinc-like pulses, (3) Gaussian-shaped pulses and (4) sinusoidal pulses. Surprisingly, for $B_1 > 2\mu T$ the order reverses completely.

The AREX values were used to determine the corresponding Ω-plots (figure 6.11C). The data (dots) of the cw saturation as well as the saturation using shaped pulses show clear linear behavior. Fitting of the data points to a linear function (dashed line) enables the application of equations (6.9) and (6.10), if the form factors and the DC are known. For the already known schemes using cw saturation ($c_1 = c_2 = 1$, $DC = 100\%$) and Gaussian-shaped pulses ($c_1 = 0.5672$, $c_2 = 0.6117$, $DC = 50\%$) this yield the tupel

$$\begin{aligned} \left(k_{BA}\left[\text{s}^{-1}\right] | f_B\left[‰\right]\right)_{cw} &= (908 \pm 36.6 | 1.74 \pm 0.09) \\ \left(k_{BA}\left[\text{s}^{-1}\right] | f_B\left[‰\right]\right)_{Gaussian} &= (920 \pm 78.7 | 1.81 \pm 0.07) \end{aligned}$$

respectively. The values for the exchange rate and the relative concentration determined for the saturation using Gaussian-shaped pulses are, within the error limits, in a good agreement with the values obtained by the original Ω-plot method presuming cw saturation.

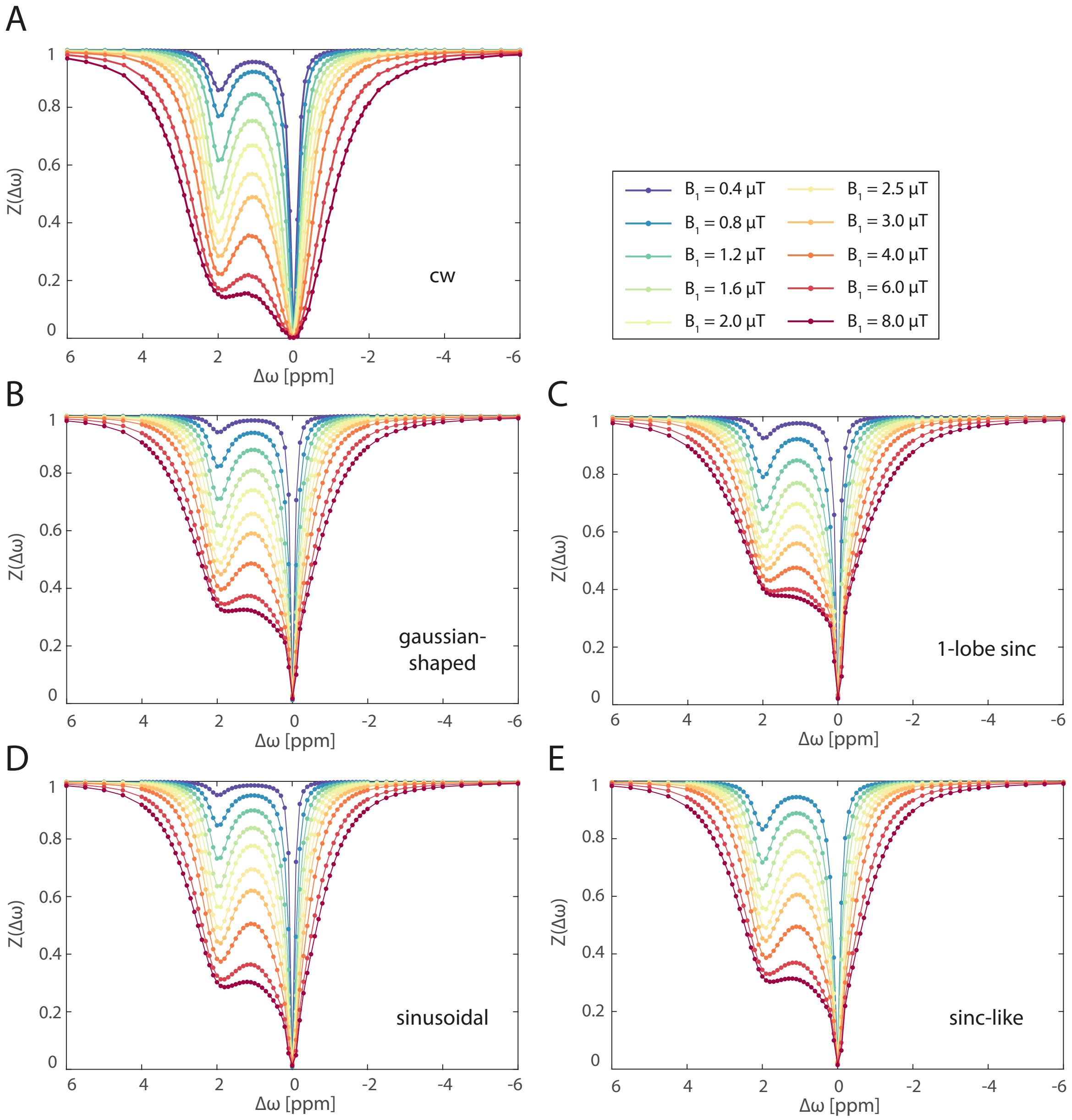

Figure 6.10.: (A-E) Experimental Z-spectra for different saturation schemes with various saturation amplitudes B_1 obtained in model solution measurements of phantom #S2 ($c_{Cr} = 50\,\mathrm{mM}$, pH 7.15, $T = 37°\mathrm{C}$) at $B_0 = 14.1\,\mathrm{T}$. The saturation time was $t_{sat} = 14.1\,\mathrm{s}$ for cw, whereas for the pulsed saturation 71 shaped pulses with $t_p = 0.1\,\mathrm{s}$ and $DC = 50\%$ were used. The pulses correspond to the shaped depicted in figure 6.11A. For the sinc-like pulse shape the measurement at $0.4\,\mu\mathrm{T}$ was corrupted.

As shown in section 6.2.2 the cw measurement can be used to determine the form factors of the shaped pulses, since the results for the exchange rate and relative concentration should yield the same value for each experiment independent of the saturation scheme. Hence, using equations (6.16) and (6.17) yields

$$\begin{aligned}
c_1^{Gaussian} &= 0.599 \pm 0.064 & \qquad c_2^{Gaussian} &= 0.625 \pm 0.035\\
c_1^{1\text{-}lobe\ sinc} &= 0.456 \pm 0.037 & \qquad c_2^{1\text{-}lobe\ sinc} &= 0.470 \pm 0.020\\
c_1^{sinusoidal} &= 0.762 \pm 0.075 & \qquad c_2^{sinusoidal} &= 0.785 \pm 0.039\\
c_1^{sinc-like} &= 0.654 \pm 0.072 & \qquad c_2^{sinc-like} &= 0.682 \pm 0.039
\end{aligned}$$

The form factors of the Gaussian-shaped pulse from this measurement are, within the error limits, equivalent to the ones obtained from figure 6.3 in section 6.2.2.

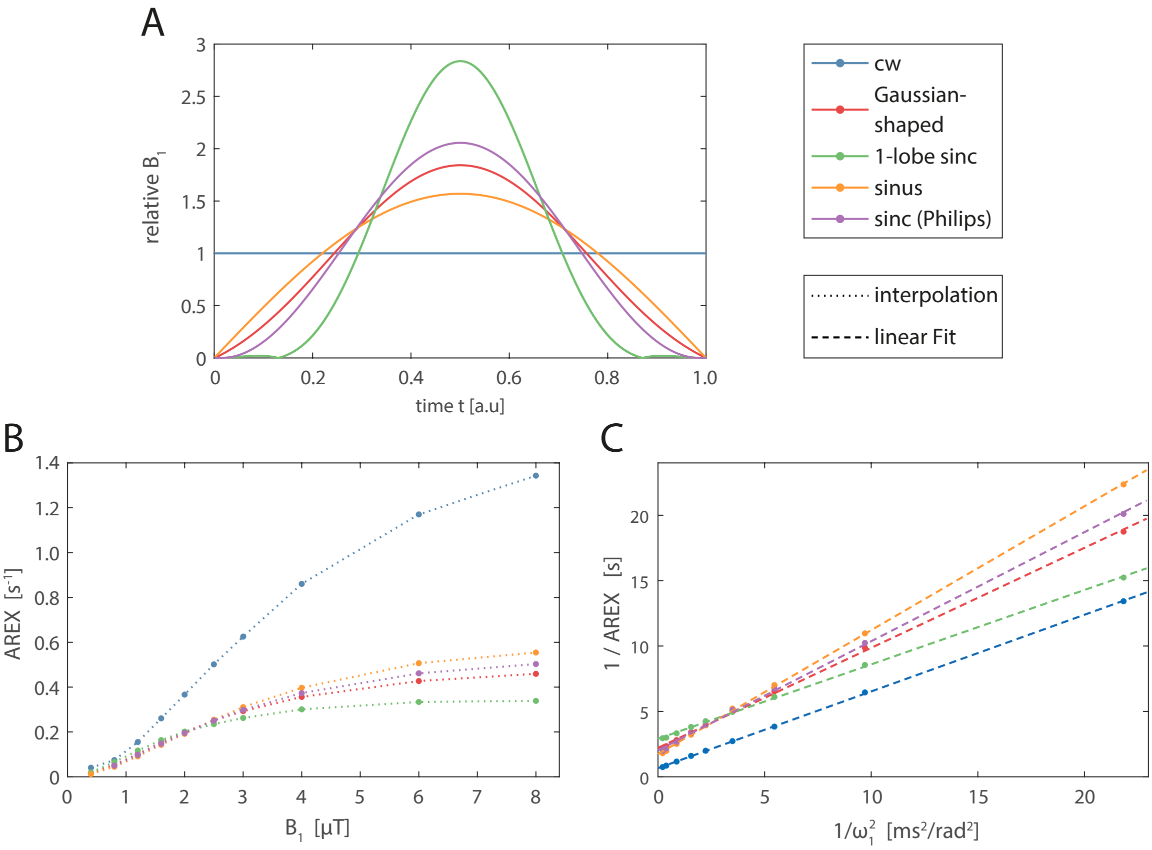

Figure 6.11.: The saturation characteristics of different pulse schemes are shown. All saturation pulses are normalized to satisfy $\frac{1}{t_p}\int_0^{t_p}\omega_1(t)\mathrm{dt} = \omega_1$ (A). The saturation involving shaped pulses is interleaved with a pause of duration $t_d = t_p$ between two successive pulses. After saturation of in total $t_{sat} = 14.1$s the resulting CEST effect at $\Delta\omega_B = 1.9$ppm differs dependent on the absolute saturation amplitude B_1 (B).

6.3. A proper Z_{ref} in multiple-pool systems

So far, all investigations were carried out using a pure composition of water and creatine. However, the complex in vivo system contains several overlaying effects. In figure 6.12 is a highly sampled in vivo Z-spectrum of the human calf of volunteer #1 depicted for different saturation amplitudes B_1. The saturation was performed by $n = 35$ Gaussian-shaped pulses with length $t_p = 0.1\,\text{ms}$, $DC = 50\%$ and the width-to-length ratio of $\sigma/t_p = 1/4.458$. The Z-spectra exhibit all different effects discussed in section 3.3. The direct water saturation dominates each Z-spectrum at $\Delta\omega = 0\,\text{ppm}$ and the broad semi-solid magnetization transfer (FWHM $\sim 50 - 100\,\text{ppm}$) increases with B_1 (figure 6.12A). The extract (figure 6.12B) from $-10\,\text{ppm}$ to $+10\,\text{ppm}$ shows the different effects of chemical transfer at $\Delta\omega_B \sim 3.5\,\text{ppm}$ and $\Delta\omega_B \sim 2.0\,\text{ppm}$ as well as the relayed Nuclear-Overhauser (rNOE) effect downfield from water (from $\Delta\omega = -2$ to $-5\,\text{ppm}$).

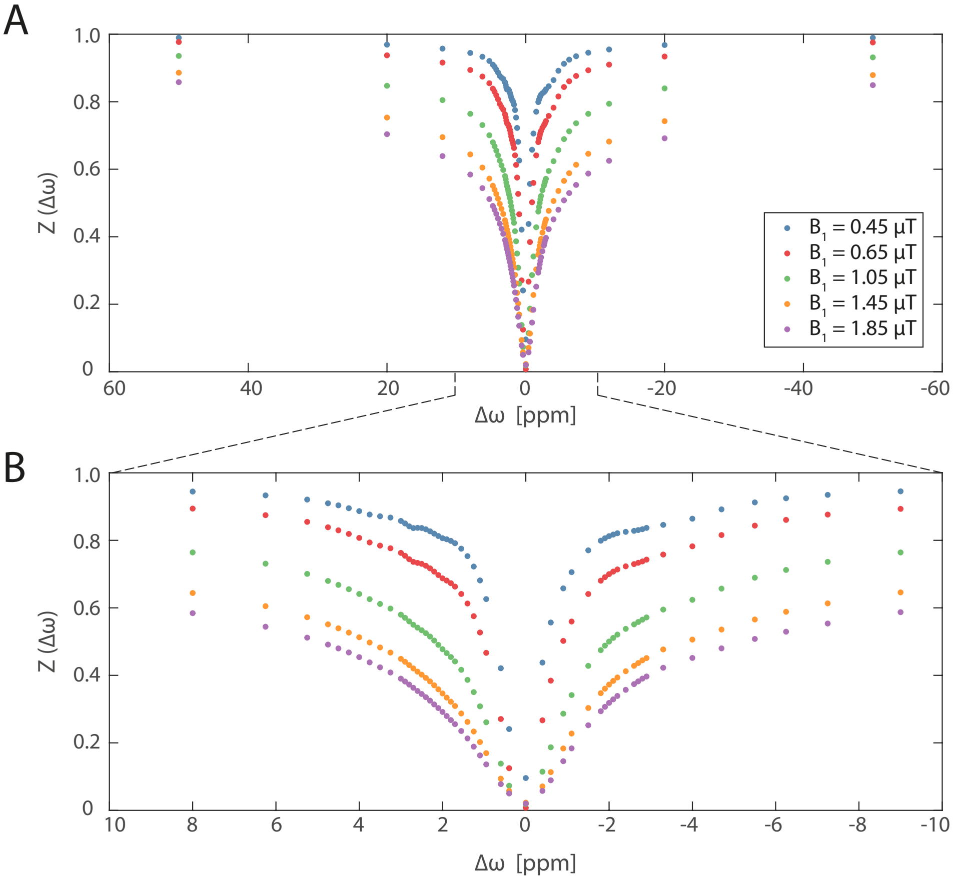

Figure 6.12.: In vivo Z-spectra from the human calf of volunteer #1 are shown for several different saturation amplitudes B_1. For better visibility the center of the Z-spectrum from $-10\,\text{ppm}$ to $+10\,\text{ppm}$ is enlarged. The legend applies for both graphs.

This system of multiple pools makes an isolation of the desired effect more difficult. Hence, the determination of Z_{ref} can not be done at the opposite offset frequency. In the following the performance of the multiple Lorentzian fitting method is investigated, as a good fitting algorithm would allow a characterization of all effects in the Z-spectrum.

6.3.1. Multiple Lorentzian fit analysis

Multiple Lorentzian fit algorithms were used to describe multiple pool systems like in vitro protein model solutions [99] and in vivo investigations in mice [90] and the human brain [70,89]. However, to date no application in the human calf was reported. Therefore the ability of the Lorentzian fit analysis to describe the Z-spectra was tested. Three different models, with varying number, combination and characteristics of pools, were used to fit the Z-spectra shown in figure 6.12. The models are composed by the pools given in table 6.1. The start parameters for the different pools were not changed between the models and are given in table 5.2.

pool describing	model #1	model #2	model #3
direct water saturation	✓	✓	✓
semi-solid magnetization transfer	✓	✓	✓
CE at $\Delta\omega_B \sim 3.5\,\text{ppm}$	✓	✓	✓
CE at $\Delta\omega_B \sim 1.9\,\text{ppm}$	✓	✓	✓
rNOE at $\Delta\omega_B \sim -3.5\,\text{ppm}$	✓		✓
CE at $\Delta\omega_B \sim 2.7\,\text{ppm}$		✓	✓

Table 6.1.: Composition of the three Lorentzian fit models.

Model #1 represents the common way to describe the in vivo situation. It was shown to work excellent in mice and human brain studies [70,89,90]. However, an additional CEST effect at $\Delta\omega_B \sim 2.7\,\text{ppm}$ is prominent in the Z-spectra of the human calf (figure 6.12A). This peak is assigned to the chemical exchange of amine groups [58]. While model #3 just adds this pool to the other existing ones, model #2 substitutes the rNOE pool. The rNOE is not primarily influential on the CEST effects upfield from water and could therefore be excluded to save measurement time.

The fit results are depicted in figure 6.13. For all three model the residuals are only larger than 5% close to the water resonance. Model #1 exhibits small deviations in the range of 2.7 ppm and 3.5 ppm (figure 6.13B). This can be attributed to the missing pool describing the amine exchange at 2.7 ppm. For model #2 the measurement points from $-1.5 \text{to} - 6.25\,\text{ppm}$ were excluded, which explains the deviations downfield from water. For better visualization these points are only shown by half opacity (figure 6.13B). Except from a poor fit for the smallest B_1 this model describes the chemical exchange upfield from water with good accuracy. Nevertheless, model #3 depicts the best performance in form of deviations between data and fit (figure 6.13C). Since model #3 has no disadcantages to model #2, except the presumable longer measurement time, it is used for all in vivo examinations of volunteers in the next section.

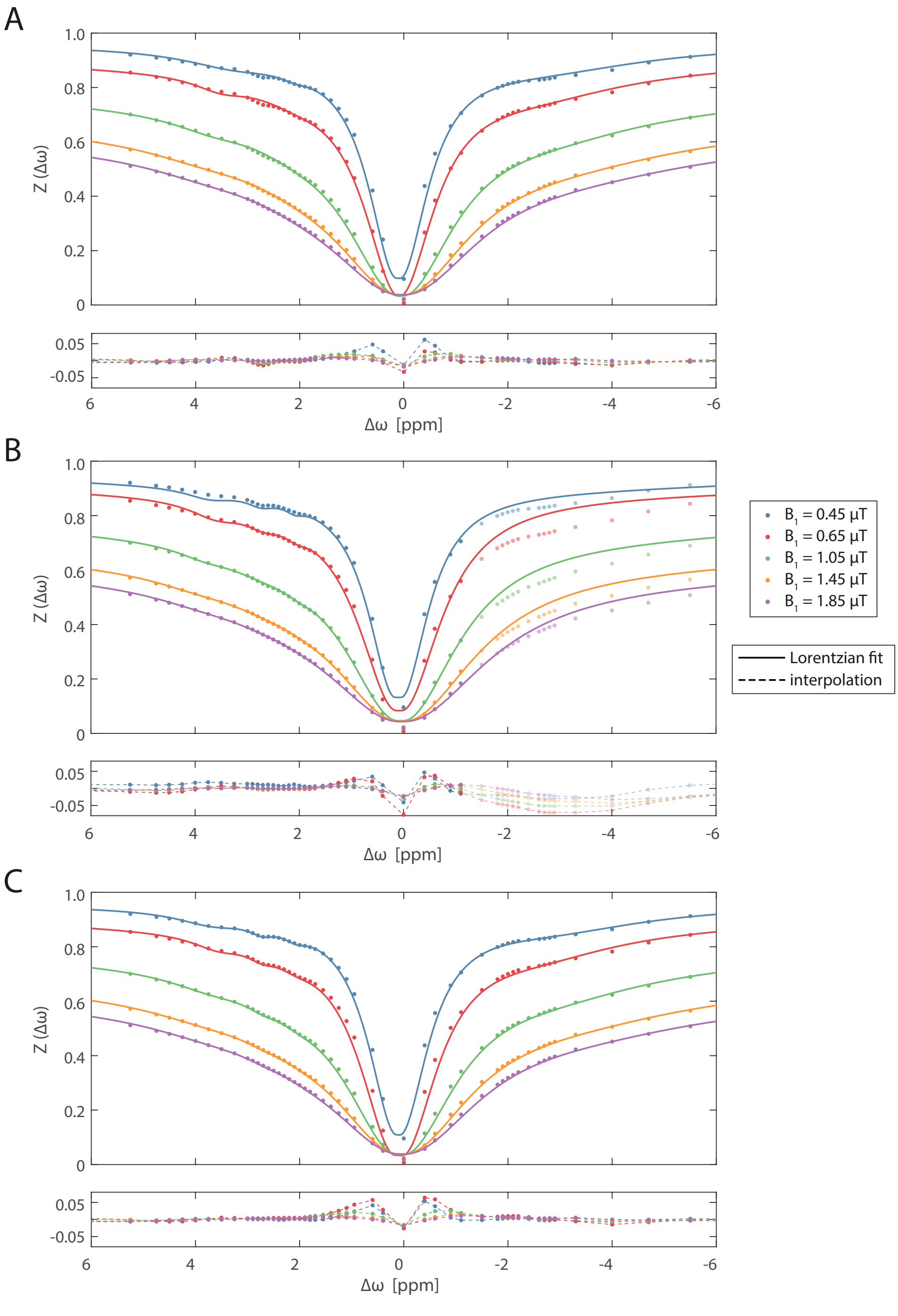

Figure 6.13.: The performance of different Lorentzian fitting models is depicted. Below the Z-spectra are the residuals between data and fit shown. All models include direct water saturation, semi-solid magnetization transfer, CE at $\Delta\omega_B \sim 3.5$ ppm and $\Delta\omega_B \sim 1.9$ ppm. Additionally model #1 includes a rNOE pool at $\Delta\omega_B \sim -3.5$ ppm (A), model #2 includes CE at $\Delta\omega_B \sim 2.7$ ppm (B) and model #3 includes both, the rNOE and CE at $\Delta\omega_B \sim 2.7$ ppm (C). In the case of model #2 the data points from -1.5 to -6.25 ppm were excluded from the fitting algorithm. The legend applies for all graphs.

Hence, the Lorentzian fitting algorithm is able to describe the Z-spectra in the human calf. In figure 6.14A is the exemplary fit for $B_1 = 0.45\,\mu$T with the single Lorentzian functions $\mathcal{L}$ shown. This spectrum illustrates the importance of the pool at $\Delta\omega_B \sim 2.7\,$ppm. As described in section 5.4.3 the result of the fit, i.e. the split into a Lorentzian function for each pool, is used to calculate AREX (figure 6.14).

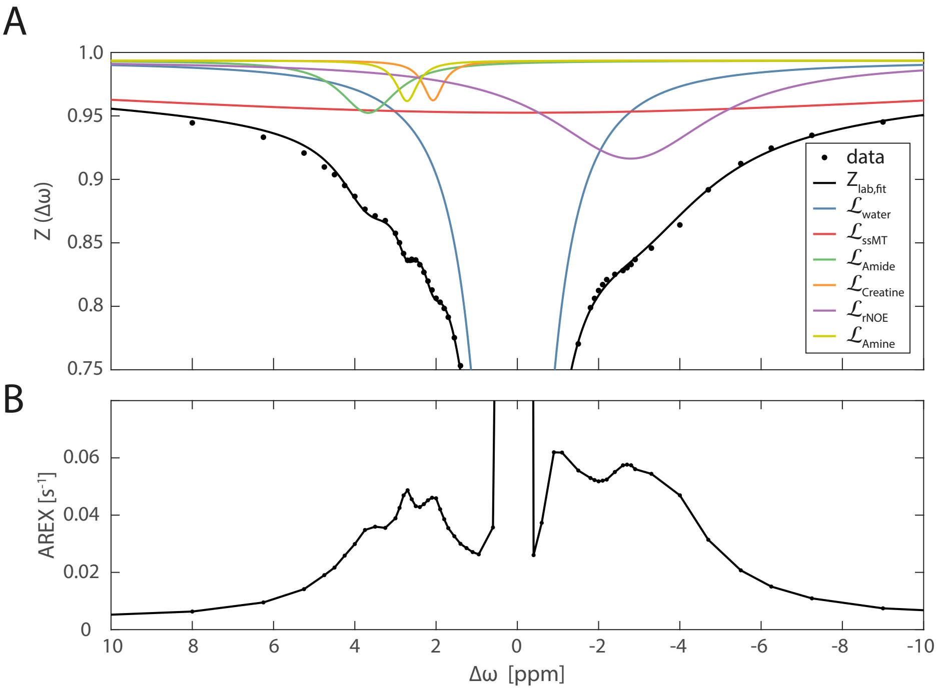

Figure 6.14.: 6-pool Lorentzian fit of the Z-spectrum in a ROI of the human calf at $B_1 = 0.45\,\mu$T. Only the center of the Z-spectrum is shown. The summation (black line) of all Lorentzian functions $\mathcal{L}$ (colored) depicts the measurement point (black dots) fairly good (A). AREX evaluation substracting the diluting effects of the direct water saturation and ssMT component yields distinguishable peaks (B). The AREX spectrum shows the different effects due to chemical exchange of amide protons (3.5 ppm), the guanidinium groups of creatine (1.9 ppm), amine protons (2.7 ppm) and the rNOE (−3.5 ppm).

6.4. Quantitative CEST in vivo

The analytical model and hence the extended Ω-plot method can, in combination with the Lorentzian fitting analysis, be used to investigate the quantitative behavior of metabolites conducting chemical exchange in vivo. Since it was shown, that the extended Ω-plot method does not work for slow exchange rate, the focus is set on the intermediate to fast exchange of the guanidinium group of creatine at the resonance frequency $\Delta\omega_B = 1.9\,\text{ppm}$.
From a physiological perception the human calf with its muscle composition (section 2.5.1) is the favored in vivo system. Using the relations between exchange rate and pH determined in section 6.2.2, and relative concentration and absolute concentration given from the assumption of four exchanging protons for creatine, allows the full quantitative characterization from a physical and biochemical point of view.

6.4.1. Exchange rate and relative concentration in the human calf

As shown in section 6.3 the apparent exchange-dependent relaxation AREX can be determined in vivo using the multiple Lorentzian fitting analysis. Figure 6.15A shows AREX spectra for different saturation amplitudes B_1 in a ROI within the *musculus gastrocnemius*. The effects due to chemical exchange of different functional groups at $\Delta\omega_B = 1.9\,\text{ppm}$, $\Delta\omega_B = 2.7\,\text{ppm}$ and $\Delta\omega_B = 3.5\,\text{ppm}$ and the rNOE at $\Delta\omega_B = -3.5\,\text{ppm}$ are visible. While for small B_1 the rNOE depicts the largest effect, the difference between $B_1 = 1.45\,\mu\text{T}$ and $B_1 = 1.85\,\mu\text{T}$ is negligible. All effects solely due to chemical exchange increase with increasing B_1. The peak of the guanidinium group of creatine at $\Delta\omega_B = 1.9\,\text{ppm}$ shows the most pronounced effect downfield from water. However, for very high B_1 the separation of the different peaks becomes more difficult. Close to the water resonance the 6-pool Lorentzian fit does not describe the in vivo situation in the human calf perfectly. Hence, the CEST effects are slightly diluted.

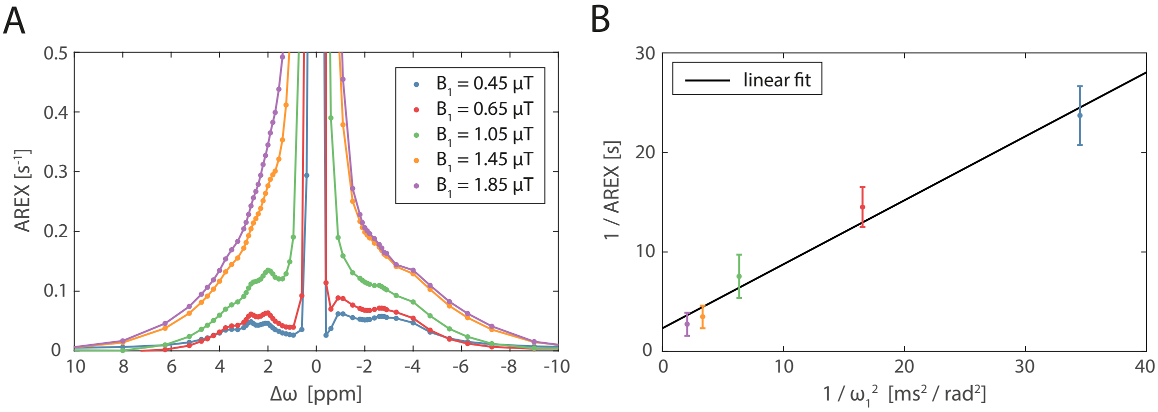

Figure 6.15.: AREX spectra of a ROI in the human calf are shown for different saturation amplitudes B_1 (A). The different effects due to chemical exchange and the rNOE are observable. The evaluation of the inverse AREX values at $\Delta\omega_B = 1.9\,\text{ppm}$ enables the Ω-plot analysis (B). The data points exhibit a linear relation. The fit results were: slope $m = (3.21 \pm 0.37) \cdot 10^5$ and y-intersection $n = 2.34 \pm 0.61$.

Nevertheless, the inverse AREX values at $\Delta\omega_B = 1.9\,\text{ppm}$ were plotted against $1/\omega_1^2$ (figure 6.15B). The colors of the different data points correspond to the colors used in figure 6.15A.

The data points correspond to a straight line. Linear regression (black line) yields the slope $m = (3.21 \pm 0.37) \cdot 10^5$ and y-intersection $n = 2.34 \pm 0.61$. The Ω-plot analysis, i.e. equations (6.9) and (6.10), results in the exchange rate $k_{BA} = (569 \pm 186)\ \mathrm{s}^{-1}$ and the relative concentration $f_B = (2.65 \pm 0.36)$‰.

The observed linearity and resulting values for the exchange rate and relative concentration permit a pixel-wise application of the equations (6.9) and (6.10) in vivo. Figure 6.16 depicts the transition from AREX maps at the resonance frequency $\Delta\omega_B = 1.9\,\mathrm{ppm}$ to the full quantitative parameter maps of the exchange rate and the relative concentration. For better visibility all non-relevant pixel were set to zero (black). The AREX maps show an increased contrast with increasing saturation amplitude (upper row). For low B_1 the maps are homogenous over the whole cross section, while for large B_1 the inhomogeneities increase. The cause of this is the inability of the correct isolation of the effects in the AREX spectra (figure 6.15). The inaccuracies near the resonance frequence of water result in a dilution of the CEST effects.

The Ω-plot method yields values for the exchange rate k_{BA} and relative concentration f_B. These parameter maps can be reconstructed within minutes (figure 6.16, lower row). Next to small hot spots or artifacts in the region of bones, veins or fasciae, the parameter maps are homogenous across the whole slice. Only a very slight tendency to higher values on the left side of the human calf is vaguely perceptible. This could be due to smaller muscle group diameter and hence a more diverse fibered structure, movement of the volunteer during the measurement time or a result of an inhomogeneous coil profile. However, even though different muscle regions are built of diverse types of filaments, the microscopical environment in a resting condition, and hence the characteristics of creatine, should approximately be the same and confirms the result of a homogenous distribution. The values for the exchange rate k_{BA} are in the range of $550\,\mathrm{s}^{-1}$, while the relative concentration f_B is about 2.3‰.

6.4.2. Physiological examination of four volunteers

Using a creatine model solution a correlation of exchange rate k_{BA} with pH value, and relative concentration f_B with absolute concentration c_{Cr} was determined in section 6.2. Assuming that the in vivo CEST effect at $\Delta\omega_B = 1.9\,\mathrm{ppm}$ is solely due to the protons of the guanidinium groups of creatine, the relations from figure 6.9 can be transformed to calculate the pH value and absolute concentration in vivo as follows

$$\mathrm{pH} = \log_{10}\left(k_{BA}\left[s^{-1}\right]\right) + 4.19 \tag{6.18}$$

$$c_{Cr}\,[\mathrm{mM}] = 27.75 \cdot f_B\,[‰] \tag{6.19}$$

The right calf of three additional volunteers were measured using almost the same protocol. The only two changes were (i) the reduction of the slice thickness to $\Delta z = 5\,\mathrm{mm}$ to show an applicability with lower SNR, and (ii) a reduction of the highest saturation amplitude value to $B_1 = 1.65\,\mu\mathrm{T}$ to reduce the total examination time due to the possibility of a decreased recover time M_{rec}.

The pixel-wise application of both equations on the measurement data for all four volunteers is shown in figure 6.17. The different rows show the parameter maps of k_{BA} (first row), f_B (second row), pH (third row), and c_{Cr} (fourth row), while the columns depict the different vounteers. The maps of volunteer #1 of k_{BA} (first row, left) and f_B (second row, left) are the already shown in figure 6.16. The parameter maps of the other volunteers are also homogenous and yield for all volunteers values in the same order. However, a slight tendency for higher values on the left side of the human calf can again be observed, especially for volunteer #3

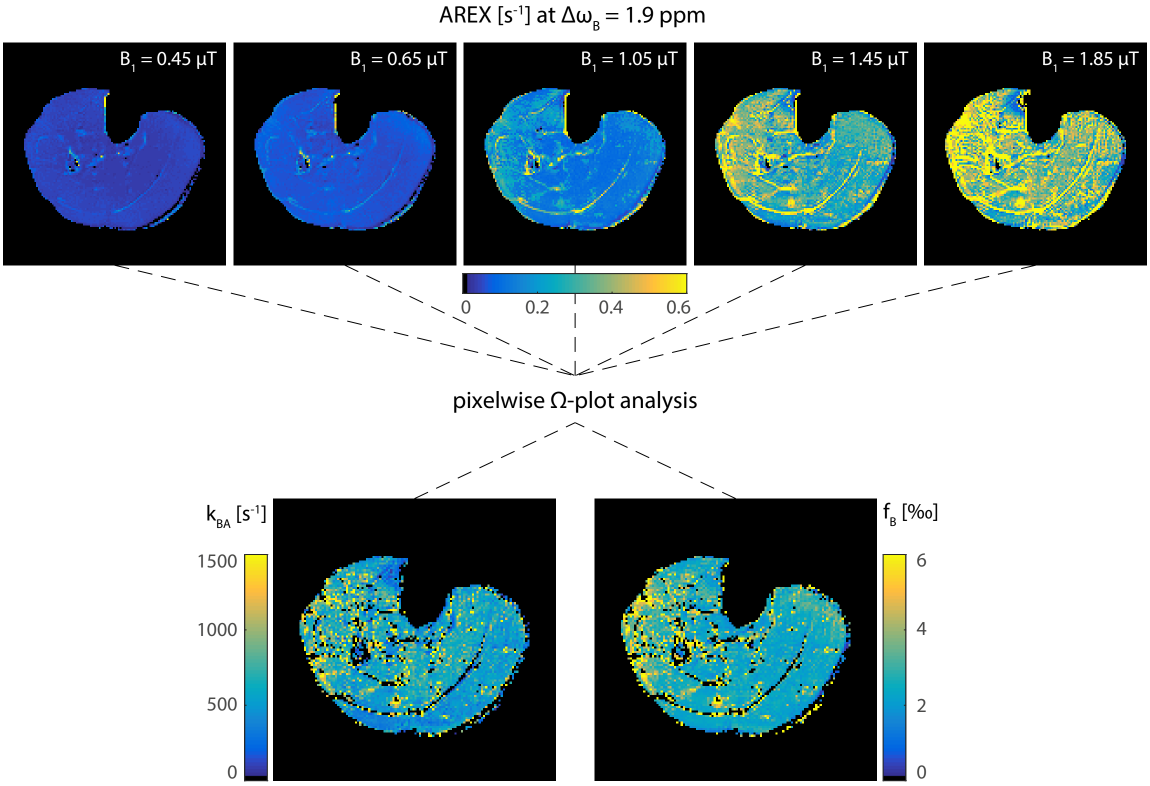

Figure 6.16.: AREX and the full quantitative parameter maps are shown of a cross section in the human calf of volunteer #1. The AREX maps were created for the resonance frequency $\Delta\omega_B = 1.9\,\text{ppm}$ (upper row). The colorbar below the middle image applies for all different B_1 values. After pixel-wise Ω-plot analysis, i.e. applying equations (6.9) and (6.10), the exchange rate k_{BA} and relative concentration f_B can be calculated (lower row). All non-physiological relevant pixel and all pixels were the fit generated non-physical values were set to zero (black).

(third column). Also an increased noise can be seen for volunteers #2, #3 and #4, which is caused by the decreased slice thickness. Nevertheless, a resolution of $1.17 \times 1.17 \times 5\,\text{mm}^3$ is sufficient to obtain a reasonable SNR for the quantitative CEST analysis.

Statistical evaluation of the whole calf

A statistical evaluation was performed to quantify the determined parameter maps. To keep the following pages clear, only the values for the respective questions are shown. The complete overview of all determined values is given in the Appendix F. The statistical behaviour was investigated using a bar plot analysis. Exemplary, the distribution of pixel with given pH is shown in figure 6.18. The statistical evaluation of the other three parameters is shown in Appendix G. The decreased amplitude in B,C, and D is due to the the higher resolution of the experiments in z-direction. This removal of averaged tissue also leads to the widening of the distributions. In a resting condition, the physiological (pH and c_{Cr}) and hence also the physical parameter (k_{BA} and f_B) should stay constant over the whole calf. Accordingly all deviations are due to measuring inaccuracy and the data should spread around a mean value

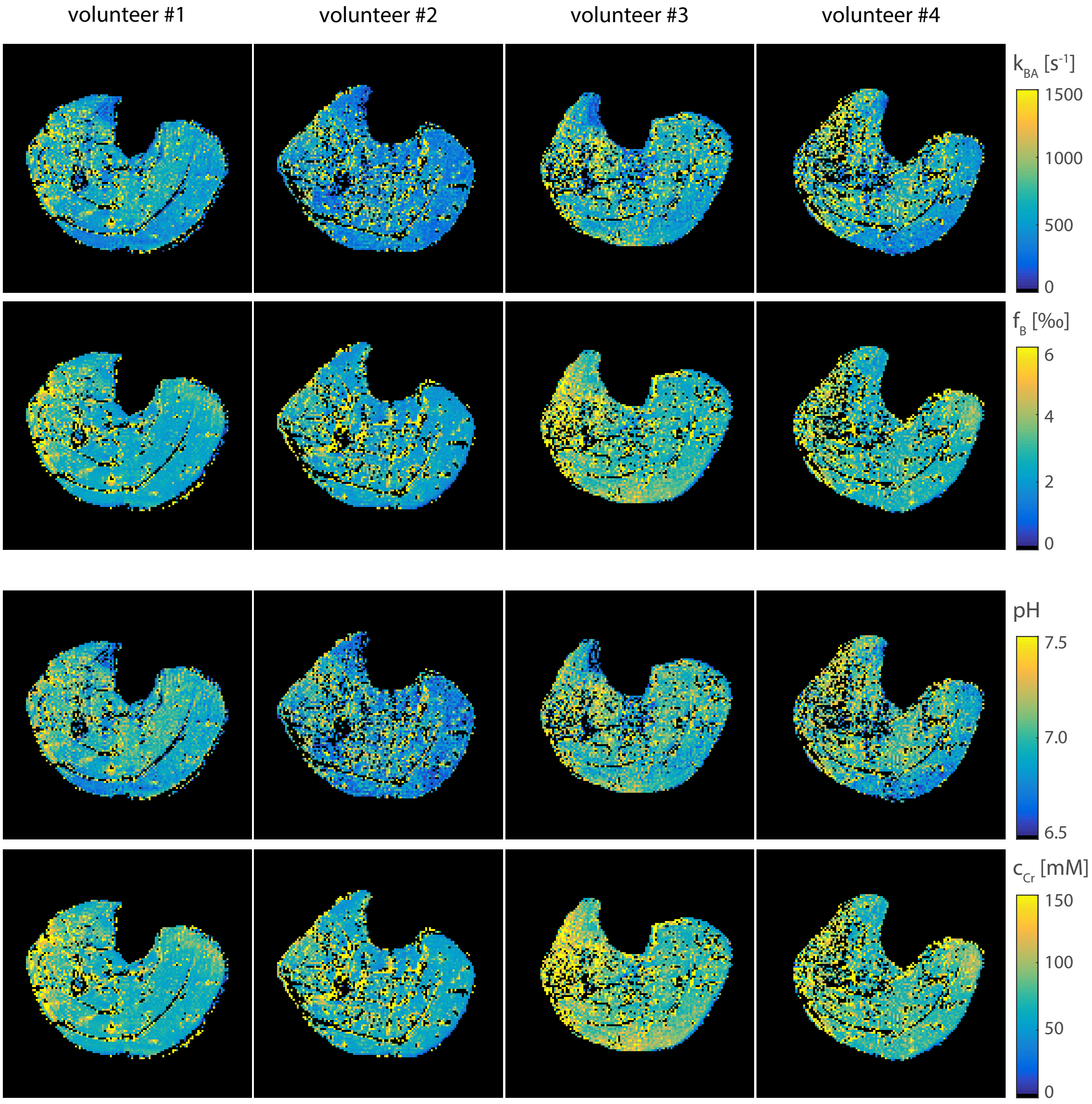

Figure 6.17.: Full quantitative maps are shown for a cross section of the human calf of the right leg of four healthy volunteers. The Ω-plot analysis allowed the determination of the exchange rate k_{BA} (first row) and relative concentration f_B (second row). Using equation (6.18) and (6.19) enabled the non invasive determination of the pH value (third row) and the absolute concentration of creatine in mM (fourth row). All non-physiological relevant pixel and all pixels were the fit generated non-physical values were set to zero (black).

like a normal distribution. Fitting a Gaussian function

$$f\left(pH|\mu,\sigma^2\right) = A \cdot exp\left(-\frac{(pH-\mu)^2}{2\sigma^2}\right)$$

to the distribution (black line) allows to determine a mean value as well as an error σ. The quantitative values for all parameters are given in table 6.2. The exchange rate k_{BA} of volunteers #1, #3 and #4 is in the range of $575\,\mathrm{s}^{-1}$ as expected from the Ω-plot performed on the ROI data (figure 6.15). Only volunteer #2 shows a reduced exchange rate of around $400\,\mathrm{s}^{-1}$. However, the values are quiet defective, as the errors are about 35%.
The obtained pH value is, within the error limits, around 7.0 in all four volunteers. This represents the physiological expected value in muscle tissue [105]. The relative and absolute concentration, f_B and c_{Cr}, differ between the volunteers. The diet and training status could influence the metabolite concentrations in muscle. This deviations were already visible in the second and fourth row in figure 6.17.

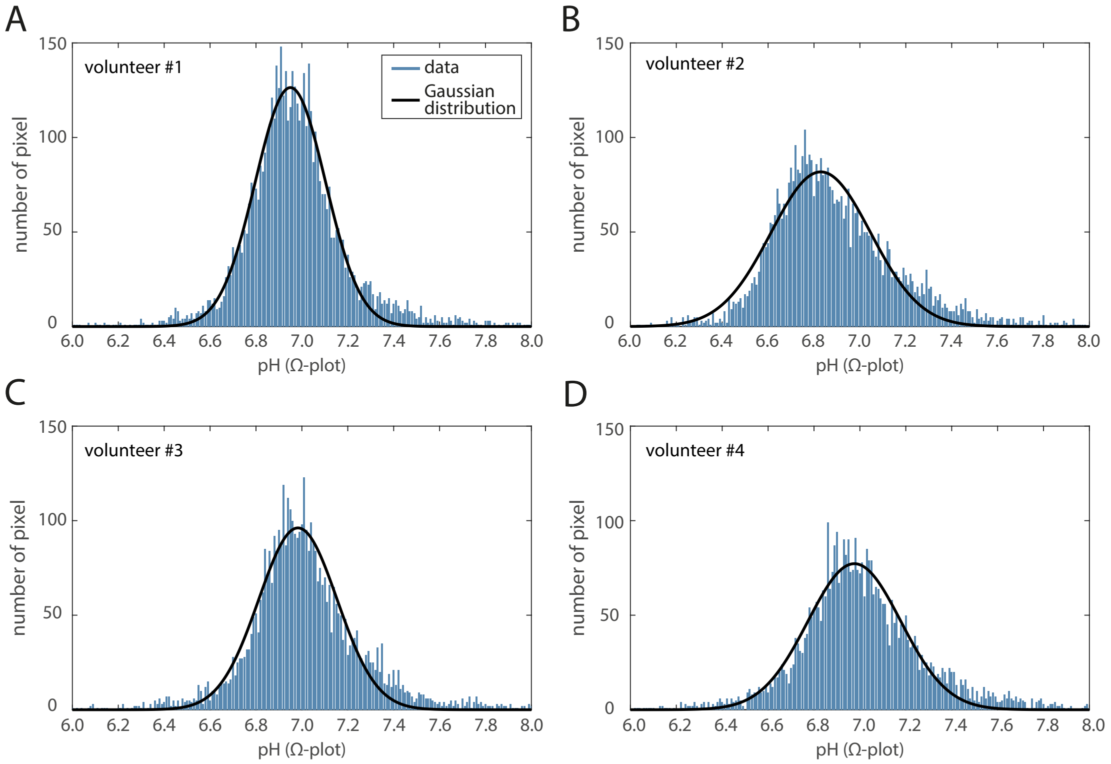

Figure 6.18.: The pixel-wise distribution of the pH value is shown (blue bars). The data spread accordingly to a Gaussian function (black line) around a mean pH value. The decrease in amplitude, and consequently increase of FWHM, for volunteer #2, #3 and #4 is caused by the lower SNR due to a higher spatial resolution (B-D).

	volunteer #1	volunteer #2	volunteer #3	volunteer #4	mean
k_{BA} [s^{-1}]	553 ± 185	394 ± 159	584 ± 207	562 ± 232	523 ± 198
pH	6.95 ± 0.15	6.83 ± 0.22	6.98 ± 0.17	6.98 ± 0.20	6.94 ± 0.19
f_B[‰]	2.36 ± 0.42	2.06 ± 0.48	2.88 ± 0.75	2.64 ± 0.60	2.49 ± 0.58
c_{Cr} [mM]	65.5 ± 11.9	57.3 ± 13.2	80.0 ± 20.9	73.2 ± 16.7	69.0 ± 16.1

Table 6.2.: In vivo quantitative CEST results determined by fitting a Gaussian distribution to the the pixel-wise results (as shown in figure 6.18).

Differentiation of different muscle regions

Even though the general distribution is homogenous across the whole slice (figure 6.17) and Gaussian-like (figure 6.18), some deviations can be seen between different regions. Therefore three muscle regions, *musculus gastrocnemius*, *musculus solues* and *musculus tibialis anterior*, were evaluated using a region-of-interest analysis. Exemplary are the ROIs shown for volunteer #1 in figure 6.19.

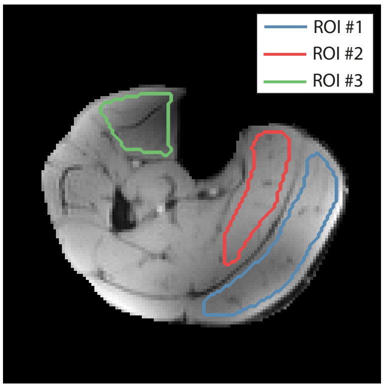

Figure 6.19.: Region-of-interest definition in the human calf of volunteer #1. The three muscle regions *musculus gastrocnemius* (ROI #1, blue), *musculus solues* (ROI #2, red) and *musculus tibialis anterior* (ROI #3, green) were examined.

The M_0 image of the measurement at $B_1 = 0.45\,\mu$T was used to indentify the muscle regions. The low resolution and contrast of this GRE sequence between muscle tissue and fasciae complicates the identification of borders, especially for the *musculus tibialis anterior.* A high resolution MR image, for example T_2-weighted turbo-spin echo, would improve the segmentation. Nevertheless, the ROIs were chosen by the best knowledge. The resulting values for pH and absolute concentration c_{Cr} are given for each ROI and volunteer in table 6.3.

at rest	ROI	volunteer #1	volunteer #2	volunteer #3	volunteer #4	mean
pH	#1	6.90 ± 0.14	6.78 ± 0.19	6.98 ± 0.19	6.90 ± 0.19	6.89 ± 0.18
	#2	7.02 ± 0.14	6.89 ± 0.23	7.05 ± 0.18	7.06 ± 0.22	7.01 ± 0.20
	#3	6.94 ± 0.24	6.77 ± 0.26	6.92 ± 0.27	7.08 ± 0.26	6.93 ± 0.26
c_{Cr} [mM]	#1	69.6 ± 16.8	64.6 ± 19.0	81.6 ± 22.3	85.2 ± 22.8	75.3 ± 20.4
	#2	69.8 ± 16.6	68.8 ± 27.2	82.1 ± 26.6	87.9 ± 29.4	77.2 ± 25.4
	#3	79.5 ± 24.9	63.0 ± 23.0	99.1 ± 29.7	80.8 ± 30.0	80.6 ± 27.1

Table 6.3.: ROI analysis of the quantitative CEST parameters obtained from all four volunteers. A schematic definition of the ROIs is given in figure 6.19.

As expected the pH values are in the range of 7. Even though within the error limits, a slight trend can be seen for the pH value between the different ROIs. While the *musculus solues*

(ROI #2) exhibits a pH of (7.01 ± 0.20) the other two muscle regions display a decreased pH of combined (6.91 ± 0.22). Both groups have a different dominant muscle fiber type, which could lead to a changed physiological environment.
Interestingly the creatine concentration varies between the volunteers and the ROIs. This is particular noticeable in ROI #3 depicting the *musculus tibialis anterior*. While the concentration for volunteer #1 and #3 is higher compared to the other muscle groups, volunteer #2 and #4 display smaller to equal concentrations in all muscle groups.

6.4.3. Investigation of muscle exercise

After the applicability of the extended Ω-plot method was shown in vivo in a resting condition, the investigation was repeated under exercise for volunteer #1. Plantar & dorsi flexion was induced in the calf using an MR-compatible foot pedal was used (section 5.6). To reduce image artifacts due to movement, the exercise was only carried out during the saturation, resulting in a pattern of about 6 s exercise followed by 3 s of rest. The volunteer was obliged to perform only mild exercise.
In figure 6.20A are AREX spectra during exercise for different saturation amplitudes B_1 shown. The ROI was selected similar to the examination under resting condition. In comparison to the measurement depicted in figure 6.15 the AREX spectra are not as smooth. These artifacts can be attributed to internal adjustment of the muscle fibers. The corresponding Ω-plot of AREX values at $\Delta\omega_B = 1.9\,\text{ppm}$ yields the slope $m = (2.95 \pm 0.62) \cdot 10^5$ and y-intersection $n = 1.97 \pm 0.89$ (B). This results in an exchange of $k_{BA} = (595 \pm 286)\ \text{s}^{-1}$ and a relative concentration of $f_B = (3.01 \pm 0.73)\,‰$. The values are slightly increased compared to the resting condition, however, the error limits are larger, too. Thus, no significant change is observable.

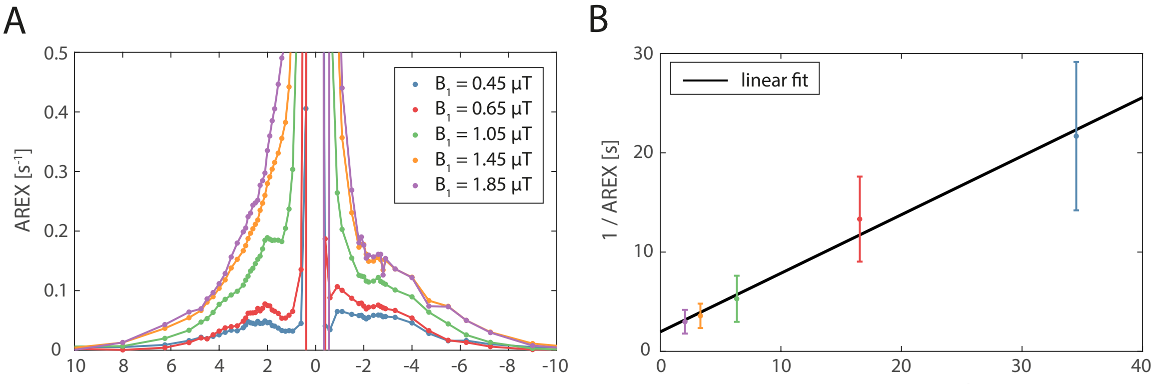

Figure 6.20.: AREX spectra of a ROI in the human calf during exercise are shown for different saturation amplitudes B_1 (A). The evaluation of the inverse AREX values at $\Delta\omega_B = 1.9\,\text{ppm}$ enables the Ω-plot analysis (B). The data points exhibit a linear relation. The fit results were: slope $m = (2.95 \pm 0.62) \cdot 10^5$ and y-intersection $n = 1.97 \pm 0.89$.

Nevertheless, the pixel-wise evaluation yielding pH and c_{Cr} was performed (figure 6.21 A and B). The parameter maps depict physiological differences between the muscle groups. The *musculus tibialis anterior* and *musculus gastrocnemius* appear to respond to the chosen exercise, while the *musculus soleus*, which primary role is maintaining a standing posture, exhibits no change. The creatine concentration c_{Cr} is strongly increased in the *musculus tibialis anterior* . However, this region also seems to be much more disturbed due to movement artifacts. Surprisingly, the *musculus gastrocnemius* appears to respond differently within itself to the performed exercise. To evaluate the different reaction two additional ROIs (#1.1 and #1.2) were defined (figure 6.21 C). The resulting mean values for all five ROIs are given in table 6.4.

Compared to the results of volunteer #1 under resting condition (table 6.3 column 3) is particular an increase of c_{Cr} in ROI #1.1 and pH in ROI #1.2 noticeable. The other values pH in ROI #1.1 and c_{Cr} in ROI #1.2, respectively, exhibit no change. As already addressed, the creatine concentration increases by about 20% in ROI #3.

during exercise	ROI #1	ROI #1.1	ROI #1.2	ROI #2	ROI #3
pH	6.98 ± 0.24	6.89 ± 0.22	7.06 ± 0.22	7.06 ± 0.19	6.89 ± 0.37
ΔpH	$+0.08 \pm 0.27$	-0.01 ± 0.27	$+0.16 \pm 0.22$	$+0.04 \pm 0.19$	-0.05 ± 0.37
c_{Cr} [mM]	80.1 ± 25.9	91.1 ± 22.1	68.3 ± 24.8	71.9 ± 19.6	109.8 ± 40.9
Δc_{Cr} [mM]	$+10.5 \pm 25.9$	$+21.5 \pm 22.1$	-1.3 ± 24.8	$+2.1 \pm 19.6$	$+30.3 \pm 40.9$

Table 6.4.: ROI analysis of the quantitative CEST parameters obtained of volunteer #1 during exercise. A schematic definition of the ROIs is given in figure 6.19 and 6.21. Mean values and error limits were determined by a Gaussian fit of the pixel-wise distribution.

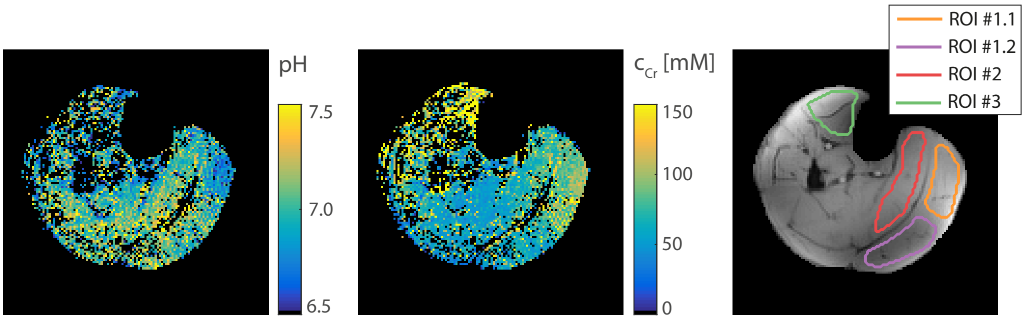

Figure 6.21.: The results of the quantitative CEST analysis for volunteer #1 performing exercise is shown. The maps of the pH-value (left) and absolute creatine concentration c_{Cr} (middle) depict varying physiological behaviors of the different muscle groups, which are schematically drawn in the anatomical image (right).

7. Discussion

The ideal and pure *Chemical Exchange Saturation Transfer* (CEST) effect, given by the exchange dependent-relaxation rate R_{ex} depends only on the exchange rate k_{BA} and the relative concentration f_B of the respective functional group under investigation. These in turn were reported to correlate with pH [12,25–27] and the absolute abundance of the solute containing the exchanging protons [12,14,106]. Hence, an evaluation method, which enables a quantitative determination of the CEST effect in vivo is of great interest as it could provide insight into the micro-environmental and physiological properties of tissue [107].
Previous publications addressing to solve this problem are restricted to a continuous-wave (cw) saturation [35,108] or exogenous CEST agents [30,33,109]. In this thesis, a solution is proposed to the lingering problem to characterize and quantify CEST data obtained in a clinical setup, i.e. on scanners that only permit pulsed saturation schemes.
The approach is based on the integration of $R_{1\rho}$ over the pulse shape yielding an analytical solution for the Z-spectrum in the case of pulsed saturation, which includes two form factors given only by the pulse shape. This allowed to extend *Dixon's* Ω-plot method [34] and consequently to determine k_{BA} and f_B. The application of this approach enabled high resolution pH imaging in the human calf.

7.1. Analytical solution

In the case of saturation by the means of shaped pulses the Z-spectrum, and especially the exchange-dependent relaxation rate R_{ex}, can be described in the steady state by the inclusion of the duty cycle DC, and the two form factors c_1 and c_2 into the previous model valid for cw saturation (section 6.1). Than the resulting signal in CEST experiments, the exchange dependent-relaxation rate (AREX [27]), is only modified by these two form factors to:

$$AREX_{shaped\ pulse} = DC \cdot f_B k_{BA} \cdot c_1 \frac{\omega_1^2}{\omega_1^2 + \left(k_{BA}\left(k_{BA} + R_{2B}\right) + \frac{k_{BA}}{k_{BA}+R_{2B}} \Delta\omega_B^2\right) \cdot c_2^2} \tag{7.1}$$

This new analytical Z-spectrum model for pulsed CEST was derived from an interleaved saturation-relaxation (ISAR [110]) approach. It assumes that the magnetization during saturation can be described by a decay with the longitudinal relaxation rate in the rotating frame $R_{1\rho}$ [38] and the recovery during the inter-pulse delay is given by the longitudinal relaxation rate of the water R_{1A}. The validity of this concept was demonstrated for saturation schemes with spin-lock pulses [27,110,111]. These approaches implicitly yielded a measure for the average saturation strength via $\overline{R_{1\rho}} = R_{1\rho}\left(\overline{\omega_1}\right) = R_{1\rho}\left(\frac{1}{t_p}\int_0^{t_p}\omega_1(t)\mathrm{d}t\right)$. Another common approach to calculate the saturation field strength of time-dependent pulses is the cw power equivalent [37,112]. However, the solution used in this thesis to calculate the average $\overline{R_{1\rho}}$ in the case of pulsed saturation is the integration of $R_{1\rho}$ over the pulse duration. The general validity of this approach was experimentally demonstrated for different pulse shapes and also mathematically derived for arbitrary pulse shapes (section 6.2.3).

7.1.1. Impact of the form factors

The introduction of the form factors does not affect the principal behavior of the pulsed CEST signal as a function of exchange rate, relative concentration and saturation amplitude compared to the cw case. However, they provide important information about several features, which are described in the following. The magnitude of each CEST effect obtained by pulsed saturation is lowered by the factor $DC \cdot c_1$ (figures 6.10 and 6.11B). Thus, the form factor c_1 can be interpreted as an 'intra-pulse duty cycle' [104]. It yields a measure about how much the shape of the saturation pulse matches a cw saturation: The flatter the pulse is at the peak amplitude, and consequently higher at the edges, the larger is c_1 (figure 6.11A). In the full saturation limit [31] these pulses result in higher CEST effects as shown in section 6.2.3.
However, if this limit is not reached the labeling efficiency α contributes to the signal (equation (4.27)) [88]. This factor describes the B_1 dispersion and is now altered by the form factor c_2 to an effective value $\frac{\omega_1}{c_2}$ [104]. For cw effects optimal labeling is obtained if $\omega_1 \approx k_{BA}$ [77,113,114]. For saturation with shaped pulses the form factor c_2 changes this rough estimation to $\omega_1 \approx k_{BA} \cdot c_2$. Additionally, this allows a transfer of optimal saturation strengths from one saturation scheme to another simply by the factor c_2.

The term *form factor* was chosen with reference to the atomic form factor $|F(\vec{q})|$ [115]. There the transition from the scattering of a particle at a point charge to extended charge distributions is made. In the case of pulsed CEST experiments the uniform cw saturation is transformed into a temporal, distribution of the saturation amplitudes.

7.1.2. Restrictions of the Z-spectrum model

The derivation of the Z-spectrum model (equation 6.5) contains several limitations, which are addressed below. First it must be mentioned that all restrictions are fulfilled in the clinical environment in the case of intermediate to fast exchange. Thus the model enables for example CEST studies of the guanidinium group of creatine [104].

The basic assumption was that the longitudinal relaxation rate in the rotating frame $R_{1\rho}$ is sufficient to parametrize the behavior of the magnetization under saturation. This has been revealed by *Trott and Palmer* [87] for saturation with spin-lock pulses and was recently shown to be true for CEST experiments as well by *Zaiss et al.* [38]. As already mentioned in section 4.3 this approach requires sufficiently long saturation times ($t_{sat} > T_{2A}$) and small concentrations of the CEST agent compared to the water pool ($f_B < 1\%$).
This description of the relaxation pathway was inserted in the interleaved saturation-relaxation (ISAR) approach to obtain a model to describe the Z-spectrum under saturation with pulses and inter-pulse delays. This was already shown for spin-lock by *Roeloffs et al.* [110]. It was also demonstrated, that the exchange dynamics during the inter-pulse delay t_d can be neglected if the exchange rate is sufficiently high ($k_{BA} > 1/t_d$). This results in a decay between two pulses, which is given by R_{1A}.
The successful integration of adiabatic spin-lock pulses [116] and given adiabaticity of off-resonant Gaussian-shaped pulses [75] enabled the analytical integration of $R_{1\rho}$ over the pulse shape performed in this thesis. At the resonance frequency of the CEST pool ($\Delta\omega_B = 1.9\,\text{ppm}$) the employed Gaussian-shaped pulse features a minimal adiabaticity of $\eta \geq 50.5$ for the used saturation strengths and therefore fulfills the adiabatic condition $\eta \gg 1$ [75]. Additionally, the calculation of the final result was only valid in the case of $\Delta\omega^2 > \omega_1^2/c_2^2$ and $k_{BA}(k_{BA} + R_{2B}) > \omega_1^2/c_2^2$ (Appendix D). This yields the deviations of the Z-spectrum model close to the resonance frequency of water ($\Delta\omega^2 < 0.5$) and thus excludes the investigation of exchanging groups that resonate close to water, e.g. the hydroxyl group of lactate [21].

In addition to the adiabaticity, the saturation pulse must be sufficiently long to avoid rotations of the magnetization around B_{eff}. These are not described by using the single eigenvalue approach [38, 95, 110]. These chemical exchange rotation transfer (CERT) effects [75, 117, 118] can be neglected for appropriate exchange rates ($k_{BA} > 1/t_p$). This, in combination with the limitation of the exchange rate for the valid calculation, explains the large deviations which are observed for small exchange rates (figure 6.2).
The accuracy of the analytically derived form factors of the Gaussian-shaped pulse is debatable, because the integration was performed for a real Gaussian function from − to + infinity (equations (D.34) - (D.36)). The pulse, as generated by the RF amplifier is finite and consequently the edges are lowered to minimize artifacts. The approximation is nevertheless acceptable, if the width of the pulse is small relative to its length ($\sigma/t_p < 0.5$). However, the derived form factors are only an approximation and vary slightly for the real pulses. An improved estimation can be obtained by either comparing cw with pulsed CEST data (section 6.2.2) or by numerical calculations.

In summary, the proposed analytical Z-spectrum model is valid if the following six conditions for the CEST pool and the saturation dynamics are met [104]:

(i) $f_B < 1\%$ (ii) $t_{sat} > T_{2A}$ (iii) $k_{BA} > 1/t_d$
(iv) $\Delta\omega^2 \geq \omega_1^2/c_2^2$ (v) $k_{BA} > 1/t_p$ (vi) $\sigma/t_p \leq 0.5$

In words:

The proposed Z-spectrum model is valid in the case of
studies with adiabatic saturation pulses
of low concentrated exchanging groups
in the intermediate to fast exchange regime
obeying the large-shift limit.

All these restrictions can be fulfilled on clinical MR scanners for CEST systems in the intermediate to fast exchange regime.

7.2. Quantitative pulsed CEST-MRI using Ω-plots

As mentioned above the ideal and pure CEST effect depends only on the micro-environment of the small exchanging pool. However, the contrast determined in CEST experiments is quiet complex, as it is regulated by several technical and physiological variables [77]. The influencing variables can be broadly divided into three main parts:

I) The proton pool specific exchange rate k_{BA}, which depends on the physiological parameters pH and temperature T, and the relative concentration f_B of the functional group. In the formula for the ideal CEST effect both parameters appear as a product [29–31].

II) The relaxation parameter of the free water molecules in the tissue and their altering influence on the CEST effect called spillover [31, 32].

III) The chosen saturation scheme, which has to comply with device-specific limits and the specific absorption rate (SAR) in the case of in vivo examinations [36, 37].

The possibility to determine the exchange rate and the relative concentration individually was already demonstrated. Most approaches use the dispersion of the CEST effect with the saturation strength B_1 (QUESP [30], optimal B_1 [119], multiple B_1 fit [31, 33]), however, also methods that take advantage of the dispersion with saturation length (QUEST [30]) or ratiometric approaches [32, 120] were reported. Mathematically the dispersion of the CEST effect can be transformed into a linear function of $1/B_1^2$ [34]. The evaluation of these so-called Ω-plots is simple, however, the signal must be free from influences of direct water saturation and is therefore limited to the investigation of exogenous PARACEST agents with large chemical shifts. The spillover effect arising from the direct water saturation can easily be corrected by applying the inverse metric [27]. This enables the application of the Ω-plot formalism to endogenous CEST agents with chemical shifts near the resonance frequency of water [35]. However, this solution is only valid for cw saturation. This in turn is not applicable on clinical whole-body scanners, which inhibit the quantification of the exchange rate and the relative concentration in vivo.

The analytical solution for pulsed saturation derived in this thesis can now be used to extend the Ω-plot method. This improves the estimation of exchange rate and relative concentration in the case of saturation by means of shaped pulses by rewriting the equations of the original Ω-plot method to:

$$k_{BA} = \left(-\frac{R_{2B}}{2} + \sqrt{\frac{R_{2B}^2}{4} + \frac{m}{n \cdot c_2^2}}\right) \tag{7.2}$$

$$f_B = \frac{1}{DC \cdot n \cdot c_1 \cdot \left(-\frac{R_{2B}}{2} + \sqrt{\frac{R_{2B}^2}{4} + \frac{m}{n \cdot c_2^2}}\right)} \tag{7.3}$$

7.2.1. AREX based Ω-plots

The linearity of the Ω-plots under pulsed saturation, as given in equation (4.39) and (D.43), is apparent for all various shaped pulses (figure 6.5 and 6.11). Though an additional assumption had to be made to derive this equation for the ‘pulsed theory‘. To derive AREX in the pulsed case small exponents in the exponential functions of equation C.19 must be assumed ($R_{1\rho} t_p \ll 1$ and $R_{1A} t_d \ll 1$). In the case of creatine in muscle (table 5.1) the longitudinal relaxation

rate in the rotating frame is $R_{1\rho} \approx 2R_{1A}$ for $B_1 = 1.85\,\mu$T resulting in an underestimation of about 2.5%. This approximation worsens for higher transversal relaxation rates of water R_{2A} and explains the deviations between and for low T_{2A} (figure 6.4).
As the proposed analytical Z-spectrum model is only valid in the intermediate to fast exchange regime – the sum in equation (D.48) only converges if $\omega_1^2 < 0.5 \cdot k_{BA}(k_{BA} + R_{2B})$ – the same is true for the AREX-based Ω-plots in the case of saturation using shaped pulses. In contrast, the original Ω-plot method [34] and the approach for cw saturation (equation (4.38) [35]) are not limited to a specific regime.

The independence of the steady-state AREX evaluation from water relaxation effects [27] is reflected in the Ω-plot method as the simultaneously determined exchange rate and relative concentration do not depend on relaxation parameters (figure 6.7 E and F). However, leaving the steady state condition ($t_{sat} \geq 5 \cdot T_{1A}$) leads to deviations (figure 6.4B). Despite a sufficiently long saturation, systematic deviations for k_{BA} and f_B can be seen (figure 6.4B and D). These can be attributed to the inaccurate integration performed for the Gaussian-shaped pulse as explained above. The use of the experimentally determined form factors minimizes the deviation (figure 7.1).

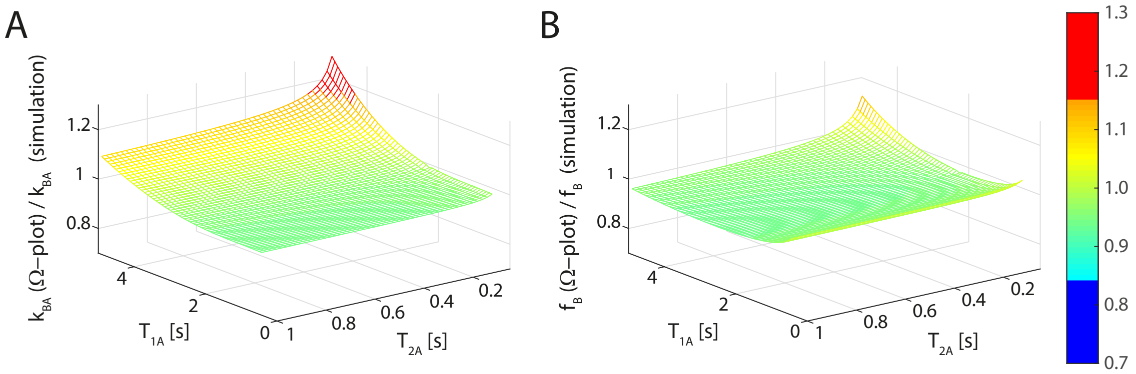

Figure 7.1.: The improved accuracy due to the experimentally determined form factors is depicted in simulations (figure 6.4 B and D). The normalized exchange rate (A) and the normalized relative concentration (B) are displayed as functions of the relaxation times T_{1A} and T_{2A} of the water pool. The color bar applies for both graphs.

7.2.2. Ω-plots for shaped pulses in experiments with phantoms at 7 T

Even though the analytical model and the extended Ω-plot method derived from it are severely limited by the restrictions described above, the obtained values for the exchange rate k_{BA} and relative concentration f_B in phantom measurements with creatine agree well with published values.

All values in this thesis were determined at the range of the body temperature. A published value for the exchange rate of creatine at $T = 37°\text{C}$ is $k_{BA} = (950 \pm 150)\,\text{s}^{-1}$ at pH 7.0 (*Haris et al.* [13]). Application of the original Ω-plot theory for cw saturation yielded $k_{BA} = (911 \pm 123)\,\text{s}^{-1}$ at pH 7.12. Saturation with several Gaussian-shaped pulses at pH 7.15 resulted without form factors in $k_{BA} = (525 \pm 43)\,\text{s}^{-1}$, with the analytically derived form factors ($c_1 = 0.5623$ and $c_1 = 0.6687$) in $k_{BA} = (800 \pm 65)\,\text{s}^{-1}$, and with the experimentally improved form factors ($c_1 = 0.5672$ and $c_1 = 0.6171$) in $k_{BA} = (870 \pm 73)\,\text{s}^{-1}$. While the spectrometer measurement and the result of *Haris et al.* are very similar, only the correction with the form factors ensures a reliable determination of the exchange rate for pulsed saturation.

Other publications investigated the correlation of exchange rate and pH. *Goerke et al.* [60] applied water exchange spectroscopy (WEX [121, 122]) to determine the exchange rates at temperature $T = 25°\mathrm{C}$, since WEX can only be used in the case of slow exchange. The applied extrapolation to $T = 37°\mathrm{C}$ yielded an exchange rate of $k_{BA} = (1500 \pm 150)\,\mathrm{s}^{-1}$. In contrast to the WEX method, the Ω-plot method enables a direct measurement of the exchange rates in the intermediate range, and the result of the spectrometer measurement should be more reliable ($k_{BA} = (911 \pm 123)\,\mathrm{s}^{-1}$) [104]. Even though the absolute magnitude is different, in both methods the exchange rate reflects, as expected for a base-catalyzed exchange [12], an exponential behavior as a function of pH (figure 6.9C). However, by heuristically setting the temperature in the function $k_{BA}(pH, T)$ of *Goerke et al.* [60] to $T = 31.55°\mathrm{C}$ a very good agreement can be obtained. This temperature yields the exponential factor $\mathcal{K} = 4.19$ in the case of the WEX experiment, equivalent to $\mathcal{K} = 4.19 \pm 0.02$ determined by the extended Ω-plot method with improved form factors. This could mean that the extrapolation of *Goerke et al.* only overestimates the exchange rates for high temperatures, however, is superior for low pH and accordingly in the slow exchange rate regime. Other groups published similar exponential behaviors. While *Desmond et al.* derived from [54] a value $\mathcal{K} = 4.4$ for creatine at $\Delta\omega_B = 2\,\mathrm{ppm}$ in mice [84], *McVicar et al.* stated $\mathcal{K} = 4.2$ for the amine exchange at $\Delta\omega_B = 2.7\,\mathrm{ppm}$ [85].

The number of exchanging protons of aqueous creatine, and hence the translation from relative to absolute concentrations according to equation (4.12), in the physiological range around pH 7.0 is still not completely elucidated. While the zwitterionic structure of creatine (figure 7.2) displays four exchanging protons arising from the transfer of a proton from the carboxy to the guanidinium group [123] and is dominant in the range from pH 4.0 - 12.0 at $T = 20°\mathrm{C}$ [124–126], an increased occurrence of the neutral, or other forms, at higher temperatures can not be ruled out. However, as well as the determined correlation in this thesis, published values suggest 4 exchanging protons for the guanidinium group of creatine [27,60,94] also at $T = 37°\mathrm{C}$ at least for pH in the range of 6.3 to 7.6. The deviation observed for high absolute concentrations of creatine are probably due to the restriction (i) of the analytical model (section 7.1.2).

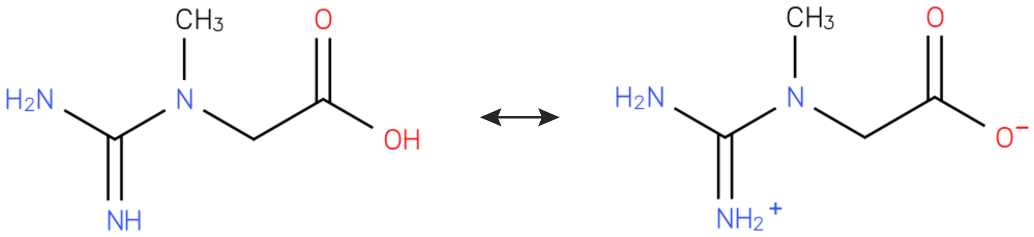

Figure 7.2.: The native (left) and zwitterionic (right) form of creatine. The transition arises from a transfer of a proton from the carboxy (red) to the guanidino (blue) group. The zwitterionic structure is dominant at pH 4.0 - 12.0 [124]. Images taken from [123].

As for most CEST experiments performed on a whole-body scanner a reliable knowledge of the spatial distribution of the B_0 and B_1 field is of utmost importance. The proposed Ω-plot method is particularly prone to variations of B_1 and based on the asymmetry analysis also to B_0-inhomogeneities. A B_0-correction is straightforward (section 5.4.2) and the needed ΔB_0 map can easily be obtained [101, 102]. However, also elaborated sequences [76, 118] or fitting approaches [31, 89, 90, 103, 127] can bypass this matter. The actual flip-angle distribution provided by the scanner can also be determined using sophisticated sequences [102, 128] or instead be corrected for B_1-inhomogeneities [103, 129]. Lately, also so-called pTx (multi-channel transmit [130, 131]) methods were used to increase the B_1-homogeneity in the FoV of the whole-body scanner [132, 133].

7.3. Quantitative CEST in vivo

The in vivo application of the Ω-plot method was for the first time possible using the above described form factors. Based on the herein proposed analytical model [104] an application in the intervertebral disc in a porcine model was published investigating the hydroxyl group of the glycosaminoglycan (GAG) components [134].

The technical and safety limitations of whole-body scanners [36,37] are a major issue regarding in vivo studies. However, sufficient saturation can be irradiated with a train of shaped pulses to achieve the steady state, which allows the utilization of the extended Ω-plot method. Compared to conventional spectroscopy sufficient SNR can be generated even for high spatial resolutions of about $1.17 \times 1.17 \times 5\,\text{mm}^3$.

7.3.1. Determination of the reference value Z_{ref}

A complex superposition of several different signals such as chemical exchange, rNOE and semi-solid MT occurs for in vivo CEST investigations. A sufficient isolation, meaning a proper identification of Z_{ref}, of the desired CEST effect can be obtained by Lorentzian fitting of the peaks. Usually a five-pool model is assumed to describe the Z-spectrum in the small animal and human brain [31,89,90,103], however, in the case of the human calf muscle an additional pool at $\Delta\omega_B = 2.7\,\text{ppm}$ must be considered in the fitting routine (section 6.3). This yields decreased residues upfield from water. Optimizing the measured frequency offsets might enable the use of a two-pool model, including only direct water saturation and semi-solid MT, while reducing the over parametrization of the fit [99,127,135].
Whether the shape of the semi-solid MT is actual Lorentzian-like has not yet been clarified. However, its influence, modifying $R_{1\rho}$ and R_{1A} of water [66], was also recently demonstrated to be mathematically describable applying the $R_{1\rho}$ model [136]. Thus, the use of the suggested R_{1obs} could allow to apply the pulsed Ω-plot method in the presence of a semi-solid MT by changing equations (7.2) and (7.3) appropriately (Appendix E). The reference value could also be acquired by other methods including extrapolation of MT [137], three-point methods [26, 27,138], variable flip-angle methods [75,118], or variable delay-time approaches [76,139]. The acquisition of many frequency offsets and subsequent utilization of the fitting algorithm could be avoided by a combination of transfer-rate-edited CEST approaches [68,70] and asymmetry analysis.

7.3.2. Physical and biochemical properties of the human calf

Ω-plots in the human calf

The in vivo application of Ω-plots is possible by the appropriate determination of Z_{ref} (section 6.4.1). The linearity is given in the examined saturation amplitude range. This is the first known application to the human calf. The mean values over the whole calf of the exchange rate, $k_{BA} = (523 \pm 198)\,\text{s}^{-1}$, and the relative concentration, (2.49 ± 0.58)‰, are within the expected order of several hundred s^{-1}. Moreover, the homogeneity of the k_{BA}- and f_B-maps of four different volunteers with comparable values supports the assumption that the results are not accidental.

Physiological evaluation and origin of the signal

The application of the correlations determined in the phantom measurements to the in vivo situation enable the determination of biochemical parameters – pH and absolute concentration – instead of parameters of the chemical exchange. These physiological variables in turn are well known and studied by other methods, which, however, have major drawbacks such as very long measurement times, low spatial resolutions or require tissue biopsies. Averaging of the data over the whole calf of four volunteers yielded $pH = (6.94 \pm 0.19)$ and $c_{Cr} = (69.0 \pm 16.1)$ mM. In general the obtained pH is in good agreement with the physiologically expected value of about 7 in the muscle [50]. Precise measurements of the pH were performed in muscle homogenates of the *musculus quadriceps femoris* using a pH-meter yielding $pH = (6.92 \pm 0.03)$ [140], and using ^{31}P spectroscopy resulting in $pH = (7.04 \pm 0.01)$ [141] in a region mostly consisting of the *musculus gastrocnemius*. Even though the values agree within the error limits, a small underestimation of the pH value is observed. The measured concentration is significantly larger than all published values for sole creatine concentration $c_{Cr} \cong 10 - 15$ mM [105, 142, 143]. The differences in concentration indicate other contributions to the signal.

The origin of the CEST signal at $\Delta\omega_B \sim 1.9$ ppm in the human calf is attributed to be the guanidinium group of creatine [14, 15, 144, 145]. A correlation with creatine was also shown in rat brain [146, 147], however, recently a CEST effect at $\Delta\omega_B \sim 1.9$ ppm was observed in proteins. The guanidinium group of the amino acid *arginine* was assigned to the effect in BSA studies [58]. The relative abundance of arginine in proteins is about 5-6% [148, 149] and its molar weight is $M_{arg} = 174.20$ g/mol. Assuming a total protein weight per cell of $7 \cdot 10^{-10}$ g and an average cell volume of $3.4 \cdot 10^{-9}$ ml [150] would yield an arginine concentration of $c_{arg} \approx 59$ mM. Due to the spatial composition of the proteins, i.e. tertiary and quaternary structure, it remains unclear how many of these arginine amino acids actually interact with free water molecules, so that the effective concentration is probably lower. The rough estimation of the concentration, nevertheless, yields a value in the *millimolar* range and should not be neglected when investigating the chemical exchange of guanidinium groups at $\Delta\omega_B \sim 1.9$ ppm in vivo.

Additionally, effects of phosphocreatine (PCr) were reported at the resonance frequency $\Delta\omega_B \sim 1.8$ ppm with slower exchange rates of about $k_{BA} \sim 130\,\mathrm{s}^{-1}$ [61]. However, the used saturation pulse parameters potentially preclude or at least suppress the detection of the slow exchanging amine protons in PCr [13]. Nevertheless, a small influence can not be ruled out, so that a slight reduction of the exchange rate could occur. Nevertheless, the total creatine concentration, i.e. $c_{tCr} = c_{Cr} + c_{PCr}$, is stated at $\sim 40 - 50$ mM [105].

Further, CEST signals upfield from water are artificially increased by additional rNOE contributions [71]. Aromatic protons of covalently bound C-H$_\mathrm{n}$ groups are suspected as the origin of this effect [151]. It has now been suggested by *Zaiss et al.* that the effect of aromatic and aliphatic rNOE in the Z-spectrum correlate in their extent [72]. This allows to calculate the unbiased CEST effect, the so-called *downfield-rNOE-suppressed AREX* (dnsAREX), by simple weighted subtraction of the downfield effect as follows:

$$dnsAREX(\Delta\omega) = AREX(\Delta\omega) - r_{NOE} \cdot AREX(-\Delta\omega). \tag{7.4}$$

The correlation factor was determined for the human brain to be $r_{NOE} \approx 0.2$ [72]. An application of $dnsAREX$ with this factor to the data of volunteer #1 results in practically no change in pH ($pH = 6.96 \pm 0.15$) while the concentration of creatine drops significantly ($c_{Cr} = (55.9 \pm 10.1)$ mM). Even though the used factor may not be precise due to the differently composed tissues of brain and muscle, this correction probably allows a more accurate determination of the metabolite concentration. A correct identification of $r_{NOE,muscle}$ requires tissue at different pH values over a wide range, excluding a direct in vivo measurement. However, in a first step tissue homogenates of animal muscle, i.e. frog leg muscle, could be extracted and measured as shown in other studies [152].

After all it could also be argued whether the CEST signal itself arises from exchanging protons within the cell or from the extracellular space. While any signals caused by proteins, containing for example arginine, are from the intracellular space [12], metabolites like creatine are also present outside the cell. It is believed that these two areas differ in pH [50]. So it is possible that the determined pH value and concentration by the extended Ω-plot method are average values over both compartments.This could be investigated by using the frequency separation between the phosphocreatine (PCr) and anorganic phosphate (Pi) resonance [153], which allows to determine the intracellular pH by ^{31}P spectroscopic imaging with good precision [154].

Differences between muscle groups

The physiological parameters determined by the Ω-plot method enable the investigation of differences between muscle regions. This small, but distinct heterogeneity is particularly visible and reproducible between the pH values of the *musculus gastrocnemius* and *musculus soleus* (figure 6.17 and table 6.3). These disparities could reflect different muscle fiber compositions or the difference between oxidative and glycolytic energy metabolism [154]. For more precise statements, follow-up experiments and a comparison to other methods like spectroscopy or biopsy are needed.

7.3.3. Impact of exercise on the quantitative values

With the help of the extended Ω-plot method it is possible to determine absolute changes in pH and metabolite concentration in vivo. Using a MR-compatible foot pedal the volunteer performed a consistent mild exercise, i.e. plantar and dorsi flexion, during the saturation phase and hold still during the imaging part. The break was primarily introduced to minimize movement artifacts during imaging readout [155].

The *musculus soleus* is hardly affected by the selected exercise. On the one hand this muscle is mainly responsible for holding a standing posture [51] and on the other hand primarily consists of slow-twitch fibers ($\geq 70\%$) [50,156]. They are characterized by an aerobic metabolism and in the case of mild exercise no excessive creatine or H^+ ions should be produced. In the *musculus tibialis anterior* the pH did not change while the creatine concentration increased strongly. The pause in the exercise could ensure a constant activity of the creatine-kinase (CK) for energy supply, as there is always time for regeneration and the cell has no need to activate the glycolysis [50]. However, the resulting maps (figure 6.21) show many corrupted pixels in this region. Especially there a movement of the calf can be observed in the single offset images so that the observed effects are most likely motion artifacts.

The *musculus gastrocnemius* shows different reaction within itself. While in the more lateral part the pH stays constant and c_{Cr} increases, the dorsal part exhibits exactly the opposite – an increased pH and constant c_{Cr}. As already stated, the energy demand for mild exercise in combination with the pause could be so low that the CK-reaction provides sufficient ATP [50] to supply the muscle. Hence the creatine concentration rises and the hydrogen ion concentration equalizes between ATP hydrolysis and CK-reaction. This, however, can not explain the behavior in the dorsal part. This region could be more strained by the exercise so that the CK-reaction is no longer sufficient as an energy supplier. In the case of a weak, but steady energy turnover the glycolysis could provide the needed energy. Anorganic phosphate P_i released from ATP might buffer the hydrogen ions resulting in a slightly increased pH.

Also, a different fiber type distribution could be responsible for the disparity. Even though the *musculus gastrocnemius* consists mainly out of fast-twitch fibers ($> 60\%$) [157], the specific prevalence of slow-twitch fibers in the more lateral part could be increased. Since the two fibers have different metabolic behaviors, they react differently to fatigue [158]. The slow-twitch muscle fibers gain energy mainly through aerobic and the fast-twitch fibers through anaerobic metabolism. However, this explanation is speculative and must be verified in follow up experiments.

There are many arteries and veins in the human calf. Blood exhibits a strong and broad CEST effect upfield from water [159]. This explains pixels and regions where the Ω-plot fit failed and resulted in exclusion. In addition to large vessels the muscle is traversed by capillaries. During exercise these capillaries are supplied with more blood to meet the increased oxygen consumption. Since the pH value of blood is higher than that of the surrounding tissue [140], perfusion could lead to an overestimation. However, *Kogan et al.* recently showed that the creatine CEST effect is not affected by perfusion in the case of mild exercise [145]. If pathologies are examined, the effect of perfusion, however, cannot be excluded as a plausible cause.

Even though the measured absolute creatine concentration is probably contaminated by other effects (section 7.3.2), all changes of the value c_{Cr} under exercise should result from the CK reaction. The increase of about $\sim 10\,\text{mM}$ agrees well with other published values for mild exercise, i.e. $(13.8 \pm 6.8)\,\text{mM}$ by *Rerich et al.* [15] or $(11.0 \pm 5.8)\,\text{mM}$ by *Kogan et al.* [14]. This allows to conclude that, even if no absolute statements can be made, changes in the creatine concentration can be investigated.

7.3.4. Further (clinical) applications in vivo – an outlook

The constraints of the extended Ω-plot method and the comparatively long measurement time set limits to its clinical applicability in vivo. Nevertheless, the measurement of pH and concentration in vivo is desirable in many diseases and also in basic research. As already addressed, the creatine concentration correlates with the energy metabolism of healthy and pathological tissue in muscle [14,160] as well as in the brain [146,147]. Also, the measurement of the glycosaminogycan (GAG) concentration is important in connection with joint diseases, as a loss in cartilage is typically an initiating event of osteoarthritis [20]. Another widespread pathology related to GAG is inter-vertebral disk degeneration, in which the Ω-plot method has recently been used to study inter-vertebral discs in a porcine model [134].

Besides diseases of the musculoskeletal system these maps could yield information on the pathophysiology of stroke [161] or oncologic diseases such as brain tumors [162–164]. The applicability of the extended Ω-plot method to the brain is demonstrated by utilizing an old data set of *Windschuh et al.* obtained at 7 T [103]. The Z-spectra, AREX-spectra, Ω-plot in a ROI, and resulting pixel-wise parameter maps are shown in figure 7.3. The expected pH homogeneity and difference in metabolite concentration between white and gray matter is seen [165]. Note, that the pH is around 7 and the creatine concentration is probably elevated due to the presence of proteins containing arginine and the rNOE upfield from water.

Next to endogenous agents, the quantification of exchange rates of exogenous CEST agents is of interest [22,30,78,166,167]. These, compared to conventional contrast agents, e.g. gadolinium compounds, exhibit the possibility to switch the contrast on and off [166]. By adapting the chemical structure of the compound the exchange rate can be matched to optimal saturation parameter, which may result in an improved contrast [168]. Until now the determination of the exchange rate was only possible for cw saturation which is not applicable in a clinical setup. Altogether, the extended Ω-plot method could help to characterize chemical compounds for clinical and basic research.

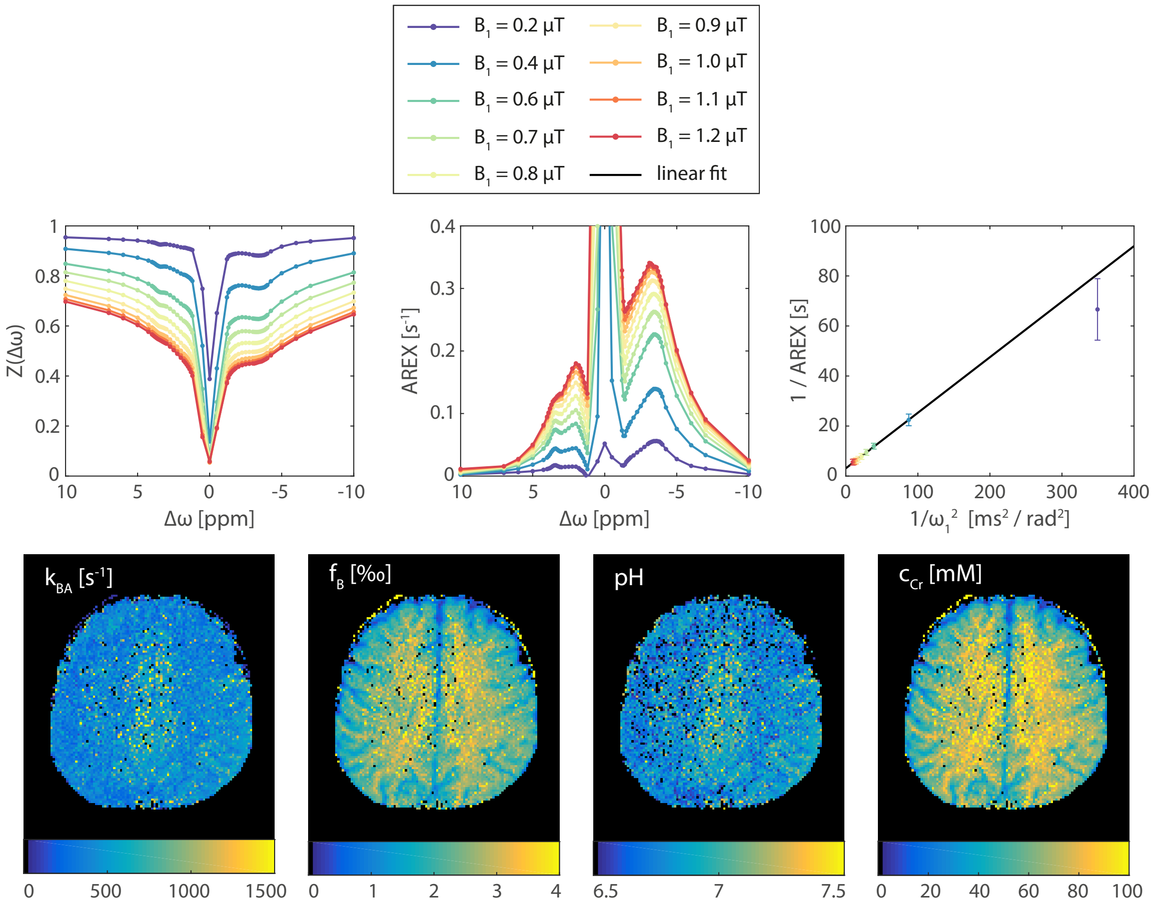

Figure 7.3.: Z-spectra, AREX-spectra, Ω-plot in a ROI, and pixel-wise parameter maps in the human brain. The data was kindly provided by *Windschuh et al.* [103].

One major drawback of the proposed method is the long measurement time. This results from the imaging readout and from the required steady state. The acquisition could be accelerated using more advanced techniques, i.e. echo-planar readouts [169, 170], balanced steady-state free precession (bSSFP) sequences [171, 172], or parallel imaging [130–133]. Additionally, to increase the clinical significance a three dimensional readout is needed. To avoid the very long saturation times t_{sat} for AREX, *Zaiss* proposed an alternative method, which uses the transient state. Performing two optimized measurements with shortened t_{sat} enables the determination of AREX (Appendix A.8. in [28]).

8. Conclusion

The goal of this study was to enable the quantitative examination of Chemical Exchange Saturation Transfer (CEST) effects in a clinical setup. For this purpose the simultaneous determination of the exchange rate k_{BA} of exchanging protons and their relative concentration f_B in the case of pulsed saturation is sought. In the process, this allows to analyze the pH and absolute creatine concentrations in vitro and in the human calf muscle for resting condition as well as exercise.

To describe pulsed CEST experiments analytically an existing interleaved-saturation and relaxation model was extended for time-dependent saturation pulses. The integration of the longitudinal relaxation rate in the rotating frame $R_{1\rho}(\omega_1(t))$ as a function of the pulse shape was performed entirely for a Gaussian-like function. This analytical calculation ultimately resulted in two form factors c_1 and c_2 which are sufficient to adjust the cw theory for Gaussian-shaped saturation pulses. Later on it was shown, that the description by these form factors is universal for every shaped pulse, although the actual values differ between the pulses. Hence, the behavior of the exchange-dependent relaxation rate R_{ex} in the case of pulsed saturation can be fully understood. Consequently, the exchange rate dependent performance of different pulse shapes can be tested. The accuracy of the analytical derived form factors can be improved by utilizing a measurement with continuous wave saturation. Comparing the proposed model to numerical Bloch-McConnell simulations demonstrates the validity in the intermediate- and fast-exchange regime.
Employing the proposed analytical description of CEST with its form factors to the Ω-plot method allowed an improved estimation of the exchange rate k_{BA} and the relative concentration f_B in the case of pulsed saturation. In vitro experiments were performed on a 7 T whole body scanner. In this clinical setup the characterization of the exchanging guanidinium group of creatine was performed. As derived from the apparent exchange-dependent relaxation rate AREX this extended Ω-plot method enabled a water relaxation parameter independent determination of k_{BA} and f_B. The exponential relation between the exchange rate and pH and linear dependency of the relative concentration from the creatine abundance could be verified. The quantitative values determined for saturation using shapes pulses are in good agreement with results from cw experiments and published values. Since all in vitro experiments point to four exchanging protons for creatine the zwitterionic structure can be confirmed as the dominant form between pH 6 and 7.5.
The obtained knowledge about the form factors enabled quantitative investigations in vivo. The human calf was chosen as the examined biological system, since creatine is an important part of the energy metabolism in muscle. Different Lorentzian fit models were probed regarding an adequate isolation of the CEST effect. It was found that a six-pool Lorentzian fit model, which included the direct water saturation, semi-solid MT, rNOE and chemical exchange effects at $\Delta\omega = 1.9$, 2.7 and 3.5 ppm, performed best. The resulting exchange rate and concentration maps depicted slight differences between the various muscle groups. Though, the values were homogenous within these different regions. The assumption that the relations between physical and physiological parameters, which were determined for creatine model solutions, are also applicable in vivo allowed the determination of pH and absolute concentration. While the pH was around 7 the Ω-plot analysis revealed other contributions than

creatine at $\Delta\omega_B = 1.9\,\text{ppm}$. The rNOE effect of aliphatic protons and the guanidinium group of the amino acid arginine are the most prominent additional contributions.
pH and concentration changes could be observed during mild exercise. Differences between the muscles, i.e. *musculus gastrocnemius* and *musculus soleus*, and within the individual muscles can be seen.

Altogether, the proposed Ω-plot approach represents a major step towards quantitative CEST studies in vivo. The application might provide new insights in the energy metabolism and pathologies like stroke or cancer on a physiological level.

Appendix

A. Weak-saturation-pulse or large-shift limit

In a *weak-saturation* or *large-(frequency-)shifts* limit the direct water saturation can be neglected. In this case only the pool B is directly affected by the rf saturation. In the Bloch-McConnell (BM) equations (4.4)-(4.9) the following terms can be ignored: $\Delta\omega_A M_{yA}$, $\Delta\omega_A M_{xA}$, $\omega_1 M_{zA}$ und $\omega_1 M_{yA}$. Assuming additionally a steady state condition ($\frac{d}{dt}M = 0$) yields form the equations (4.4)-(4.6) the following terms for the magnetization component of the water pool:

$$M_{xA} = \frac{k_{BA}}{R_{2A} + k_{AB}} \cdot M_{xB} \tag{A.1}$$

$$M_{yA} = \frac{k_{BA}}{R_{2A} + k_{AB}} \cdot M_{yB} \tag{A.2}$$

$$M_{zA} = \frac{k_{BA}}{R_{1A} + k_{AB}} \cdot M_{zB} + \frac{R_{1A}}{R_{1A} + k_{AB}} \cdot M_{zA}^0 \tag{A.3}$$

Substitution in (4.7) and (4.8) yields:

$$0 = -\,\Delta\omega_B M_{yB} - R_{2B} M_{xB} - k_{BA} M_{xB} + k_{AB} \cdot \frac{k_{BA}}{R_{2B} + k_{AB}} \cdot M_{xB} \tag{A.4}$$

$$0 = +\,\Delta\omega_B M_{xB} - R_{2B} M_{yB} - \omega_1 M_{zB} - k_{BA} M_{yB} + k_{AB} \cdot \frac{k_{BA}}{R_{2B} + k_{AB}} \cdot M_{yB} \tag{A.5}$$

Using

$$p = R_{2B} + \frac{R_{2A} k_{BA}}{R_{2A} + k_{AB}} \tag{A.6}$$

$$q = R_{1B} + \frac{R_{1A} k_{BA}}{R_{1A} + k_{AB}} \tag{A.7}$$

simplifies the equations (A.4) and (A.5) to

$$M_{xB} = \frac{-\Delta\omega_B M_{yB}}{p} \tag{A.8}$$

$$M_{yB} \cdot p = +\Delta\omega_B M_{xB} - \omega_1 M_{zB}. \tag{A.9}$$

This allows the derivation of M_{yB} as follows

$$M_{yB} = \frac{-\,\omega_1}{p + \frac{\Delta\omega_B^2}{p}} M_{zB}. \tag{A.10}$$

Inserting equation (A.10) into (4.9) yields for M_{zB}

$$M_{zB} = \frac{R_{1B}M_{zB}^0 + k_{AB}M_{zA}}{\omega_1 \frac{\omega_1}{p+\frac{\Delta\omega_B^2}{p}} + R_{1B} + k_{BA}} \tag{A.11}$$

This is the steady state magnetization of pool B for any given pool A. Substitution of M_{zA} from (A.3) yields

$$M_{zB} = \frac{R_{1B}M_{zB}^0 + k_{AB}\left(\frac{k_{BA}}{R_{1A}+k_{AB}} \cdot M_{zB} + \frac{R_{1A}}{R_{1A}+k_{AB}} \cdot M_{zA}^0\right)}{\omega_1 \frac{\omega_1}{p+\frac{\Delta\omega_B^2}{p}} + R_{1B} + k_{BA}} \tag{A.12}$$

$$\Leftrightarrow \qquad M_{zB} = \frac{R_{1B}M_{zB}^0 + R_{1A}\frac{k_{AB}}{R_{1A}+k_{AB}} \cdot M_{zA}^0}{\frac{\omega_1^2}{p+\frac{\Delta\omega_B^2}{p}} + q} \tag{A.13}$$

Using the relations $\frac{M_{zA}^0}{M_{zB}^0} = \frac{k_{BA}}{k_{AB}}$ leads to:

$$\frac{M_{zB}}{M_{zB}^0} = \frac{R_{1B} + R_{1A}\frac{k_{BA}}{R_{1A}+k_{AB}}}{\frac{\omega_1^2}{p+\frac{\Delta\omega_B^2}{p}} + q} \ . \tag{A.14}$$

Combining equations (A.14) and (A.3) yields:

$$Z = \frac{M_{zA}}{M_{zA}^0} = 1 - \frac{k_{AB}}{R_{1A} + k_{AB}} \cdot \underbrace{\frac{\omega_1^2}{\omega_1^2 + pq + \frac{\Delta\omega_B^2 \cdot q}{p}}}_{\alpha} \tag{A.15}$$

This equation describes the Z value in the *weak-saturation* or *large-shift* limit. The labeling efficiency α [88] has the shape of a Lorentzian function [25]. By switching all indices from A to B and vice versa the formula for the direct water saturation can be derived.

B. Labeling efficiency in general

Derived by *Sun et al.* [25] the labeling efficiency α is given by

$$\alpha(\Delta\omega, \omega_1) = \frac{R_{ex}(\Delta\omega, \omega_1)}{f_B k_{BA}} \tag{B.16}$$

neglecting the R_{2B} term yields

$$\alpha(\Delta\omega, \omega_1) = \frac{\frac{\delta\omega^2}{\omega_1+\delta\omega^2}k_{BA} + R_{2B}}{k_{BA} + R_{2B}} \cdot \frac{\omega_1^2}{\omega_1^2 + k_{BA}(k_{BA} + R_{2B})} \tag{B.17}$$

$$\overset{\text{LS}}{=} \frac{\omega_1^2}{\omega_1^2 + k_{BA}(k_{BA} + R_{2B})} \tag{B.18}$$

C. Derivation of AREX in the pulsed case

This calculations were published in the Journal *NMR in Biomedicine* [104].

The normalized steady-state magnetization in the case of pulsed pre-saturation is given by

$$Z_{pulsed}^{SS} = \frac{\left(1 - \mathrm{e}^{-R_{1A}t_d}\right) - \frac{\cos\Theta R_{1A}}{R_{1\rho}(\Delta\omega)}\left(1 - \mathrm{e}^{R_{1\rho}(\Delta\omega)t_p}\right)}{\mathrm{e}^{R_{1\rho}(\Delta\omega)t_p} - \mathrm{e}^{-R_{1A}t_d}} \tag{C.19}$$

using the assumption $exp(x) \approx 1 + x$ leads to

$$Z_{pulsed}^{SS} \approx \frac{(1 - (1 - R_{1A}t_d)) - \frac{\cos\Theta R_{1A}}{R_{1\rho}(\Delta\omega)}(1 - (1 + R_{1\rho}(\Delta\omega)t_p))}{(1 - R_{1\rho}(\Delta\omega)t_p) - (1 + R_{1A}t_d)} \tag{C.20}$$

$$\approx \frac{R_{1A}\left(\frac{t_d}{t_p} + \cos\Theta\right)}{R_{1\rho} + R_{1A}\frac{t_d}{t_p}} \tag{C.21}$$

Introducing the duty cycle $DC = t_p/t_p + t_d$ results in

$$Z_{pulsed}^{SS} \approx \frac{R_{1A}\left(1 - DC + DC \cdot \cos\Theta\right)}{R_{1\rho}DC + R_{1A}(1 - DC)} \tag{C.22}$$

Considering only small flip angles Θ, the cosine term will be approximately one, and with

$$MTR_{Rex} = \frac{1}{Z_{lab}} - \frac{1}{Z_{ref}} \tag{C.23}$$

yields

$$MTR_{Rex} = \frac{1}{\frac{R_{1A}}{R_{1\rho,lab}DC + R_{1A}(1-DC)}} - \frac{1}{\frac{R_{1A}}{R_{1\rho,ref}DC + R_{1A}(1-DC)}} \tag{C.24}$$

$$= \frac{DC\left(R_{1\rho,lab} - R_{1\rho,ref}\right)}{R_{1A}} \tag{C.25}$$

Using $R_{1\rho,lab} = R_{eff} + R_{ex}$ and $R_{1\rho,ref} = R_{eff}$, it follows that

$$MTR_{Rex} = \frac{R_{ex}DC}{R_{1A}} \tag{C.26}$$

Multiplication by R_{1A} yields the definition of AREX as defined in [28]:

$$AREX = MTR_{Rex}R_{1A} = R_{ex}DC. \tag{C.27}$$

D. Derivation of the time-dependent $R_{1\rho}$ for Gaussian-shaped pulses

This calculations were published in the Journal *NMR in Biomedicine* [104].

For shaped pulses, a time dependent $R_{1\rho}$ has to be considered:

$$R_{1\rho}(\omega(t)) = R_{eff}(\omega(t)) + R_{ex}(\omega(t)) \tag{D.28}$$

Integration as a function of time leads to an average $\overline{R_{1\rho}}$:

$$\overline{R_{1\rho}}(\omega(t)) = \frac{1}{t_p}\int_0^{t_p} R_{eff}(\omega(t))\mathrm{d}t + \frac{1}{t_p}\int_0^{t_p} R_{ex}(\omega(t))\mathrm{d}t \tag{D.29}$$

$$\begin{aligned} &= \frac{1}{t_p}\int_0^{t_p}\left[R_{1A} + (R_{2A}-R_{1A})\frac{\omega_1^2(t)}{\omega_1^2(t)+\Delta\omega}\right]\mathrm{d}t \\ &+ \frac{1}{t_p}\int_0^{t_p}\left[f_B k_{BA}\frac{\omega_1^2(t)}{\omega_1^2(t)+k_{BA}(k_{BA}+R_{2B})}\right]\mathrm{d}t \end{aligned} \tag{D.30}$$

Rearranging yields

$$\begin{aligned} \overline{R_{1\rho}}(\omega(t)) = &R_{1A} + \frac{(R_{2A}-R_{1A})}{t_p}\int_0^{t_p}\frac{\omega_1^2(t)}{\Delta\omega^2}\cdot\frac{1}{\frac{\omega_1^2(t)}{\Delta\omega^2}+1}\mathrm{d}t \\ &+ \frac{f_B k_{BA}}{t_p}\int_0^{t_p}\frac{\omega_1^2(t)}{k_{BA}(k_{BA}+R_{2B})}\cdot\frac{1}{\frac{\omega_1^2(t)}{k_{BA}(k_{BA}+R_{2B})}+1}\mathrm{d}t \end{aligned} \tag{D.31}$$

Substitution with $x^2 = \frac{1}{\Delta\omega^2}$ and $y^2 = \frac{1}{k_{BA}(k_{BA}+R_{2B})}$ leads to

$$\begin{aligned} \overline{R_{1\rho}}(\omega(t)) = &R_{1A} + \frac{(R_{2A}-R_{1A})}{t_p}\int_0^{t_p}\frac{\omega_1^2(t)}{\Delta\omega^2}\cdot\frac{1}{\frac{\omega_1^2(t)}{\Delta\omega^2}+1}\mathrm{d}t \\ &+ \frac{f_B k_{BA}}{t_p}\int_0^{t_p}\frac{\omega_1^2(t)}{k_{BA}(k_{BA}+R_{2B})}\cdot\frac{1}{\frac{\omega_1^2(t)}{k_{BA}(k_{BA}+R_{2B})}+1}\mathrm{d}t \end{aligned} \tag{D.32}$$

This integral can be solved numerically. However, in the following an analytical approximation is shown.

D.1. Analytical integration

Due to the same form of the integrals in Equation , calculations can be performed for x^2 and transferred to y^2. Employing the power-series of $1/(x^2+1)$, the integral can be rewritten as

$$\frac{1}{t_p}\int_0^{t_p}\omega_1^2(t)x^2\cdot\frac{1}{\omega_1^2(t)+1}\mathrm{d}t = \frac{1}{t_p}\int_0^{t_p}\omega_1^2(t)x^2\cdot\left(\sum_{l=0}^{\infty}\left(-\omega_1^2(t)x^2\right)^l\right) \tag{D.33}$$

Assuming a Gaussian-shaped pulse defined by

$$\omega_1(t) = \omega_1 t_p\frac{1}{\sigma\sqrt{2\pi}}\cdot \mathrm{e}^{-\frac{\left(t-\frac{t_p}{2}\right)^2}{2\sigma^2}} \tag{D.34}$$

with

$$\int_0^{t_p} \frac{\omega_1(t)}{t_p} \mathrm{d}t = \omega_1 \tag{D.35}$$

and the nth moments of ω_1,

$$\int \omega_1^n \mathrm{d}t = \int \left(\omega_1 t_p \frac{1}{\sigma\sqrt{2\pi}} \cdot \mathrm{e}^{-\frac{\left(t-\frac{t_p}{2}\right)^2}{2\sigma^2}} \right)^2 = (\omega_1 t_p)^n \left(\frac{1}{\sigma\sqrt{2\pi}} \right)^{n-1} \cdot \frac{1}{\sqrt{n}} \tag{D.36}$$

every single term of the infinite series ca be analytically integrated and yields

$$\frac{1}{t_p} \int_0^{t_p} \left(-\sum_{l=1}^{\infty} \left(-\omega_1^2(t) x^2\right)^l \right) \mathrm{d}t = -\frac{1}{t_p} \sum_{l=1}^{\infty} \left(-\omega_1^2 t_p^2 x^2\right)^l \left(\frac{1}{\sigma\sqrt{2\pi}} \right)^{2l-1} \cdot \frac{1}{\sqrt{2l}} \tag{D.37}$$

$$:= \Psi\left(-\omega_1^2(t) x^2, \sigma, t_p\right) \tag{D.38}$$

The function $\Psi\left(X, \sigma, t_p\right)$ is defined by the power series as given in Appendix D.2. By inserting equation (D.37) into equation (D.32) an analytic expression of $\overline{R_{1\rho}}$ can be derived:

$$\overline{R_{1\rho}} = R_{1A} + \left(R_{2A} - R_{1A}\right) \cdot \Psi\left(-\omega_1^2(t) x^2, \sigma, t_p\right) + f_B k_{BA} \cdot \Psi\left(-\omega_1^2(t) y^2, \sigma, t_p\right) \tag{D.39}$$

However, the linearity of the Ω-plots in the case of pulsed pre-saturation (figure 6.11) indicated that R_ex and thus $\Psi\left(X, \sigma, t_p\right)$ must have the shape $X^2/\left(1+X^2\right)$. This is the case if $X < 1$, as given in Appendix D.2. Then equation (D.39) simplifies to

$$\overline{R_{1\rho}} \approx R_{1A} + \left(R_{2A} - R_{1A}\right) \cdot c_1 \frac{\omega_1^2 \cdot x^2}{\omega_1^2 \cdot x^2 + c_2^2} + f_B k_{BA} \cdot c_1 \frac{\omega_1^2 \cdot y^2}{\omega_1^2 \cdot y^2 + c_2^2}. \tag{D.40}$$

With the form factors $c_1 = \sqrt{2\pi}$ and $c_2 = c_1 \cdot \sqrt[4]{2} = \sqrt{2\pi}\ \sigma / t_p \cdot \sqrt[4]{2}$, substitution of $x^2 = \frac{1}{\Delta\omega^2}$ and $y^2 = \frac{1}{k_{BA}(k_B A + R_{2B})}$ yields

$$\overline{R_{1\rho}} \approx R_{1A} + \left(R_{2A} - R_{1A}\right) \cdot c_1 \frac{\omega_1^2}{\omega_1^2 + \omega^2 \cdot c_2^2} + f_B k_{BA} \cdot c_1 \frac{\omega_1^2}{\omega_1^2 + k_{BA}\left(k_{BA} + R_{2B}\right) \cdot c_2^2}. \tag{D.41}$$

Thus, AREX in the case of a pulsed pre-saturation is modified to

$$AREX_{pulsed} = DC \cdot f_B k_{BA} \cdot c_1 \frac{\omega_1^2}{\omega_1^2 + k_{BA}\left(k_{BA} + R_{2B}\right) + \cdot c_2^2} \tag{D.42}$$

which yields a linear equation of the form $1/AREX = m \cdot 1/\omega_1^2 + n$:

$$\frac{1}{AREX_{pulsed}} = \frac{\left(k_{BA} + R_{2B}\right) c_2^2}{f_B \cdot DC \cdot c_1} \cdot \frac{1}{\omega_1^2} + \frac{1}{f_B k_{BA} \cdot DC \cdot c_1} \tag{D.43}$$

Determination of the slope m and y-intersection n enables quatification of f_B and k_{BA}in the case of Gaussian-shaped saturation:

$$f_B^{shaped-pulses} = \frac{1}{c_1 \cdot DC \cdot n \cdot \left(-\frac{R_{2B}}{2} + \sqrt{\frac{R_{2B}^2}{4} + \frac{m}{n \cdot c_2^2}}\right)} \tag{D.44}$$

$$k_{BA}^{shaped-pulses} = -\frac{R_{2B}}{2} + \sqrt{\frac{R_{2B}^2}{4} + \frac{m}{n \cdot c_2^2}} \tag{D.45}$$

D.2. The power series $\Psi\left(X, \sigma, t_p\right)$

The found power series $\Psi\left(X, \sigma, t_p\right)$ is generally defined as

$$\Psi\left(X, \sigma, t_p\right) = -\frac{1}{t_p} \sum_{l=1}^{\infty} \left(-\omega_1^2 t_p^2 x^2\right)^l \left(\frac{1}{\sigma\sqrt{2\pi}}\right)^{2l-1} \cdot \frac{1}{\sqrt{2l}} \tag{D.46}$$

If $X < 1$, this serien can be transformed to the geometric series using the approximation $\sqrt{2l} \approx \sqrt{2}^l$. This yields a geometric series $G\left(X, \sigma, t_p\right)$, which agrees with $\Psi\left(X, \sigma, t_p\right)$ to the second order:

$$\Psi\left(X, \sigma, t_p\right) \approx G\left(X, \sigma, t_p\right) = -\frac{\sigma\sqrt{2\pi}}{t_p} \cdot \sum_{l=1}^{\infty} \left(X \left(\frac{t_p}{\sigma\sqrt{2\pi}}\right)^2 \cdot \frac{1}{\sqrt{2}}\right)^l \tag{D.47}$$

$$= -\frac{\sigma\sqrt{2\pi}}{t_p} \cdot \sum_{l=1}^{\infty} (q)^l \tag{D.48}$$

This yields a closed form if $q < 1$:

$$G\left(X, \sigma, t_p\right) = -\frac{\sigma\sqrt{2\pi}}{t_p} \cdot \frac{q}{1-q} \tag{D.49}$$

$$= -\frac{\sigma\sqrt{2\pi}}{t_p} \cdot \frac{X\left(\frac{t_p}{\sigma\sqrt{2\pi}}\right)^2 \cdot \frac{1}{\sqrt{2}}}{1 - X\left(\frac{t_p}{\sigma\sqrt{2\pi}}\right)^2 \cdot \frac{1}{\sqrt{2}}} \tag{D.50}$$

Rearranging leads to

$$G\left(X, \sigma, t_p\right) = -\frac{\sigma\sqrt{2\pi}}{t_p} \cdot \frac{X}{X - \left(\frac{t_p}{\sigma\sqrt{2\pi}}\right)^2 \cdot \sqrt{2}} \tag{D.51}$$

Introducing the form factors $c_1 = \sqrt{2\pi}$ and $c_2 = c_1 \cdot \sqrt[4]{2} = \sqrt{2\pi}\ \sigma/t_p \cdot \sqrt[4]{2}$ yields

$$\Psi\left(X, \sigma, t_p\right) \approx G\left(X, \sigma, t_p\right) = c_1 \frac{X}{X - c_2^2} \tag{D.52}$$

D.3. R_{ex} in the large-shift limit

The calculations in the previous section were only valid in the case of on-resonant irradiation. In general the exchange-dependent relaxation rate R_{ex} is given by

$$\begin{aligned} R_{ex} = f_B k_{BA} \frac{\delta\omega_B^2}{\omega_1^2 + \Delta\omega^2} \cdot \frac{\omega_1^2}{\Gamma^2/4 + \Delta\omega_B^2} + \\ f_B R_{2B} \frac{\omega_1^2}{\Gamma^2/4 + \Delta\omega_B^2} + f_B k_{BA} sin^2\Theta \frac{R_{2B}\left(R_{2B} + k_{BA}\right)}{\Gamma^2/4 + \Delta\omega_B^2} \end{aligned} \tag{D.53}$$

In the large-shift-limit ($\delta\omega_B \to \infty$) the exchange-dependent relaxation rate R_{ex} is given by [28]:

$$R_{ex,LS} = \frac{R_{ex,LS}^{lab} \cdot \Gamma^2/4}{\Gamma^2/4 + \Delta\omega^2} \tag{D.54}$$

$$\Leftrightarrow R_{ex,LS} = \frac{f_B k_{BA} \frac{\omega_1^2}{\omega_1^2 + k_{BA}(k_{BA} + R_{2B})} \cdot \left(\frac{R_{2B} + k_{BA}}{k_{BA}}\omega_1^2 + \left(R_{2B} + k_{BA}\right)^2\right)}{\left(\frac{R_{2B} + k_{BA}}{k_{BA}}\omega_1^2 + \left(R_{2B} + k_{BA}\right)^2\right) + \Delta\omega_B^2} \tag{D.55}$$

$$\Leftrightarrow R_{ex,LS} = \frac{f_B k_{BA} \frac{\omega_1^2}{\omega_1^2 + k_{BA}(k_{BA} + R_{2B})} \cdot \left(\frac{R_{2B} + k_{BA}}{k_{BA}}\right)\left(\omega_1^2 + k_{BA}\left(R_{2B} + k_{BA}\right)\right)}{\frac{R_{2B} + k_{BA}}{k_{BA}}\left(\omega_1^2 + k_B\left(R_{2B} + k_{BA}\right) + \frac{k_{BA}}{R_{2B} + k_{BA}}\Delta\omega_B^2\right)} \tag{D.56}$$

$$\Leftrightarrow R_{ex,LS} = \frac{f_B k_{BA} \frac{\omega_1^2}{\omega_1^2 + k_{BA}(k_{BA} + R_{2B})} \cdot \left(\omega_1^2 + k_{BA}\left(R_{2B} + k_{BA}\right)\right)}{\omega_1^2 + k_B\left(R_{2B} + k_{BA}\right) + \frac{k_{BA}}{R_{2B} + k_{BA}}\Delta\omega_B^2} \tag{D.57}$$

$$\Leftrightarrow R_{ex,LS} = \frac{f_B k_{BA} \omega_1^2}{\omega_1^2 + k_B\left(R_{2B} + k_{BA}\right) + \frac{k_{BA}}{R_{2B} + k_{BA}}\Delta\omega_B^2} \tag{D.58}$$

The mean R_{ex} can than be derived by

$$\overline{R}_{ex} = \frac{\int_{t=0}^{t_p} R_{ex}(\omega_1(t))dt}{t_p} = \frac{f_B k_{BA} \int_{t=0}^{t_p} \frac{\omega_1^2}{\omega_1^2 + k_{BA}(k_{BA} + R_{2B}) + \frac{k_{BA}}{k_{BA} + R_{2B}}\Delta\omega_B^2} dt}{t_p} \tag{D.59}$$

with $K = \left(k_{BA}\left(k_{BA} + R_{2B}\right) + \frac{k_{BA}}{k_{BA} + R_{2B}}\Delta\omega_B^2\right)$ follows

$$\overline{R}_{ex} = \frac{\int_{t=0}^{t_p} R_{ex}(\omega_1(t))dt}{t_p} = \frac{f_B k_{BA} \int_{t=0}^{t_p} \frac{\omega_1^2}{\omega_1^2 + K} dt}{t_p} \tag{D.60}$$

D.3.1. Derivation of the integral

The integral so solve is given by

$$\int \frac{\omega_1^2(t)}{\omega_1^2(t) + K} dt = \int \frac{\omega_1^2(t)}{K} \frac{1}{\frac{\omega_1^2(t)}{K} + 1} dt \tag{D.61}$$

Assuming that $\omega_1^2 \ll k_{BA}(k_{BA} + R_{2B})$, the second term can be written as a sum:

$$\int \frac{\omega_1^2(t)}{K} \frac{1}{\frac{\omega_1^2(t)}{K} + 1} dt \overset{\omega_1 \ll k_{BA}}{\overbrace{=}} \int \frac{\omega_1^2(t)}{K} \left(1 - \frac{\omega_1^2(t)}{K} + \left(\frac{\omega_1^2(t)}{K}\right)^2 - \left(\frac{\omega_1^2(t)}{K}\right)^3 + ...\right) dt \tag{D.62}$$

now the derived intergral of the Gaussian-shaped pulse D.1 can be inserted

$$\int \left[\frac{\omega_1^2(t)}{K} \left(1 - \frac{\omega_1^2(t)}{K} + \left(\frac{\omega_1^2(t)}{K}\right)^2 - \left(\frac{\omega_1^2(t)}{K}\right)^3 + ...\right)\right] dt \tag{D.63}$$

$$= \int \left[\frac{\omega_1^2(t)}{K} - \left(\frac{\omega_1^2(t)}{K}\right)^2 + \left(\frac{\omega_1^2(t)}{K}\right)^3 - \left(\frac{\omega_1^2(t)}{K}\right)^4 + ...\right] dt \tag{D.64}$$

$$= \left(\frac{(\omega_1 \cdot t_p)^2}{K^1} \cdot \left(\frac{1}{\sigma\sqrt{2\pi}}\right) \frac{1}{\sqrt{2}}\right) - \left(\frac{(\omega_1 \cdot t_p)^4}{K^2} \cdot \left(\frac{1}{\sigma\sqrt{2\pi}}\right)^3 \frac{1}{\sqrt{4}}\right) + \left(\frac{(\omega_1 \cdot t_p)^6}{K^3} \cdot \left(\frac{1}{\sigma\sqrt{2\pi}}\right)^5 \frac{1}{\sqrt{6}}\right) - \left(\frac{(\omega_1 \cdot t_p)^8}{K^4} \cdot \left(\frac{1}{\sigma\sqrt{2\pi}}\right)^7 \frac{1}{\sqrt{8}} -\right) + ... \tag{D.65}$$

$$= \left(\frac{\omega_1^2 \cdot t_p^2}{K} \cdot \left(\frac{1}{\sigma\sqrt{2\pi}}\right) \frac{1}{\sqrt{2}}\right) - \left(\frac{\left(\omega_1^2 \cdot t_p^2\right)^2}{K^2} \cdot \left(\frac{1}{\sigma\sqrt{2\pi}}\right)^3 \frac{1}{\sqrt{4}}\right) + \left(\frac{\left(\omega_1^2 \cdot t_p^2\right)^3}{K^3} \cdot \left(\frac{1}{\sigma\sqrt{2\pi}}\right)^5 \frac{1}{\sqrt{6}}\right) - \left(\frac{\left(\omega_1^2 \cdot t_p^2\right)^4}{K^4} \cdot \left(\frac{1}{\sigma\sqrt{2\pi}}\right)^7 \frac{1}{\sqrt{8}} -\right) + ... \tag{D.66}$$

$$= \sigma\sqrt{2\pi} \cdot \left(\left(\frac{\omega_1^2 \cdot t_p^2}{K}\right) \left(\frac{1}{\sigma\sqrt{2\pi}}\right)^2 \cdot \frac{1}{\sqrt{2}} - \left(\frac{\omega_1^2 \cdot t_p^2}{K}\right)^2 \cdot \left(\frac{1}{\sigma\sqrt{2\pi}}\right)^4 \frac{1}{\sqrt{4}} + \left(\frac{\omega_1^2 \cdot t_p^2}{K}\right)^3 \cdot \left(\frac{1}{\sigma\sqrt{2\pi}}\right)^6 \frac{1}{\sqrt{6}} - \left(\frac{\omega_1^2 \cdot t_p^2}{K}\right)^4 \cdot \left(\frac{1}{\sigma\sqrt{2\pi}}\right)^8 \frac{1}{\sqrt{8}} - +...\right) \tag{D.67}$$

with $\frac{1}{\sqrt{2}} \left(\frac{\omega_1^2 \cdot t_p^2}{K}\right) \left(\frac{1}{\sigma\sqrt{2\pi}}\right)^2 = \Theta$ the relaxation rate is given by

$$\bar{R}_{ex} = \frac{f_B k_{BA} \int_{t=0}^{t_p} \frac{\omega_{1(t)}^2}{\omega_1^2(t) + K} dt}{t_p} = \frac{f_B k_{BA}}{t_p} \sigma\sqrt{2\pi} \left(\Theta \cdot \frac{1}{\sqrt{2}} - \Theta^2 \cdot \frac{1}{\sqrt{4}} + \Theta^3 \cdot \frac{1}{\sqrt{6}} - \Theta^4 \cdot \frac{1}{\sqrt{8}} + ...\right) \tag{D.68}$$

inserting back in D.60 yields

$$\bar{R}_{ex} = f_B k_{BA} \frac{1}{t_p} \sigma\sqrt{2\pi} \frac{\Theta}{\Theta + 1} \tag{D.69}$$

$$\bar{R}_{ex} = f_B k_{BA} \frac{1}{t_p} \sigma\sqrt{2\pi} \frac{\left(\frac{\omega_1^2 \cdot t_p^2}{K}\right)\left(\frac{1}{\sigma\sqrt{2\pi}}\right)^2 \cdot \frac{1}{\sqrt{2}}}{\left(\frac{\omega_1^2 \cdot t_p^2}{K}\right)\left(\frac{1}{\sigma\sqrt{2\pi}}\right)^2 \cdot \frac{1}{\sqrt{2}} + 1} \tag{D.70}$$

$$\bar{R}_{ex} = f_B k_{BA} \frac{1}{t_p} \sigma\sqrt{2\pi} \cdot \frac{\omega_1^2 \cdot \frac{1}{\sqrt{2}}}{\omega_1^2 + K\left(\frac{1}{t_p}\sigma\sqrt{2\pi}\right)^2 \cdot \sqrt{2}} \tag{D.71}$$

with $c_1 = \frac{\sigma\sqrt{2\pi}}{t_p}$ and $c_2 = \frac{\sigma\sqrt{2\pi}}{t_p} \cdot \sqrt{\sqrt{2}}$

$$\bar{R}_{ex} = f_B k_{BA} c_1 \cdot \frac{\omega_1^2}{\omega_1^2 + K \cdot c_2^2} \tag{D.72}$$

$$\bar{R}_{ex} = f_B k_{BA} c_1 \cdot \frac{\omega_1^2}{\omega_1^2 + \left(k_{BA}\left(k_{BA} + R_{2B}\right) + \frac{k_{BA}}{k_{BA}+R_{2B}}\Delta\omega_B^2\right) \cdot c_2^2} \tag{D.73}$$

This is the final result for the exchange-dependent relaxation rate R_{ex} in the large-shift limit.

E. Additional correction terms for AREX

The analytically derived solution for AREX given in equation (6.8) neglects several effects.

Contribution of a semi-solid MT

As given by Zaiss et al. [136] the CEST signal is diluted by a semi-solid MT. This dilution behaves similar to the spillover dilution of the water signal (section 3.4). This can be corrected by incorporating the contribution, i.e. the relative concentration, of the ssMT pool into the analytical formula for AREX.

$$AREX = R_{ex} \cdot DC \cdot \left(1 + f_C \frac{R_{1C}}{R_{1A}}\right) \tag{E.74}$$

$$k_{BA} = \left(-\frac{R_{2B}}{2} + \sqrt{\frac{R_{2B}^2}{4} + \frac{m}{n \cdot c_2^2}}\right) \tag{E.75}$$

$$f_B = \frac{1}{DC \cdot \left(1 + f_C \frac{R_{1C}}{R_{1A}}\right) \cdot n \cdot c_1 \cdot \left(-\frac{R_{2B}}{2} \sqrt{\frac{R_{2B}^2}{4} + \frac{m}{n \cdot c_2^2}}\right)} \tag{E.76}$$

F. Complete statistical evaluation

	volunteer		k_{BA} [s^{-1}]	f_B[‰]	pH	c_{Cr} [mM]
resting condition	#1	whole calf	553 ± 185	2.36 ± 0.42	6.95 ± 0.15	65.5 ± 11.9
		ROI #1			6.90 ± 0.14	69.6 ± 16.8
		ROI #2			7.02 ± 0.14	69.8 ± 16.6
		ROI #3			6.94 ± 0.24	79.5 ± 24.9
	#2	whole calf	394 ± 159	2.06 ± 0.48	6.83 ± 0.22	57.3 ± 13.2
		ROI #1			6.78 ± 0.19	64.6 ± 19.0
		ROI #2			6.89 ± 0.23	68.8 ± 27.2
		ROI #3			6.77 ± 0.26	63.0 ± 23.0
	#3	whole calf	584 ± 207	2.88 ± 0.75	6.98 ± 0.17	80.0 ± 20.9
		ROI #1			6.98 ± 0.19	81.6 ± 22.3
		ROI #2			7.05 ± 0.18	82.1 ± 26.6
		ROI #3			6.92 ± 0.27	99.1 ± 29.7
	#4	whole calf	562 ± 232	2.64 ± 0.60	6.98 ± 0.20	73.2 ± 16.7
		ROI #1			6.90 ± 0.19	85.2 ± 22.8
		ROI #2			7.06 ± 0.22	87.9 ± 29.4
		ROI #3			7.08 ± 0.26	80.8 ± 30.0
during exercise	#1	whole calf	-	-	-	-
		ROI #1			6.98 ± 0.24	80.1 ± 25.9
		ROI #1.1			6.89 ± 0.22	91.1 ± 22.1
		ROI #1.2			7.06 ± 0.22	68.3 ± 24.8
		ROI #2			7.06 ± 0.19	71.9 ± 19.6
		ROI #3			6.89 ± 0.37	109.8 ± 40.9

Table F.1.: Complete statistical evaluation of all different in vivo measurements. The ROIs are according to figures 6.19 and 6.21. Mean values and corresponding uncertainties were determined using the position of the maximum and FWHM of the Gaussin fit, respectively.

G. Histograms of the parameter maps obtained from quantitative CEST in vivo

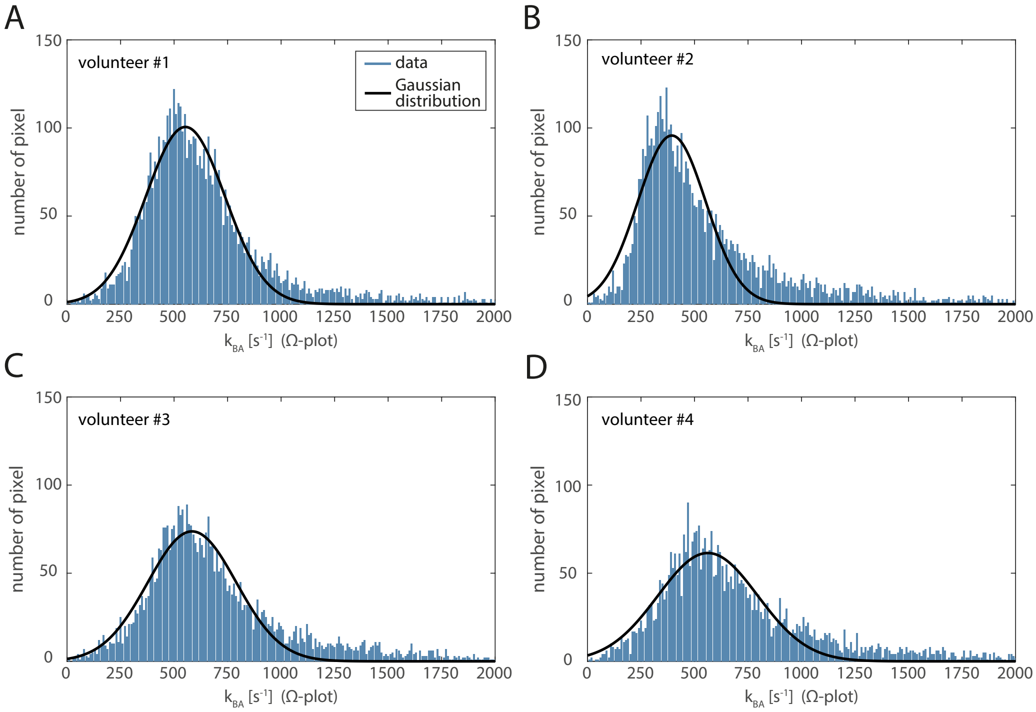

Figure G.1.: The pixel-wise distribution of the exchange rate k_{BA} is shown (blue bars). The data spread accordingly to a Gaussian-function (black line) around a mean k_{BA}.

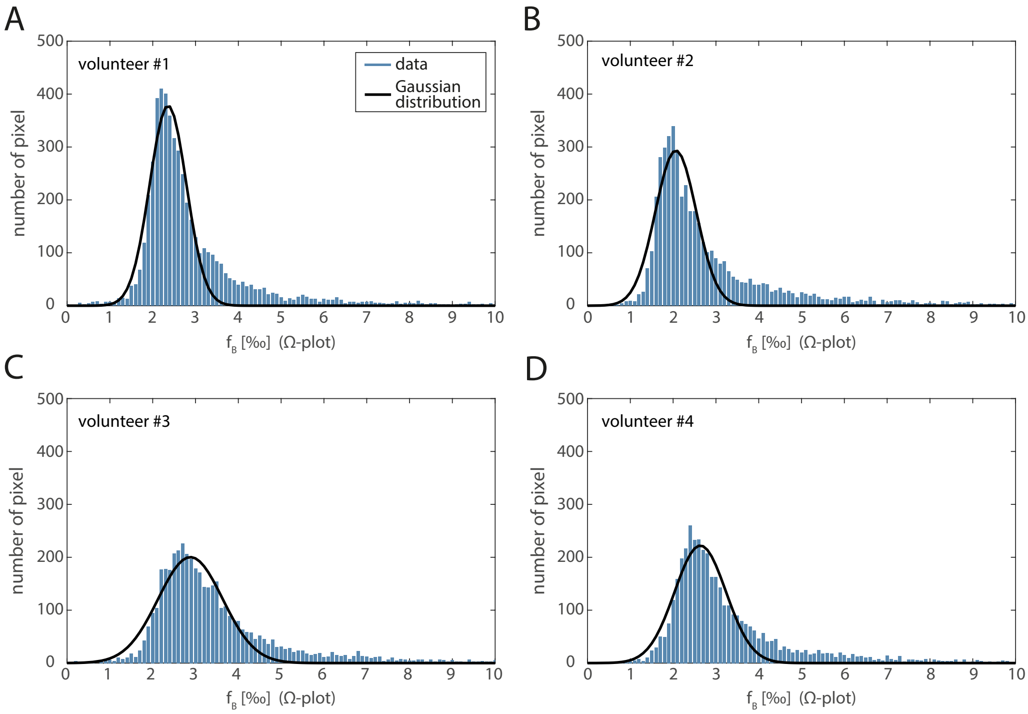

Figure G.2.: The pixel-wise distribution of the exchange rate f_B is shown (blue bars). The data spread accordingly to a Gaussian-function (black line) around a mean f_B.

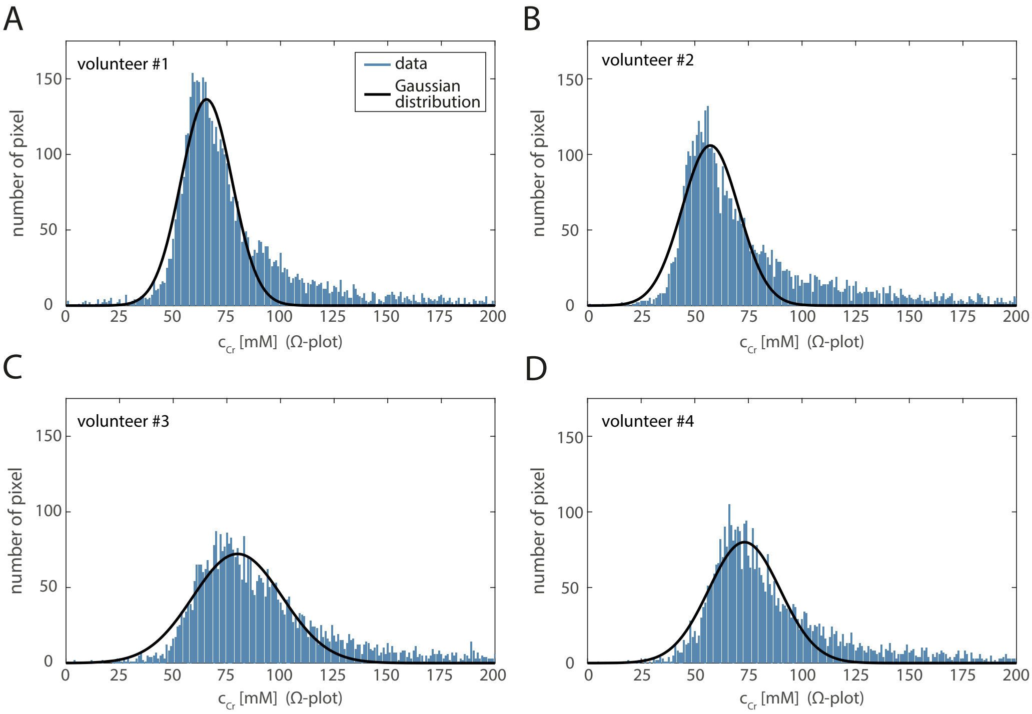

Figure G.3.: The pixel-wise distribution of the exchange rate c_{Cr} is shown (blue bars). The data spread accordingly to a Gaussian-function (black line) around a mean c_{Cr}.

List of Figures

List of Tables

Bibliography

[1] W. Gerlach and O. Stern, “Der experimentelle Nachweis der Richtungsquantelung im Magnetfeld,” *Zeitschrift für Physik*, vol. 9, no. 1, pp. 349–352, 1922.

[2] R. Frisch and O. Stern, “Über die magnetische Ablenkung von Wasserstoffmolekülen und das magnetische Moment des Protons,” *Zeitschrift für Physik*, vol. 86, no. 1-2, pp. 132–134, 1933.

[3] I. I. Rabi, J. R. Zacharias, S. Millman, and P. Kusch, “A New Method of Measuring Nuclear Magnetic Moment,” 1938.

[4] F. Bloch, W. W. Hansen, and M. Packard, “The nuclear induction experiment,” *Physical Review*, vol. 70, no. 7-8, pp. 474–485, 1946.

[5] E. Purcell, H. Torrey, and R. Pound, “Resonance Absorption by Nuclear Magnetic Moments in a Solid,” *Physical Review*, vol. 69, no. 1-2, pp. 37–38, 1946.

[6] W. G. Proctor and F. C. Yu, “The dependence of a nuclear magnetic resonance frequency upon chemical compound,” *Physical Review*, vol. 77, no. 5, p. 717, 1950.

[7] P. C. Lauterbur, “Image formation by induced local interactions: examples employing magnetic resonance,” *Nature*, vol. 242, pp. 190–191, jul 1973.

[8] P. Mansfield and P. K. Grannell, “NMR ’diffraction’ in solids?,” *Journal of Physics C: Solid State Physics*, vol. 6, no. 22, pp. L422–L426, 1973.

[9] S. D. Wolff and R. S. Balaban, “Magnetization transfer contrast (MTC) and tissue water proton relaxation in vivo,” *Magnetic Resonance in Medicine*, vol. 10, no. 1, pp. 135–144, 1989.

[10] S. D. Wolff and R. S. Balaban, “NMR imaging of labile proton exchange,” *Journal of Magnetic Resonance (1969)*, vol. 86, pp. 164–169, jan 1990.

[11] K. M. Ward, A. H. Aletras, and R. S. Balaban, “A new class of contrast agents for MRI based on proton chemical exchange dependent saturation transfer (CEST),” *Journal of magnetic resonance (San Diego, Calif. : 1997)*, vol. 143, pp. 79–87, mar 2000.

[12] J. Zhou, J.-F. Payen, D. A. Wilson, R. J. Traystman, and P. C. M. van Zijl, “Using the amide proton signals of intracellular proteins and peptides to detect pH effects in MRI.,” *Nature medicine*, vol. 9, pp. 1085–90, aug 2003.

[13] M. Haris, R. P. R. Nanga, A. Singh, K. Cai, F. Kogan, H. Hariharan, and R. Reddy, “Exchange rates of creatine kinase metabolites: Feasibility of imaging creatine by chemical exchange saturation transfer MRI,” *NMR in Biomedicine*, vol. 25, pp. 1305–1309, nov 2012.

[14] F. Kogan, M. Haris, A. Singh, K. Cai, C. Debrosse, R. P. R. Nanga, H. Hariharan, and R. Reddy, “Method for high-resolution imaging of creatine in vivo using chemical exchange saturation transfer,” *Magnetic Resonance in Medicine*, vol. 71, pp. 164–172, jan 2014.

[15] E. Rerich, M. Zaiss, A. Korzowski, M. E. Ladd, and P. Bachert, “Relaxation-compensated CEST-MRI at 7T for mapping of creatine content and pH - preliminary application in human muscle tissue in vivo,” *NMR in Biomedicine*, vol. 28, no. 11, pp. 1402–1412, 2015.

[16] S. Walker-Samuel, R. Ramasawmy, F. Torrealdea, M. Rega, V. Rajkumar, S. P. Johnson, S. Richardson, M. Gonçalves, H. G. Parkes, E. Arstad, D. L. Thomas, R. B. Pedley, M. F. Lythgoe, and X. Golay, “In vivo imaging of glucose uptake and metabolism in tumors.,” *Nature medicine*, vol. 19, no. 8, pp. 1067–72, 2013.

[17] X. Xu, N. N. Yadav, L. Knutsson, J. Hua, R. Kalyani, E. Hall, J. Laterra, J. O. Blakeley, R. Strowd, M. Pomper, P. B. Barker, K. Chan, G. Liu, M. T. McMahon, R. D. Stevens, and P. C. M. van Zijl, “Dynamic Glucose-Enhanced (DGE) MRI: Translation to Human Scanning and First Results in Glioma Patients.,” *Tomography : a journal for imaging research*, vol. 1, no. 2, pp. 105–114, 2015.

[18] K. Cai, M. Haris, A. Singh, F. Kogan, J. Greenberg, H. Hariharan, J. A. Detre, and R. Reddy, “Magnetic Resonance Imaging of Glutamate,” *Nature Medicine*, vol. 18, no. 2, pp. 302–306, 2012.

[19] D. R. Roalf, R. P. R. Nanga, P. E. Rupert, H. Hariharan, M. Quarmley, M. E. Calkins, E. Dress, K. Prabhakaran, M. A. Elliott, P. J. Moberg, R. C. Gur, R. E. Gur, R. Reddy, and B. I. Turetsky, “Glutamate imaging (GluCEST) reveals lower brain GluCEST contrast in patients on the psychosis spectrum,” *Molecular Psychiatry*, no. October 2016, pp. 1–8, 2017.

[20] W. Ling, R. R. Regatte, G. Navon, and A. Jerschow, “Assessment of glycosaminoglycan concentration in vivo by chemical exchange-dependent saturation transfer (gagCEST).,” *Proceedings of the National Academy of Sciences of the United States of America*, vol. 105, pp. 2266–70, mar 2008.

[21] C. DeBrosse, R. P. R. Nanga, P. Bagga, K. Nath, M. Haris, F. M. Marincola, M. D. Schnall, H. Hariharan, and R. Reddy, “Lactate Chemical Exchange Saturation Transfer (LATEST) Imaging in vivo A Biomarker for LDH Activity,” *Scientific Reports*, vol. 6, no. October 2015, p. 19517, 2016.

[22] S. Zhang, M. E. Merritt, D. E. Woessner, R. E. Lenkinski, and A. D. Sherry, “PARACEST Agents: Modulating MRI Contrast via Water Proton Exchange,” *Accounts of Chemical Research*, vol. 36, pp. 783–790, oct 2003.

[23] G. Liu, Y. Liang, A. Bar-Shir, K. W. Y. Chan, C. S. Galpoththawela, S. M. Bernard, T. Tse, N. N. Yadav, P. Walczak, M. T. McMahon, J. W. M. Bulte, P. C. M. van Zijl, and A. A. Gilad, “Monitoring enzyme activity using a diamagnetic chemical exchange saturation transfer magnetic resonance imaging contrast agent,” *Journal of the American Chemical Society*, vol. 133, pp. 16326–16329, oct 2011.

[24] K. M. Ward and R. S. Balaban, “Determination of pH using water protons and Chemical Exchange Dependent Saturation Transfer (CEST),” *Magnetic Resonance in Medicine*, vol. 44, pp. 799–802, nov 2000.

[25] P. Z. Sun, C. T. Farrar, and A. G. Sorensen, “Correction for artifacts induced by B0 and B1 field inhomogeneities in pH-sensitive chemical exchange saturation transfer (CEST) imaging,” *Magnetic Resonance in Medicine*, vol. 58, pp. 1207–1215, dec 2007.

[26] T. Jin, P. Wang, X. Zong, and S. G. Kim, “Magnetic resonance imaging of the Amine-Proton EXchange (APEX) dependent contrast.,” *NeuroImage*, vol. 59, pp. 1218–27, jan 2012.

[27] M. Zaiss, J. Xu, S. Goerke, I. S. Khan, R. J. Singer, J. C. Gore, D. F. Gochberg, and P. Bachert, “Inverse Z-spectrum analysis for spillover-, MT-, and T1-corrected steady-state pulsed CEST-MRI - application to pH-weighted MRI of acute stroke,” *NMR in Biomedicine*, vol. 27, pp. 240–252, mar 2014.

[28] M. Zaiss, *Chemical exchange saturation transfer MRI in a clinical context.* Phd thesis, Ruprech-Karls University Heidelberg, 2014.

[29] J. Zhou, D. A. Wilson, P. Z. Sun, J. A. Klaus, and P. C. M. Van Zijl, “Quantitative Description of Proton Exchange Processes between Water and Endogenous and Exogenous Agents for WEX, CEST, and APT Experiments,” *Magnetic Resonance in Medicine*, vol. 51, pp. 945–952, may 2004.

[30] M. T. McMahon, A. A. Gilad, J. Zhou, P. Z. Sun, J. W. M. Bulte, and P. C. M. Van Zijl, “Quantifying exchange rates in chemical exchange saturation transfer agents using the saturation time and saturation power dependencies of the magnetization transfer effect on the magnetic resonance imaging signal (QUEST and QUESP): pH calibration for poly,” *Magnetic Resonance in Medicine*, vol. 55, pp. 836–847, apr 2006.

[31] M. Zaiß, B. Schmitt, and P. Bachert, “Quantitative separation of CEST effect from magnetization transfer and spillover effects by Lorentzian-line-fit analysis of z-spectra,” *Journal of Magnetic Resonance*, vol. 211, pp. 149–155, aug 2011.

[32] P. Z. Sun, “Simplified quantification of labile proton concentration-weighted chemical exchange rate (k ws) with RF saturation time dependent ratiometric analysis (QUESTRA): Normalization of relaxation and RF irradiation spillover effects for improved quantitative ch,” *Magnetic Resonance in Medicine*, vol. 67, pp. 936–942, apr 2012.

[33] M. Kunth, C. Witte, and L. Schröder, “Quantitative chemical exchange saturation transfer with hyperpolarized nuclei (qHyper-CEST): Sensing xenon-host exchange dynamics and binding affinities by NMR,” *The Journal of Chemical Physics*, vol. 141, no. 19, p. 194202, 2014.

[34] W. Dixon, J. Ren, A. Lubag, S. J. Ratnakar, E. Vinogradov, I. Hancu, R. Lenkinski, and A. D. Sherry, “A concentration independent method to measure exchange rates in PARACEST agents,” *Magnetic Resonance in Medicine*, vol. 63, no. 3, pp. 625–632, 2010.

[35] R. Wu, G. Xiao, I. Y. Zhou, C. Ran, and P. Z. Sun, “Quantitative chemical exchange saturation transfer (qCEST) MRI - omega plot analysis of RF-spillover-corrected inverse CEST ratio asymmetry for simultaneous determination of labile proton ratio and exchange rate,” *NMR in Biomedicine*, vol. 28, pp. 376–383, jan 2015.

[36] P. Z. Sun, T. Benner, A. Kumar, and A. G. Sorensen, “Investigation of optimizing and translating pH-sensitive pulsed-chemical exchange saturation transfer (CEST) imaging to a 3T clinical scanner,” *Magnetic Resonance in Medicine*, vol. 60, pp. 834–841, oct 2008.

[37] Z. Zu, K. Li, V. A. Janve, M. D. Does, and D. F. Gochberg, "Optimizing pulsed-chemical exchange saturation transfer imaging sequences," *Magnetic Resonance in Medicine*, vol. 66, pp. 1100–1108, oct 2011.

[38] M. Zaiss and P. Bachert, "Exchange-dependent relaxation in the rotating frame for slow and intermediate exchange - modeling off-resonant spin-lock and chemical exchange saturation transfer," *NMR in Biomedicine*, vol. 26, pp. 507–518, may 2013.

[39] A. Abragam, *Principles of nuclear magnetism.* Oxford, Clarendon Press, 1963.

[40] E. M. Haacke, R. W. Brown, M. R. Thompson, and R. Venkatesan, "Haacke - Magnetic Resonance Imaging - Physical Principles and Sequence Design.pdf," 1999.

[41] R. A. de Graaf, *In Vivo NMR Spectroscopy: Principles and Techniques: 2nd Edition.* John Wiley & Sons, 2007.

[42] P. Zeeman, "On the Influence of Magnetism on the Nature of the Light emitted by a Substance," *Nature*, vol. 55, p. 347, 1897.

[43] P. Ehrenfest, "Bemerkung über die angenäherte Gültigkeit der klassischen Mechanik innerhalb der Quantenmechanik," *Zeitschrift für Physik*, vol. 45, no. 7-8, pp. 455–457, 1927.

[44] N. Bohr, "Über die Serienspektra der Elemente," *Zeitschrilt für Physik*, vol. 2, no. 5, 1920.

[45] W. D. Rooney, G. Johnson, X. Li, E. R. Cohen, S. G. Kim, K. Ugurbil, and C. S. Springer, "Magnetic field and tissue dependencies of human brain longitudinal 1H2O relaxation in vivo," *Magnetic Resonance in Medicine*, vol. 57, no. 2, pp. 308–318, 2007.

[46] G. J. Stanisz, E. E. Odrobina, J. Pun, M. Escaravage, S. J. Graham, M. J. Bronskill, and R. M. Henkelman, "T1, T2 relaxation and magnetization transfer in tissue at 3T," *Magnetic Resonance in Medicine*, vol. 54, pp. 507–512, sep 2005.

[47] I. Tkáč, G. Öz, G. Adriany, K. Ugurbil, and R. Gruetter, "In vivo 1H NMR spectroscopy of the human brain at high magnetic fields: Metabolite quantification at 4T vs. 7T," *Magnetic Resonance in Medicine*, vol. 62, no. 4, pp. 868–879, 2009.

[48] European Agency for Safety and Health at Work, "Directive 2013/35/EU - electromagnetic fields," 2015.

[49] D. I. Hoult and D. Phil, "Sensitivity and power deposition in a high-field imaging experiment.," *Journal of magnetic resonance imaging : JMRI*, vol. 12, no. 1, pp. 46–67, 2000.

[50] R. F. Schmidt and F. Lang, *Physiologie des Menschen*, vol. 91. 2007.

[51] P. M. Tiidus, A. R. Tupling, and M. E. Houston, *Biochemistry primer for exercise science*, vol. 2. Human Kinetics, 4th ed., 2012.

[52] M. Schünke, E. Schulte, and U. Schumacher, *PROMETHEUS - Allgemeine Anatomie und Bewegungssystem.* Thieme (Verlag), 4th ed., 2014.

[53] K. Rink, *Signal-verstärkte multispektrale In-vivo-31P-Magnetresonanztomographie.* Phd thesis, Ruprech-Karls University Heidelberg, 2016.

[54] E. Liepinsh and G. Otting, "Proton exchange rates from amino acid side chains - Implications for image contrast," *Magnetic Resonance in Medicine*, vol. 35, pp. 30–42, jan 1996.

[55] I. Solomon, “Relaxation Processes in a System of Two Spins,” *Physical Review*, vol. 99, no. 2, pp. 559–565, 1955.

[56] J. Grad and R. G. Bryant, “Nuclear magnetic cross-relaxation spectroscopy,” *Journal of Magnetic Resonance*, vol. 90, no. 1, pp. 1–8, 1990.

[57] R. V. Mulkern, “The general solution to the Bloch equation with constant rf and relaxation terms: Application to saturation and slice selection,” *Medical Physics*, vol. 20, no. 1, p. 5, 1993.

[58] S. Goerke, M. Zaiss, P. Kunz, K. D. Klika, J. Windschuh, A. Mogk, B. Bukau, M. E. Ladd, and P. Bachert, “Signature of protein unfolding in chemical exchange saturation transfer imaging,” *NMR in Biomedicine*, vol. 28, no. 7, pp. 906–913, 2015.

[59] D. Liu, J. Zhou, R. Xue, Z. Zuo, J. An, and D. J. J. Wang, “Quantitative characterization of nuclear overhauser enhancement and amide proton transfer effects in the human brain at 7 Tesla,” *Magnetic Resonance in Medicine*, vol. 70, pp. 1070–1081, dec 2013.

[60] S. Goerke, M. Zaiss, and P. Bachert, “Characterization of creatine guanidinium proton exchange by water-exchange (WEX) spectroscopy for absolute-pH CEST imaging in vitro,” *NMR in Biomedicine*, vol. 27, pp. 507–518, feb 2014.

[61] O. Ivchenko, *Studies of molecular dynamics of small metabolites for quantification of chemical exchange saturation transfer in vivo NMR.* Phd thesis, Ruprech-Karls University Heidelberg, 2014.

[62] P. Schuenke, *Quantitative Multi-Pool-Analyse von Glukose-CEST in vitro.* Master thesis, Ruprech-Karls University Heidelberg, 2013.

[63] S. Aime, L. Calabi, L. Biondi, M. De Miranda, S. Ghelli, L. Paleari, C. Rebaudengo, and E. Terreno, “Iopamidol: Exploring the potential use of a well-established x-ray contrast agent for MRI,” *Magnetic Resonance in Medicine*, vol. 53, no. 4, pp. 830–834, 2005.

[64] L. Schröder, T. J. Lowery, C. Hilty, D. E. Wemmer, and A. Pines, “Molecular imaging using a targeted magnetic resonance hyperpolarized biosensor,” *Science*, vol. 774, no. 1993, pp. 0–3, 2005.

[65] B. Yoo and M. D. Pagel, “A PARACEST MRI contrast agent to detect enzyme activity,” *Journal of the American Chemical Society*, vol. 128, no. 43, pp. 14032–14033, 2006.

[66] R. M. Henkelman, G. J. Stanisz, and S. J. Graham, “Magnetization transfer in MRI: A review,” *NMR in Biomedicine*, vol. 14, no. 2, pp. 57–64, 2001.

[67] P. C. M. Van Zijl and N. N. Yadav, “Chemical exchange saturation transfer (CEST): What is in a name and what isn’t?,” *Magnetic Resonance in Medicine*, vol. 65, pp. 927–948, apr 2011.

[68] J. I. Friedman, D. Xia, R. R. Regatte, and A. Jerschow, “Transfer Rate Edited Experiment for the Selective Detection of Chemical Exchange via Saturaion Transfer (TRE-CEST),” *Journal of Magnetic Resonance*, vol. 256, pp. 43–51, 2015.

[69] X. Y. Zhang, F. Wang, A. Afzal, J. Xu, J. C. Gore, D. F. Gochberg, and Z. Zu, “A new NOE-mediated MT signal at around -1.6 ppm for detecting ischemic stroke in rat brain,” *Magnetic Resonance Imaging*, vol. 34, no. 8, pp. 1100–1106, 2016.

[70] J. Windschuh, *Isolation of Unbiased Chemical Exchange Saturation Transfer Effects at 7 T and Application to Brain Tumors.* Phd thesis, Ruprech-Karls University Heidelberg, 2016.

[71] T. Jin and S. G. Kim, "In vivo saturation transfer imaging of nuclear Overhauser effect from aromatic and aliphatic protons: implication to APT quantification," *Proc. Intl. Soc. Mag. Reson. Med.*, vol. 21, p. 2528, 2013.

[72] M. Zaiss, J. Windschuh, S. Goerke, D. Paech, J. E. Meissner, S. Burth, P. Kickingereder, W. Wick, M. Bendszus, H. P. Schlemmer, M. E. Ladd, P. Bachert, and A. Radbruch, "Downfield-NOE-suppressed amide-CEST-MRI at 7 Tesla provides a unique contrast in human glioblastoma," 2016.

[73] J. T. Vaughan, M. Garwood, C. M. Collins, W. Liu, L. Delabarre, G. Adriany, P. Andersen, H. Merkle, R. Goebel, M. B. Smith, and K. Ugurbil, "7T vs. 4T: RF power, homogeneity, and signal-to-noise comparison in head images," *Magnetic Resonance in Medicine*, vol. 46, no. 1, pp. 24–30, 2001.

[74] B. Schmitt, M. Zaiss, J. Zhou, and P. Bachert, "Optimization of pulse train presaturation for CEST imaging in clinical scanners," *Magnetic Resonance in Medicine*, vol. 65, pp. 1620–1629, jun 2011.

[75] Z. Zu, V. A. Janve, J. Xu, M. D. Does, J. C. Gore, and D. F. Gochberg, "A new method for detecting exchanging amide protons using chemical exchange rotation transfer," *Magnetic Resonance in Medicine*, vol. 69, pp. 637–647, mar 2013.

[76] J. Xu, N. N. Yadav, A. Bar-Shir, C. K. Jones, K. W. Y. Chan, J. Zhang, P. Walczak, M. T. McMahon, and P. C. M. Van Zijl, "Variable delay multi-pulse train for fast chemical exchange saturation transfer and relayed-nuclear overhauser enhancement MRI," *Magnetic Resonance in Medicine*, vol. 71, pp. 1798–1812, jun 2014.

[77] M. Zaiss and P. Bachert, "Chemical exchange saturation transfer (CEST) and MR Z-spectroscopy in vivo: a review of theoretical approaches and methods," *Phys. Med. Biol*, vol. 58, pp. 221–269, 2013.

[78] G. Liu, X. Song, K. W. Y. Chan, and M. T. Mcmahon, "Nuts and Bolts of CEST MR imaging," *NMR Biomed*, vol. 26, no. 7, p. 810828, 2013.

[79] M. T. McMahon, A. A. Gilad, J. W. M. Bulte, and P. C. M. van Zijl, eds., *Chemical Exchange Saturation Transfer Imaging.* Pan Stanford Publishing Pte. Ltd., 2016.

[80] P. W. Atkins and J. De Paula, *Atkins' Physical Chemistry.* Oxford University Press, 8th ed., 2006.

[81] Y. Bai, J. S. Milne, L. Mayne, and S. W. Englander, "Primary structure effects on peptide group hydrogen exchange," *Proteins: Structure, Function, and Bioinformatics*, vol. 17, no. 1, pp. 75–86, 1993.

[82] Nomenclature Joint commission on Biochemical Nomenclature, "Nomenclature and symbolism for Amino acids and peptides," *Pure & Applied Chemistry*, vol. 56, no. 5, pp. 595–624, 1984.

[83] K. Wüthrich, *NMR of proteins and nucleic acids.* John Wiley & Sons, 1st ed., 1986.

[84] K. L. Desmond and G. J. Stanisz, "Proceedings for OctoberCEST, the third international workshop on CEST imaging - pH mapping based on the ratiometric amide and amine relationship from endogenous CEST," *Contrast Media & Molecular Imaging*, vol. 8, no. 3, pp. 293–331, 2013.

[85] N. McVicar, A. X. Li, D. F. Gonçalves, M. Bellyou, S. O. Meakin, M. A. Prado, and R. Bartha, "Quantitative tissue pH measurement during cerebral ischemia using amine and amide concentration-independent detection (AACID) with MRI.," *Journal of cerebral blood flow and metabolism : official journal of the International Society of Cerebral Blood Flow and Metabolism*, vol. 34, no. 4, pp. 690–8, 2014.

[86] H. M. McConnell, "Reaction Rates by Nuclear Magnetic Resonance," *The Journal of Chemical Physics*, vol. 28, no. 3, p. 430, 1958.

[87] O. Trott and A. G. Palmer, "R1ρ Relaxation outside of the Fast-Exchange Limit," *Journal of Magnetic Resonance*, vol. 154, pp. 157–160, jan 2002.

[88] P. Z. Sun, P. C. M. Van Zijl, and J. Zhou, "Optimization of the irradiation power in chemical exchange dependent saturation transfer experiments," *Journal of Magnetic Resonance*, vol. 175, no. 2, pp. 193–200, 2005.

[89] J.-E. Meissner, J. Windschuh, M. Zaiss, D. Paech, A. Radbruch, and P. Bachert, "Multi-pool CEST imaging of Glioblastoma at 7T," *Proc. Intl. Soc. Mag. Reson. Med.*, vol. 22, p. 3152, 2014.

[90] K. L. Desmond, F. Moosvi, and G. J. Stanisz, "Mapping of amide, amine, and aliphatic peaks in the CEST spectra of murine xenografts at 7 T," *Magnetic Resonance in Medicine*, vol. 71, pp. 1841–53, jun 2013.

[91] R. M. Henkelman, X. Huang, Q. S. Xiang, G. J. Stanisz, S. D. Swanson, and M. J. Bronskill, "Quantitative interpretation of magnetization transfer.," *Magnetic resonance in medicine : official journal of the Society of Magnetic Resonance in Medicine / Society of Magnetic Resonance in Medicine*, vol. 29, pp. 759–766, jun 1993.

[92] C. Morrison, G. J. Stanisz, and R. M. Henkelman, "Modeling magnetization transfer for biological-like systems using a semi-solid pool with a super-Lorentzian lineshape and dipolar reservoir," *Journal of Magnnetic Resonance, Series B*, vol. 108, no. 2, pp. 103–113, 1995.

[93] A. Pampel, D. K. Müller, A. Anwander, H. Marschner, and H. E. Müller, "Orientation dependence of magnetization transfer parameters in human white matter," *NeuroImage*, vol. 114, pp. 136–146, 2015.

[94] P. Z. Sun, G. Xiao, I. Y. Zhou, Y. Guo, and R. Wu, "A method for accurate pH mapping with chemical exchange saturation transfer (CEST) MRI," *Contrast Media and Molecular Imaging*, vol. 11, no. 3, pp. 195–202, 2016.

[95] T. Jin, J. Autio, T. Obata, and S. G. Kim, "Spin-locking versus chemical exchange saturation transfer MRI for investigating chemical exchange process between water and labile metabolite protons," *Magnetic Resonance in Medicine*, vol. 65, pp. 1448–1460, may 2011.

[96] M. Lourakis, "levmar: Levenberg-Marquardt nonlinear least squares algorithms in {C}/{C}++," 2004.

[97] M. Zaiss, *Ein neues Modell zur Auswertung von NMR-Sättigungstransferexperimenten unter chemischem Austausch.* Diploma thesis, Ruprech-Karls University Heidelberg, 2010.

[98] German Cancer Research Center, "http://www.dkfz.de/en/medphysrad /workinggroups /ultrahighfieldmr /ultrahighfieldmr.html," 2017.

[99] S. Goerke, *Einfluss von Entfaltung und Aggregation auf den 1H-Magnetisierungstransfer zwischen Proteinen und freiem Wasser.* Phd thesis, Ruprech-Karls University Heidelberg, 2015.

[100] A. Tannús and M. Garwood, "Adiabatic pulses," *NMR in Biomedicine*, vol. 10, no. 8, pp. 423–434, 1997.

[101] M. Kim, J. S. Gillen, B. A. Landman, J. Zhou, and C. M. Peter, "WAter Saturation Shift Referencing (WASSR) for chemical exchange saturation transfer experiments," *Magnetic Resonance in Medicine*, vol. 61, no. 6, pp. 1441–1450, 2010.

[102] P. Schuenke, J. Windschuh, V. Roeloffs, M. E. Ladd, P. Bachert, and M. Zaiss, "Simultaneous mapping of water shift and B1(WASABI)-Application to field-Inhomogeneity correction of CEST MRI data," *Magnetic Resonance in Medicine*, vol. 77, no. 2, pp. 571–580, 2016.

[103] J. Windschuh, M. Zaiss, J.-E. Meissner, D. Paech, A. Radbruch, M. E. Ladd, and P. Bachert, "Correction of B1-inhomogeneities for relaxation-compensated CEST imaging at 7 T," *NMR in Biomedicine*, vol. 28, no. 5, pp. 529–37, 2015.

[104] J.-E. Meissner, S. Goerke, E. Rerich, K. D. Klika, A. Radbruch, M. E. Ladd, P. Bachert, and M. Zaiss, "Quantitative pulsed CEST-MRI using Ω-plots," *NMR in Biomedicine*, vol. 28, no. 10, pp. 1196–1208, 2015.

[105] G. J. Kemp, M. Meyerspeer, and E. Moser, "Absolute quantification of phosphorus metabolite concentrations in human muscle in vivo by P-31 MRS: a quantitative review," *NMR in Biomedicine*, vol. 20, no. 6, pp. 555–565, 2007.

[106] Z. Zu, J. T. Spear, H. Li, J. Xu, and J. C. Gore, "Measurement of regional cerebral glucose uptake by magnetic resonance spin-lock imaging," *Magnetic Resonance Imaging*, vol. 32, pp. 1078–84, jun 2014.

[107] L. K. Bell, N. L. Ainsworth, S. H. Lee, and J. R. Griffiths, "MRI & MRS assessment of the role of the tumour microenvironment in response to therapy," *NMR in Biomedicine*, vol. 24, pp. 612–635, jul 2011.

[108] P. Z. Sun, Y. Wang, Z. Z. Dai, G. Xiao, and R. Wu, "Quantitative chemical exchange saturation transfer (qCEST) MRI - RF spillover effect-corrected omega plot for simultaneous determination of labile proton fraction ratio and exchange rate," *Contrast Media and Molecular Imaging*, vol. 9, no. 4, pp. 268–275, 2014.

[109] D. L. Longo, W. Dastrù, G. Digilio, J. Keupp, S. Langereis, S. Lanzardo, S. Prestigio, O. Steinbach, E. Terreno, F. Uggeri, and S. Aime, "Iopamidol as a responsive MRI-chemical exchange saturation transfer contrast agent for pH mapping of kidneys: In vivo studies in mice at 7 T.," *Magnetic resonance in medicine : official journal of the Society of Magnetic Resonance in Medicine / Society of Magnetic Resonance in Medicine*, vol. 65, no. 1, pp. 202–211, 2011.

[110] V. Roeloffs, C. Meyer, P. Bachert, and M. Zaiss, "Towards quantification of pulsed spin-lock and CEST at clinical MR scanners: an analytical interleaved saturation-relaxation (ISAR) approach," *NMR in Biomedicine*, vol. 28, pp. 40–53, oct 2014.

[111] G. E. Santyr, E. J. Fairbanks, F. Kelcz, and J. A. Sorenson, "Off-resonance spin locking for MR imaging," *Magnetic Resonance in Medicine*, vol. 32, pp. 43–51, jul 1994.

[112] Y. K. Tee, A. A. Khrapitchev, N. R. Sibson, S. J. Payne, and M. A. Chappell, "Evaluating the use of a continuous approximation for model-based quantification of pulsed chemical exchange saturation transfer (CEST)," *Journal of Magnetic Resonance*, vol. 222, pp. 88–95, sep 2012.

[113] D. E. Woessner, S. Zhang, M. E. Merritt, and A. D. Sherry, "Numerical solution of the Bloch equations provides insights into the optimum design of PARACEST agents for MRI," *Magnetic Resonance in Medicine*, vol. 53, pp. 790–799, apr 2005.

[114] T. Jin and S. G. Kim, "Quantitative chemical exchange sensitive MRI using irradiation with toggling inversion preparation," *Magnetic Resonance in Medicine*, vol. 68, no. 4, pp. 1056–1064, 2012.

[115] R. Hofstadter, "Electron scattering and nuclear structure," *Reviews of Modern Physics*, vol. 28, no. 3, pp. 214–254, 1956.

[116] S. Mangia, T. Liimatainen, M. Garwood, and S. Michaeli, "Rotating frame relaxation during adiabatic pulses vs. conventional spin lock: simulations and experimental results at 4 T," *Magnetic Resonance Imaging*, vol. 27, pp. 1074–1087, oct 2009.

[117] C. Meyer, *Ein neues Model zur Beschreibung der Dynamik der Magnetisierungsvektoren von 2 Protonen-Pools in Chemical-Exchange-Rotationstransfer(CERT)-Experimenten.* Master thesis, Ruprech-Karls University Heidelberg, 2013.

[118] Z. Zu, J. Xu, H. Li, E. Y. Chekmenev, C. C. Quarles, M. D. Does, J. C. Gore, and D. F. Gochberg, "Imaging amide proton transfer and nuclear overhauser enhancement using chemical exchange rotation transfer (CERT)," *Magnetic Resonance in Medicine*, vol. 72, pp. 471–476, aug 2014.

[119] P. Z. Sun, "Simultaneous determination of labile proton concentration and exchange rate utilizing optimal RF power: Radio frequency power (RFP) dependence of chemical exchange saturation transfer (CEST) MRI," *Journal of Magnetic Resonance*, vol. 202, pp. 155–161, mar 2010.

[120] R. Wu, D. L. Longo, S. Aime, and P. Z. Sun, "Quantitative description of radiofrequency (RF) power-based ratiometric chemical exchange saturation transfer (CEST) pH imaging," *NMR in Biomedicine*, vol. 28, no. 5, pp. 555–565, 2015.

[121] S. Mori, M. Johnson, J. M. Berg, and P. C. M. van Zijl, "Water Exchange Filter (WEX Filter) for Nuclear Magnetic Resonance Studies of Macromolecules," *Journal of the American Chemical Society*, vol. 116, no. 24, pp. 11982–11984, 1994.

[122] S. Mori, C. Abeygunawardana, J. M. Berg, and P. C. M. van Zijl, "NMR Study of Rapidly Exchanging Backbone Amide Protons in Staphylococcal Nuclease and the Correlation with Structural and Dynamic Properties," *Journal of the American Chemical Society*, vol. 119, no. 29, pp. 6844–6852, 1997.

[123] ChEBI Database, "https://www.ebi.ac.uk/chebi/init.do," 2017.

[124] X. Wang and Q. Yin, "Determination of Isoelectric Point of Creatine by Ion Balance Method," *J. Chem. Eng. of Chinese Univ.*, vol. 17, no. 5, pp. 569–574, 2003.

[125] B. J. Diamond, *Temperature and Ph Dependence of the Cyclization of Creatine : A Study Via Mass Spectrometry.* Master thesis, Marshall University, 2005.

[126] P. S. Sharma, D. Lakshmi, and B. B. Prasad, “Molecularly imprinted solid-phase extraction combined with molecularly imprinted polymer-sensor: A diagnostic tool applicable to creatine deficiency syndrome,” *Biomedical Chromatography*, vol. 21, no. 9, pp. 976–986, 2007.

[127] C. K. Jones, A. Huang, J. Xu, R. A. E. Edden, M. Schär, J. Hua, N. Oskolkov, D. Zacà, J. Zhou, M. T. McMahon, J. J. Pillai, and P. C. M. van Zijl, “Nuclear Overhauser enhancement (NOE) imaging in the human brain at 7T,” *NeuroImage*, vol. 77, pp. 114–124, aug 2013.

[128] L. I. Sacolick, F. Wiesinger, I. Hancu, and M. W. Vogel, “B1 mapping by Bloch-Siegert shift,” *Magnetic Resonance in Medicine*, vol. 63, no. 5, pp. 1315–1322, 2010.

[129] A. Singh, K. Cai, M. Haris, H. Hariharan, and R. Reddy, “On B1 inhomogeneity correction of in vivo human brain glutamate chemical exchange saturation transfer contrast at 7T,” *Magnetic Resonance in Medicine*, vol. 69, no. 3, pp. 818–824, 2013.

[130] U. Katscher, P. Börnert, C. Leussler, and J. S. Van den Brink, “Transmit SENSE,” *Magnetic Resonance in Medicine*, vol. 49, no. 1, pp. 144–150, 2003.

[131] Y. Zhu, “Parallel Excitation with an Array of Transmit Coils,” *Magnetic Resonance in Medicine*, vol. 51, no. 4, pp. 775–784, 2004.

[132] J. Keupp and C. Baltes, “Parallel RF transmission based MRI technique for highly sensitive detection of amide proton transfer in the human brain,” *Proc. Intl. Soc. Mag. Reson. Med.*, vol. 44, no. 2010, p. 7784, 2011.

[133] O. Togao, A. Hiwatashi, J. Keupp, K. Yamashita, K. Kikuchi, T. Yoshiura, Y. Suzuki, M. J. Kruiskamp, K. Sagiyama, M. Takahashi, and H. Honda, “Scan-rescan reproducibility of parallel transmission based amide proton transfer imaging of brain tumors,” *Journal of Magnetic Resonance Imaging*, vol. 42, no. 5, pp. 1346–1353, 2015.

[134] Z. Zhou, M. Bez, W. Tawackoli, J. Giaconi, D. Sheyn, S. de Mel, M. M. Maya, B. D. Pressman, Z. Gazit, G. Pelled, D. Gazit, and D. Li, “Quantitative chemical exchange saturation transfer MRI of intervertebral disc in a porcine model,” *Magnetic Resonance in Medicine*, vol. 76, no. 6, pp. 1677–1683, 2016.

[135] S. Goerke, K. S. Milde, R. Bukowiecki, P. Kunz, K. D. Klika, T. Wiglenda, A. Mogk, E. E. Wanker, B. Bukau, M. E. Ladd, P. Bachert, and M. Zaiss, “Aggregation-induced changes in the chemical exchange saturation transfer (CEST) signals of proteins,” *NMR in Biomedicine*, no. October, pp. 1–9, 2016.

[136] M. Zaiss, Z. Zu, J. Xu, P. Schuenke, D. F. Gochberg, J. C. Gore, M. E. Ladd, and P. Bachert, “A combined analytical solution for chemical exchange saturation transfer and semi-solid magnetization transfer,” *NMR in Biomedicine*, vol. 28, pp. 217–230, dec 2015.

[137] H.-Y. Heo, Y. Zhang, D. H. Lee, X. Hong, and J. Zhou, “Quantitative assessment of amide proton transfer (APT) and nuclear overhauser enhancement (NOE) imaging with extrapolated semi-solid magnetization transfer reference (EMR) signals: Application to a rat glioma model at 4.7 tesla,” *Magnetic Resonance in Medicine*, vol. 00, no. November 2014, pp. n/a–n/a, 2015.

[138] J. Xu, M. Zaiss, Z. Zu, H. Li, J. Xie, D. F. Gochberg, P. Bachert, and J. C. Gore, “On the origins of chemical exchange saturation transfer (CEST) contrast in tumors at 9.4T,” *NMR in Biomedicine*, vol. 27, pp. 406–416, jan 2014.

[139] J. Xu, K. W. Y. Chan, X. Xu, N. N. Yadav, G. Liu, and P. C. M. van Zijl, “On-resonance variable delay multipulse scheme for imaging of fast-exchanging protons and semisolid macromolecules,” *Magnetic Resonance in Medicine*, vol. 00, pp. n/a–n/a, 2016.

[140] L. Hermansen and J. B. Osnes, “Blood and muscle pH after maximal exercise in man.,” *Journal of Applied Physiology*, vol. 32, no. 3, pp. 304–308, 1972.

[141] M. Meyerspeer, S. Robinson, C. I. Nabuurs, T. W. Scheenen, A. Schoisengeier, E. Unger, G. J. Kemp, and E. Moser, “Comparing localized and nonlocalized dynamic 31P magnetic resonance spectroscopy in exercising muscle at 7T,” *Magnetic Resonance in Medicine*, vol. 68, no. 6, pp. 1713–1723, 2012.

[142] T. Wallimann, M. Wyss, D. Brdiczka, K. Nicolay, and H. M. Eppenberger, “Intracellular compartmentation, structure and function of creatine kinase isoenzymes in tissues with high and fluctuating energy demands: the ’phosphocreatine circuit’ for cellular energy homeostasis.,” *Biochemical Journal*, vol. 281, no. Pt 1, pp. 21–40, 1992.

[143] E. Hultman, K. Söderlund, J. A. Timmons, G. Cederblad, and P. L. Greenhaff, “Muscle creatine loading in men.,” *Journal of applied physiology (Bethesda, Md. : 1985)*, vol. 81, no. 1, pp. 232–7, 1996.

[144] F. Kogan, M. Haris, C. Debrosse, A. Singh, R. P. Nanga, K. Cai, H. Hariharan, and R. Reddy, “In vivo chemical exchange saturation transfer imaging of creatine (CrCEST) in skeletal muscle at 3T,” *Journal of Magnetic Resonance Imaging*, vol. 40, no. 3, pp. 596–602, 2014.

[145] F. Kogan, R. B. Stafford, E. K. Englund, G. E. Gold, H. Hariharan, J. A. Detre, and R. Reddy, “Perfusion has no effect on the in vivo CEST effect from Cr (CrCEST) in skeletal muscle,” *NMR in Biomedicine*, no. October, pp. 1–6, 2016.

[146] K. Cai, A. Singh, H. Poptani, W. Li, S. Yang, Y. Lu, H. Hariharan, X. J. Zhou, and R. Reddy, “CEST signal at 2 ppm (CEST@2ppm) from Z-spectral fitting correlates with creatine distribution in brain tumor,” *NMR in Biomedicine*, vol. 28, pp. 1–8, oct 2014.

[147] K. Cai, R. W. Tain, X. J. Zhou, F. C. Damen, A. M. Scotti, H. Hariharan, H. Poptani, and R. Reddy, “Creatine CEST MRI for Differentiating Gliomas with Different Degrees of Aggressiveness,” *Molecular Imaging and Biology*, pp. 1–8, 2016.

[148] P. Y. Bruice, *Organic Chemistry*. Pearson Education Inc., 4th ed., 2004.

[149] L. P. Kozlowski, “Proteome - pI : proteome isoelectric point database,” *Nucleic Acids Research*, vol. 45, no. D1, pp. D1112–D1116, 2017.

[150] H. Lodish, A. Berk, C. A. Kaiser, M. Krieger, M. P. Scott, and A. Bretscher, *Molecular Cell Biology*. W. H. Freeman and Company, 6th ed., 2007.

[151] T. L. Hwang, S. Mori, A. J. Shaka, and P. C. M. Van Zijl, “Application of phase-modulated CLEAN chemical EXchange spectroscopy (CLEANEX-PM) to detect water - Protein proton exchange and intermolecular NOEs,” *Journal of the American Chemical Society*, vol. 119, no. 26, pp. 6203–6204, 1997.

[152] E. A. Louie, D. F. Gochberg, M. D. Does, and B. M. Damon, “Transverse relaxation and magnetization transfer in skeletal muscle: Effect of pH,” *Magnetic Resonance in Medicine*, vol. 61, no. 3, pp. 560–569, 2009.

[153] R. B. Moon and J. H. Richards, “Determination of Intracellular pH by 31P Magnetic Resonance,” *The Journal of Biological Chemistry*, vol. 248, no. 20, pp. 7276–7278, 1973.

[154] A. Korzowski and P. Bachert, “Mapping of pH in the human calf muscle at 7 T with 31P 3D echo-planar spectroscopic imaging,” *Proc. Intl. Soc. Mag. Reson. Med.*, vol. 24, p. 1103, 2016.

[155] G. Brix, H. Kolem, W. R. Nitz, M. Bock, A. Huppertz, C. J. Zech, and O. Dietrich, *Magnetic Resonance Tomography.* Berlin, Heidelberg: Springer Berlin Heidelberg, 2008.

[156] V. R. Edgerton, J. L. Smith, and D. R. Simpson, “Muscle fibre type populations of human leg muscles.,” *The Histochemical journal*, vol. 7, no. 3, pp. 259–266, 1975.

[157] W. J. Fink, D. L. Costill, and M. L. Pollock, “Submaximal and Maximal Working Capacity of Elite Distance Runners. Part Ii. Muscle Fiber Composition and Enzyme Activities,” *Annals of the New York Academy of Sciences*, vol. 301, no. 1, pp. 323–327, 1977.

[158] R. A. Robergs, F. Ghiasvand, and D. Parker, “Biochemistry of exercise-induced metabolic acidosis.,” *American journal of physiology. Regulatory, integrative and comparative physiology*, vol. 287, no. 3, pp. R502–16, 2004.

[159] S. Zheng, I. M. J. Van Der Bom, Z. Zu, G. Lin, Y. Zhao, and M. J. Gounis, “Chemical exchange saturation transfer effect in blood,” *Magnetic Resonance in Medicine*, vol. 71, no. 3, pp. 1082–1092, 2014.

[160] C. DeBrosse, R. P. R. Nanga, N. Wilson, K. D’Aquilla, M. A. Elliott, H. Hariharan, F. Yan, K. Wade, S. Nguyen, D. Worsley, C. Parris-Skeete, E. McCormick, R. Xiao, Z. Z. Cunningham, L. Fishbein, K. L. Nathanson, D. R. Lynch, V. A. Stallings, M. Yudkoff, M. J. Falk, R. Reddy, and S. E. McCormack, “Muscle oxidative phosphorylation quantitation using creatine chemical exchange saturation transfer (CrCEST) MRI in mitochondrial disorders,” *JCI Insight*, vol. 1, no. 18, pp. 1–15, 2016.

[161] Y. K. Tee, G. W. J. Harston, N. Blockley, T. W. Okell, J. Levman, F. Sheerin, M. Cellerini, P. Jezzard, J. Kennedy, S. J. Payne, and M. A. Chappell, “Comparing different analysis methods for quantifying the MRI amide proton transfer (APT) effect in hyperacute stroke patients,” *NMR in Biomedicine*, vol. 27, pp. 1019–1029, jun 2014.

[162] G. Helmlinger, F. Yuan, M. Dellian, and R. K. Jain, “Interstitial pH and pO2 Gradients in solid tumor in vivo: High-resolution measurements reveal a lack of correlation,” *Nature medicine*, vol. 3, no. 2, pp. 177–182, 1997.

[163] A. Radbruch, K. Lutz, B. Wiestler, P. Bäumer, S. Heiland, W. Wick, and M. Bendszus, “Relevance of T2 signal changes in the assessment of progression of glioblastoma according to the Response Assessment in Neurooncology criteria,” *Neuro-Oncology*, vol. 14, no. 2, pp. 222–229, 2012.

[164] K. Lutz, B. Wiestler, M. Graf, P. Bäumer, R. Floca, H.-P. Schlemmer, S. Heiland, W. Wick, M. Bendszus, and A. Radbruch, “Infiltrative patterns of glioblastoma: Identification of tumor progress using apparent diffusion coefficient histograms,” *Journal of Magnetic Resonance Imaging*, vol. 39, pp. 1096–1103, may 2014.

[165] G. F. Mason, W.-J. Chu, J. T. Vaughan, S. L. Ponder, D. B. Twieg, D. Adams, and H. P. Hetherington, “Evaluation of31P metabolite differences in human cerebral gray and white matter,” *Magnetic Resonance in Medicine*, vol. 39, no. 3, pp. 346–353, 1998.

[166] I. Hancu, W. T. Dixon, M. Woods, E. Vinogradov, a. D. Sherry, and R. E. Lenkinski, “CEST and PARACEST MR contrast agents.,” *Acta radiologica (Stockholm, Sweden : 1987)*, vol. 51, no. 8, pp. 910–23, 2010.

[167] D. D. Castelli, E. Terreno, D. Longo, and S. Aime, “Nanoparticle-based chemical exchange saturation transfer (CEST) agents,” *NMR in Biomedicine*, vol. 26, no. 7, pp. 839–849, 2013.

[168] S. Aime, A. Barge, D. D. Castelli, F. Fedeli, A. Mortillaro, F. U. Nielsen, and E. Terreno, “Paramagnetic lanthanide(III) complexes as pH-sensitive chemical exchange saturation transfer (CEST) contrast agents for MRI applications,” *Magnetic Resonance in Medicine*, vol. 47, no. 4, pp. 639–648, 2002.

[169] W. Jiang, I. Y. Zhou, L. Wen, X. Zhou, and P. Z. Sun, “A theoretical analysis of chemical exchange saturation transfer echo planar imaging (CEST-EPI) steady state solution and the CEST sensitivity efficiency-based optimization approach,” *Contrast Media and Molecular Imaging*, vol. 11, no. 5, pp. 415–423, 2016.

[170] R. J. Harris, T. F. Cloughesy, L. M. Liau, P. L. Nghiemphu, A. Lai, W. B. Pope, and B. M. Ellingson, “Simulation, phantom validation, and clinical evaluation of fast pH-weighted molecular imaging using amine chemical exchange saturation transfer echo planar imaging (CEST-EPI) in glioma at 3 T,” *NMR in Biomedicine*, vol. 29, no. 11, pp. 1563–1576, 2016.

[171] O. Bieri and K. Scheffler, “Fundamentals of balanced steady state free precession MRI,” *Journal of Magnetic Resonance Imaging*, vol. 38, no. 1, pp. 2–11, 2013.

[172] S. Zhang, Z. Liu, R. E. Lenkinski, and E. Vinogradov, “Balanced Steady State Free Precession (bSSFP) from an effective field perspective: application to the detection of exchange (bSSFPX),” *Journal of Magnetic Resonance*, vol. 275, pp. 55–67, 2017.

List of Publications

Journal articles

Zaiss, Moritz; Windschuh, Johannes; Goerke, Steffen; Paech, Daniel; **Meissner, Jan-Eric**; Burth, Sina; Kickingereder, Philipp; Wick, Wolfgang; Bendszus, Martin; Schlemmer, Heinz-Peter; Ladd, Mark E; Bachert, Peter and Radbruch, Alexander:
Downfield-NOE-suppressed amide-CEST-MRI at 7 Tesla provides a unique contrast in human glioblastoma. *Magnetic Resonance in Medicine* 2016. doi: 10.1002/mrm.26100.

Meissner, Jan-Eric; Goerke, Steffen; Rerich, Eugenia; Klika, Karel D; Radbruch, Alexander; Ladd, Mark E; Bachert, Peter and Zaiss, Moritz:
Quantitative pulsed CEST-MRI using Ω-plots. *NMR in Biomedicine* 2015;28(10): 1196-1208. doi: 10.1002/nbm.3362.

Zaiss, Moritz; Windschuh, Johannes; Paech, Daniel; **Meissner, Jan-Eric**; Burth, Sina; Schmitt, Benjamin; Kickingereder, Philip; Wiestler, Benedikt; Wick, Wolfgang; Bendszus, Martin; Schlemmer, Heinz-Peter; Ladd, Mark E; Bachert, Peter and Radbruch, Alexander:
Relaxation-compensated CEST-MRI of the human brain at 7T: unbiased insight into NOE and amide signal changes in human glioblastoma. *Neuroimage* 2015;112: 180-188. doi: 10.1016/j.neuroimage.2015.02.040.

Windschuh, Johannes; Zaiss, Moritz; **Meissner, Jan-Eric**; Paech, Daniel; Radbruch, Alexander; Ladd, Mark E and Bachert, Peter:
Correction of B1-inhomogeneities for relaxation-compensated CEST imaging at 7 T. *NMR in Biomedicine* 2015;28(5) :529-537. doi:10.1002/nbm.3283.

Paech, Daniel; Burth, Sina; Windschuh, Johannes; **Meissner, Jan-Eric**; Zaiss, Moritz; Eidel, Oliver; Kickingereder, Philipp; Nowosielski, Martha; Wiestler, Benedikt; Sahm, Felix; Floca, Ralf Omar; Neumann, Jan-Oliver; Wick, Wolfgang; Heiland, Sabine; Bendszus, Martin; Schlemmer, Heinz-Peter; Ladd, Mark E; Bachert, Peter and Radbruch, Alexander:
Nuclear Overhauser Enhancement imaging of glioblastoma at 7 Tesla: region specific correlation with apparent diffusion coefficient and histology. *PLOS ONE* 2015;10(3): e0121220. doi: 10.1371/journal.pone.0121220.

Paech, Daniel; Zaiss, Moritz; **Meissner, Jan-Eric**; Windschuh, Johannes; Wiestler, Benedikt; Bachert, Peter; Neumann, Jan Oliver; Kickingereder, Philipp; Schlemmer, Heinz-Peter; Wick, Wolfgang; Nagel, Armin; Heiland, Sabine; Ladd, Mark E; Bendszus, Martin and Radbruch, Alexander:
Nuclear Overhauser Enhancement Mediated Chemical Exchange Saturation Transfer Imaging at 7 Tesla in Glioblastoma Patients. *PLOS ONE* 2014;9(8): e104181. doi: 10.1371/journal.pone.0104181.

Conference contributions

Meißner, Jan-Eric; Bauer, Cornelius; Korzowski, Andreas; Zaiss, Moritz; Ladd, Mark E and Bachert, Peter:
Indirect detection of Lactate using CEST in muscle at 7T. In: *Proceedings of the 33rd Annual Scientific Meeting ESMRMB, Vienna, Austria* 2016; Oral Presentation #281

Meißner, Jan-Eric; Korzowski, Andreas; Zaiss, Moritz; Ladd, Mark E and Bachert, Peter:
Quantitative pulsed CEST-MRI using Ω-plots . In: *Proceedings of the 33rd Annual Scientific Meeting ESMRMB, Vienna, Austria* 2016; Oral Presentation #153

Bauer, Cornelius; **Meißner, Jan-Eric**; Korzowski, Andreas; Zaiss, Moritz; Ladd, Mark E and Bachert, Peter:
Indirekter Nachweis von Laktat in vivo mittels Chemical Exchange Saturation Transfer. In: *Proceedings of the 47th Annual Scientific Meeting DGMP, Würzburg, Germany* 2016; Oral Presentation #28

Windschuh, Johannes; **Meissner, Jan-Eric**; Schuenke, Patrick; Zaiss, Moritz; Ladd, Mark E and Bachert, Peter:
Charakterisierung der CEST-Signale von Gelatine. In: *Proceedings of the 47th Annual Scientific Meeting DGMP, Würzburg, Germany* 2016; Oral Presentation #21

Meißner, Jan-Eric; Goerke, Steffen; Rerich, Eugenia; Klika, Karel D; Radbruch, Alexander; Ladd, Mark E; Bachert, Peter and Zaiss, Moritz:
Quantitative pulsed CEST-MRI using Ω-plots . In: *Proceedings of the 19th Annual Scientific Meeting ISMRM-DS, Würzburg, Germany* 2016; Oral Presentation #G5

Paech, Daniel; Zaiss, Moritz; Windschuh, Johannes; Goerke, Steffen; Milde, Katharina; **Meissner, Jan-Eric**; Burth, Sina; Kickingereder, Philipp; Wick, Wolfgang; Ladd, Mark E; Bachert, Peter; Bendszus, Martin; Schlemmer, Heinz-Peter and Radbruch, Alexander:
Quantitative CEST-Bildgebung bei Glioblastompatienten am 7 Tesla Ultrahochfeldtomografen. In: *RöFo-Fortschritte auf dem Gebiet der Röntgenstrahlen und der bildgebenden Verfahren* 2016;

Windschuh, Johannes; Zaiss, Moritz; Goerke, Steffen; Paech, Daniel; **Meissner, Jan-Eric**; Burth, Sina; Kickingereder, Philipp; Wick, Wolfgang; Bendszus, Martin; Schlemmer, Heinz-Peter; Ladd, Mark E; Bachert, Peter and Radbruch, Alexander:
Downfield-rNOE-Suppressed Amide-CEST-MRI at 7 Tesla Provides a Unique Contrast in Human Glioblastoma. In: *Proceedings of the Workshop on Ultra High Field MRI of the ISMRM, Heidelberg, Germany* 2016; Flash Poster #41

Windschuh, Johannes; Zaiss, Moritz; Goerke, Steffen; Paech, Daniel; **Meissner, Jan-Eric** and Bachert, Peter:
Influence of tissue integrity and external magnetic field strength on the exchange-relayed NOE-CEST effect of mobile proteins. In: *Proceedings of the 25th Annual Meeting of the ISMRM, Singapore, Singapore* 2016; Poster #1521

Meissner Jan-Eric; Zaiss, Moritz; Rerich, Eugenia and Bachert, Peter:
Quantitative CEST using Ω-plots in the case of trains of Gaussian-shaped saturation pulses. In *Proceedings of the 5th CEST imaging workshop (PennCEST), Philadelphia, PA, USA* 2015, Poster #12

Meissner Jan-Eric; Korzowski, Andreas; Zaiss, Moritz and Bachert, Peter: Quantitative pulsed CEST at 7T in vivo. In *Proceedings of the 5th CEST imaging workshop (PennCEST), Philadelphia, PA, USA* 2015, Poster #13

Paech, Daniel; Burth, Sina; Windschuh, Johannes; **Meissner, Jan Eric**; Zaiss, Moritz; Eidel, Oliver; Kickingereder, Philipp; Bachert, Peter; Wick, Wolfgang; Schlemmer, Heinz-Peter ; Floca, Ralf Omar; Ladd, Mark E; Heiland, Sabine; Bendszus, Martin and Radbruch, Alexander: Nuclear Overhauser Enhancement Imaging of Glioblastoma Patients at 7 Tesla: Region Specific Correlation with Diffusion Weighted MRI. *Proceedings of the 23rd Annual Scientific Meeting ISMRM, Toronto, Canada* 2015; Poster #3363

Windschuh, Johannes; Goerke, Steffen; **Meissner, Jan-Eric**; Radbruch, Alexander; Bachert, Peter and Zaiss, Moritz: Isolated Amide Proton CEST Contrast at 7 T Correlates with Contrast-enhanced T1-weighted Images of Tumor Patients. *Proceedings of the 23rd Annual Scientific Meeting ISMRM, Toronto, Canada* 2015; Poster #1773

Meissner, Jan-Eric; Rerich, Eugenia; Zaiss, Moritz and Bachert, Peter: Quantitative CEST (qCEST) using Ω-plots in the case of trains of Gaussian-shaped saturation pulses. *Proceedings of the 23rd Annual Scientific Meeting ISMRM, Toronto, Canada* 2015; Poster #1754

Windschuh, Johannes; Goerke, Steffen; **Meissner, Jan-Eric**; Radbruch, Alexander; Bachert, Peter and Zaiss, Moritz: Isolated Amide Proton CEST Contrast at 7T Correlates with Contrast-enhanced T1w-Images of Tumor Patients. In: *Proceedings of the 56th Annual Scientific Meeting ENC, Pacific Grove, CA, USA* 2015; Oral Presentation #ThOA

Meissner, Jan-Eric; Zaiss, Moritz; Goerke, Steffen; Rerich; Eugenia; Radbruch, Alexander and Bachert, Peter: Quantitative CEST (qCEST) using Ω-plots in the case of trains of Gaussian-shaped saturation pulses. *Proceedings of the 56th Annual Scientific Meeting ENC, Pacific Grove, CA, USA* 2015; Poster #186

Windschuh, Johannes; Zaiss, Moritz; **Meissner, Jan-Eric**; Paech, Daniel; Radbruch, Alexander and Bachert, Peter: Paving the way for protein-concentration-weighted MRI. In: *Proceedings of the 9th Winterschool of the Heidelberg Graduate School of Fundamental Physics, Obergurgl, Austria* 2015; Poster

Radbruch, Alexander; Paech, Daniel; Windschuh, Johannes; **Meissner, Jan-Eric**; Schlemmer, Heinz-Peter; Bachert, Peter; Ladd, Mark E and Bendszus, Martin: Three-dimensional Chemical Exchange Saturation Transfer (CEST) Imaging at 7 Tesla in Glioblastoma Patients. In: *RöFo-Fortschritte auf dem Gebiet der Röntgenstrahlen und der bildgebenden Verfahren* 2014;

Windschuh, Johannes; Zaiss, Moritz; **Meissner, Jan-Eric**; Paech, Daniel; Radbruch, Alexander and Bachert, Peter: Paving the way for protein-concentration-weighted MRI. In: *Proceedings of the Workshop on Quantum Dynamics in Physics, Chemistry and Biology of the Max Planck Research School for Quantum Dynamics, Heidelberg, Germany* 2014

Zaiss, Moritz; Windschuh, Johannes; **Meissner, Jan-Eric**; Paech, Daniel; Radbruch, Alexander and Bachert, Peter:
Inverse Z-spectrum analysis for clean NOE and amide CEST-MRI – application to human glioma. In: *Proceedings of the Joint Annual Scientific Meeting ISMRM-ESMRMB, Milan, Italy* 2014; Oral Presentation #0766

Paech, Daniel; **Meissner, Jan Eric**; Windschuh, Johannes; Wiestler, Benedikt; Neumann, Jan Oliver; Schlemmer, Heinz-Peter; Wick, Wolfgang; Nagel, Armin; Ladd, Mark E; Bendszus, Martin; Bachert, Peter; Zaiss, Moritz and Radbruch, Alexander:
Nuclear Overhauser Enhancement (NOE) Mediated Chemical Exchange Saturation Transfer (CEST) Imaging At 7 Tesla In Glioblastoma Patients. In: *Proceedings of the Joint Annual Scientific Meeting ISMRM-ESMRMB, Milan, Italy* 2014; Oral Presentation #0767

Windschuh, Johannes; Zaiss, Moritz; **Meißner, Jan-Eric** and Bachert, Peter:
B_1-correction of isolated-spillover-corrected CEST effects at 7T. In: *Proceedings of the Joint Annual Scientific Meeting ISMRM-ESMRMB, Milan, Italy* 2014; Poster #3303

Meißner, Jan-Eric; Windschuh, Johannes; Zaiss, Moritz; Paech, Daniel; Radbruch, Alexander and Bachert, Peter:
Multi-pool CEST imaging of Glioblastoma. In: *Proceedings of the Joint Annual Scientific Meeting ISMRM-ESMRMB, Milan, Italy* 2014; Poster #3152

Meißner, Jan-Eric; Zaiß, Moritz; Meyer, Christian and Bachert, Peter:
Simulation und experimentelle Bestimmung der optimalen Messparameter für APT-CEST bei 3T. In: *Proceedings of the 44th Annual Scientific Meeting DGMP, Cologne, Germany* 2013; Oral presentation #31

Acknowledgment

I would like to take this opportunity to thank all those who supported me and have made this thesis possible ...

... Prof. Dr. Peter Bachert for the opportunity to graduate in your working group, your trust and support, which allowed me to implement my own ideas, and every physical and non-physical fun fact you gave us,

... Prof. Dr. Rainer Fink for kindly accepting to be the second referee for my dissertation,

... Dr. Moritz Zaiss, who opened me the door to the CEST universe, which started this incredible (scientific) journey,

... all my colleagues, especially Steffen, Andreas, Eugenia, Johnny, Philipp, Patrick, Daniel, Ferdinand, Johannes, Dominik, Loreen and Cornelius, for providing an incredible relaxed and beautiful atmosphere in our group,

... all my friends in Heidelberg, Berlin and everywhere else who accompanied me before, during and hopefully after this thesis. You are the best!

... Julia, for the best support I could have ever imagined.

Mein herzlichster Dank geht an meine Eltern, deren liebevolle Unterstützung mich jederzeit und jederorts erreichte. Ihr habt dies hier alles erst ermöglicht. Danke!